

Place in book drop to remove this checkout from your record. FINES will be charged if book is returned after the date stamped below.

	Stalliped beron	
120		
7 15 <sub>1</sub>		
JUL 17 7 1992		
AUS 1 O D		
5 22T		

# ELECTRON TRANSPORT, MAGNETIC AND GALVANOMAGNETIC PROPERTIES OF Ag-Co LAYERED STRUCTURES

Ву

Jon Michael Slaughter

#### A DISSERTATION

Submitted to

Michigan State University
in partial fulfillment of the requirements
for the degree of

DOCTOR OF PHILOSOPHY

Department of Physics and Astronomy

#### **ABSTRACT**

# ELECTRON TRANSPORT, MAGNETIC AND GALVANOMAGNETIC PROPERTIES OF Ag-Co LAYERED STRUCTURES

Βv

#### Jon Michael Slaughter

We have produced Ag-Co layered films with layer thicknesses down to 10A by sputtering. Since Ag and Co are mutually insoluble, we expect the interfaces between the layers to be sharp. X-ray diffraction measurements indicate that the samples are textured and polycrystalline with coherence over many layers.

We have, for the first time, measured the resistivity perpendicular to the layers ( $\rho_{perp}$ ) of a periodic layered metallic structure (LMS). Producing samples for the perpendicular measurements requires the use of a unique computer controlled substrate positioning and masking apparatus. A SQUID based circuit with a high-precision current comparator was used to make the measurements at low temperature (1.4 - 8.5K). Resistivity measurements made parallel and perpendicular to the layers are compared to free electron models allowing specular and diffuse scattering at the interfaces. We conclude that the unusually low resistivity of the Ag-Co LMS is mainly due to transmission of conduction electrons through the interfaces.

Magnetization measurements were made on a SHE SQUID magnetometer. We find that the saturation magnetization of Co is almost independent of layer thickness. Hall effect measurements, taken together with the magnetization results, show that a magnetic surface anisotropy is present in the samples.

The behavior of the magnetoresistance illustrates the dramatic effect of the demagnetizing field in these samples and shows anisotropic effects which cannot be explained by simply considering the layers as resistors in parallel.

To my mother and father

#### **ACKNOWLEDGMENTS**

I wish to thank Professor Peter A. Schroeder and Professor William P. Pratt, Jr. of Michigan State University and Professor Hideyuki Sato of Tokyo Metropolitan University for their support, ideas and long hours of taking data. Neither their contributions to my understanding of physics nor their friendship will be forgotten.

I am grateful to Professor Jerry Cowen and Professor Carl Foiles for following my progress and contributing to the stimulating and fruitful academic environment I have enjoyed here. I wish to thank Tom Palazzolo and Richard Hoskins for their contributions to the design and construction of the SPAMA. I am also indebted to Daniel Edmunds and Donald Shull for sharing with me their expertise in computer aided design. I am grateful to Professor Stuart Solin and Professor Duncan Sibley for the use of their X-ray equipment.

Most of all I would like to thank my wife, Anna, for her loving support and encouragement during the course of my thesis work.

The support of the National Science Foundation and the Michigan State University Center for Fundamental Materials Research is gratefully acknowledged.

#### TABLE OF CONTENTS

																				Pa	ge
LIST (	OF	TABLES.	•		•	•	•	•	•						•	•	•		•		iх
LIST (	OF	FIGURES.	•			•		•	•	•					•	•	•			•	x
INTRO	DUC	TION	•		•	•		•		•	•				•	•	•	•	•		1
СНАРТ	ER	1																			
Produc	eti	on and Ch	nara	cte	riz	ati	on	of	the	Th	in	Fil	.ms	San	ıp1e	s					
ı	Α.	Introduct	ion	١.	•	•	•	•				•	•		•		•				5
E	В.	Sputterin	ng S	yst	em	0ve	rvi	ew.			•	•	•	•		•	•	•			7
C	c.	Sputterin	ng S	our	ces	•	•	•	•		•	•	•	•	•	•	•				11
I	D.	Substrate	e Po	sit	ion	ing	an	d M	lask	ing	, Ap	par	atı	ıs.	•		•	•			13
E	Ε.	Computer	Int	erf	aci	ng	and	So	ftw	are	· .	•	•								17
F	F.	System Pe	erfo	rma	nce	•					•	•	•		•						20
(	G.	X-ray Dif	fra	cti	on	The	ory	•		•			•		•			•			22
ŀ	Н.	X-ray Dif	fra	cti	on:	E	хре	rim	ent	al	Res	u) t	s a	and	Mod	lel					
		Calculati	ions			•							•		•			•	•		33
:	Ι.	Determini	ing	the	. Sa	mp1	e G	eom	etr	у.			•						•	•	46
CHAPTE	ER	2																			
Resist	tiv	ity Paral	llel	an	d P	erp	end	icu	lar	to	th	e L	.aye	ers							
ı	Α.	Parallel	Res	ist	ivi	ty															
		1. Intr	°odu	cti	on.				•				•								52
		2. Para	alle	1 T	'ran	spo	rt	The	ory	•				•				•			54
		а.	. Mo	ide l	1	- T	ran	smi	ssi	on.											57

b. Model 2 - Reflection 6	0
c. Determining the Bulk Parameters	,2
3. Experiment	,4
B. Perpendicular Resistivity	
1. Free-electron Perpendicular Transport Theory 7	1
2. Band Structure Theory for LMS	'5
3. Superconductor - Normal Metal Interfaces	'6
4. Experiment	
a. Technique for Measuring the Perpendicular	
Resistivity	'9
b. Simple film measurements	12
c. Sandwich Samples	36
d. LMS Samples	36
CHAPTER 3	
Magnetization, Hall Effect and Magnetoresistestance	
A. Magnetization Theory	
1. Crystallographic Anisotropy 9	)4
2. Shape Anisotropy	)5
3. Surface Anisotropy	8
B. Hall Effect Theory	) 1
C. Magnetization Measurements	)4
D. Hall Effect Measurements	)7
E. Magnetoresistance Measurements	7
CHAPTER 4	
Results, Conclusions and Recommendations	
A. Results and Conclusions	24
B. Recommendations	28

APPENDIX A										
Reading Power Supply Parameters.	•		•	•		•	•	•	•	.131
APPENDIX B					•					
Sputtering System Instructions	•	•	•	•	•		•	•	•	.136
LIST OF REFERENCES								•		. 151

# LIST OF TABLES

Table		Page
1.1	Typical production parameters and FMSS	. 21
1.2	Parameters for step model calculations	. 30
1.3	Summary of step model results	. 45
1.4	Comparison of nominal and measured sample parameters	. 50
2.1	Definitions of parameters for model 1 integrals	. 61
2.2	Free-electron parameters for bulk Ag and Co	. 66
2.3	Run 38 sample summary	. 67
2.4	Pure film samples for $\rho_{\mbox{\footnotesize{perp}}}$ measurements	. 85
2.5	LMS samples for $\rho_{perp}$ measurements	. 89

## LIST OF FIGURES

Figure		Page
1.1	Sample design for perpendicular resistance measurement.	. 6
1.2	Sample design for parallel resistance measurement	. 8
1.3	Schematic view of the sputtering system	. 9
1.4	Exploded view of SPAMA, sources and chimneys	. 12
1.5	Neutral position of SPAMA	. 15
1.6	Connections to IBM Personal Computer XT	. 18
1.7	Control software organization	. 19
1.8	X-ray diffractometer geometry	. 24
1.9	Step model of a LMS	. 26
1.10	$\theta$ -2 $\theta$ spectra for $\Lambda$ =21.5 $\mathring{A}$ : Experimental and step model.	. 31
1.11	Momentum transfer q versus index m for sample 3805	. 34
1.12	$\theta$ -2 $\theta$ spectra for $\Lambda$ =157 Å: Experimental and step model.	. 36
1.13	$\theta$ -2 $\theta$ spectra for $\Lambda$ =114 Å: Experimental and step model.	. 37
1.14	$\theta$ -2 $\theta$ spectra for $\Lambda$ = 80 Å: Experimental and step model.	. 38
1.15	$\theta$ -2 $\theta$ spectra for $\Lambda$ = 53 Å: Experimental and step model.	. 39
1.16	$\theta$ -20 spectra for $\Lambda$ =38.5Å: Experimental and step model.	. 40
1.17	$\theta$ -2 $\theta$ spectra for $\Lambda$ = 30 Å: Experimental and step model.	. 41
1.18	$\theta$ -2 $\theta$ spectra for $\Lambda$ = 21 Å: Experimental and step model.	. 42
1.19	$\theta$ -2 $\theta$ spectra for $\Lambda$ = 16 Å: Experimental and step model.	. 43
1.20	$\theta$ -2 $\theta$ spectra for " $\Lambda$ = 5 $\mathring{A}$ ": Experimental and step model.	. 47
1.21	Dektak profile of a Nb strip	. 51

2.1	$\rho_{par}$ at room temperature for various LMS	. 53
2.2	ℓ <sub>eff</sub> versus Λ for Run 38 Ag-Co LMS	. 55
2.3	Fuchs model geometry of a LMS	. 56
2.4	Apparatus used for $\rho_{\mbox{\scriptsize par}}$ and Hall measurements	. 65
2.5	$\rho_{\mbox{\footnotesize{par}}}$ versus 1/A at room temperature	. 68
2.6	$\rho_{\mbox{\scriptsize par}}$ versus 1/A at liquid nitrogen temperature	. 69
2.7	$\rho_{\mbox{\scriptsize par}}$ versus 1/A at liquid helium temperature	. 70
2.8	Schematic view of "1K" refrigerator	. 80
2.9	SQUID circuit for resistance measurement	. 81
2.10	Perpendicular resistivity for pure films of Ag and Co	. 84
2.11	Geometry of sandwich samples	. 87
2.12	Perpendicular resistivity of sandwich samples	. 88
2.13	Perpendicular resistivity of LMS sample 8001	. 90
2.14	$\rho_{\text{o}}$ (perpendicular) versus 1/Λ	. 92
3.1	Orientation of the thin film	. 96
3.2	M versus $H_a$ for a thin film with only shape anisotropy.	. 99
3.3	Expected form of $\rho_H$ versus $B_a$	.103
3.4	M versus B for Ag-Co LMS with $\Lambda$ =15Å and $\Lambda$ =151Å	.105
3.5	$M_{_{\mbox{\scriptsize S}}}$ versus A. Arrow indicates $M_{_{\mbox{\scriptsize S}}}$ of a 5000Å Co film	.106
3.6	$\rho_{H}$ versus $B_{a}$ for a 5000Å Co film	.108
3.7	$ ho_{ m H}$ versus B for a $\Lambda$ =80Å Ag-Co LMS	.109
3.8	$\rho_{H}$ versus $B_{a}$ for $\Lambda$ =16, 80, 160Å Ag-Co LMS at T=295K	.110
3.9	B versus $\Lambda$ at 4.2K	.111

3.10	B versus $1/\Lambda$ at 4.2K	•	•	•	•	•	•	•	•	•	•	.112
3.11	$R_s^M$ versus $\rho^2$ at T=295K.		•		•					•	•	. 1 15
3.12	$R_s^M$ versus $\rho^2$ at T=4.2K.	•	•		•			•	•	•		.116
3.13	Magnetoresistance geometry.	•	•			•	•	•		•	•	. 1 18
3.14	$\rho$ versus B for a 5000Å Co f	`ilm	•	•	•	•	•	•	٠	•	•	.120
3.15	$\theta$ dependence of magnetoresis	tan	ce	for	th	ree	e Ag	g-Co	LN	AS.	•	.121
3.16	Magnetoresistance anisotropy	an	dρ	par	ve	rsı	ıs <i>f</i>	١.	•	•	•	.123

#### INTRODUCTION

There has been much recent work concerning the properties of layered metallic structures (LMS); structures composed of a repeated bilayer of two metals. These structures are interesting because of possible applications and because they can be used to study fundamental properties of the constituents. Some applications currently being explored by various experimental groups are optics for X-rays and magneto-optic data storage. Fundamental properties which can be studied with LMS include finite size effects and band structure changes due to the artificial periodicity.

For the purposes of this thesis the name LMS refers only to thin film structures composed of a repeated bilayer of two metals. The thickness of the bilayer is called the period of the structure and is denoted by  $\Lambda$ . The term multilayer refers to any layered structure and need not be periodic.

LMS with varying degrees of order have been identified. A compositionally modulated alloy (CMA) has alternating layers of two elements having the same structure and lattice constant. The interfaces of a CMA are not sharp due to interdiffusion of the elements. Layered ultrathin coherent structures (LUCS) are made of alternating layers of two materials which may have different lattice constants or even different structures. The atomic planes of LUCS are coherent over many layers in the direction perpendicular to the interfaces and the

interfaces are sharp within a few atomic spacings. Artificial metallic superlattices (AMS) are essentially LUCS with long range coherence inplane as well as perpendicular to the layers. The Ag-Co LMS would be characterized as a LUCS.

There were three main reasons for choosing the Ag-Co system.

- 1. Previous work, at Argonne National Laboratory, has shown that Ag and Co form a coherent LMS (or LUCS).
- 2. Ag and Co are mutually insoluble, implying that sharp interfaces could be formed.
- 3. Co is ferromagnetic even in atomically thin layers [Me80, Vi83, Ch86] a requirement for the technique we used to measure the resistivity perpendicular to the layers. In this perpendicular technique the sample film is in direct contact with a superconductor. If the film is not ferromagnetic, it will become superconducting at low temperatures due to the superconducting proximity effect. Thin layers of a ferromagnetic material can prevent the transmission of Cooper pairs, thus eliminating the proximity effect and allowing measurements of the perpendicular resistivity at low temperatures.

When considering electron transport in a LMS, one might anticipate contributions from factors which arise simply from the fact that the structure is composed of many thin films in contact with each other. Interface scattering, reflection and transmission are examples of such factors. One might also anticipate contributions from effects having their origin in the artificial structure itself rather than in the properties of the individual materials. For example, if the electron mean free path in the LMS is long compared to the artificial period, the artificial periodicity could introduce gaps in the band structure of the

layered material. Such gaps would cause anisotropies in the transport properites [Ko81]. If resistivity measurements could be made both parallel and perpendicular to the layers, it would be possible to study both types of effects. Unfortunately, there was previously no technique available for measuring the perpendicular resistivity  $\rho_{perp}$ . The difficulty in measuring  $\rho_{perp}$  is due to the fact that a LMS is a thin film having a total thickness of ~1 µm with the layers lying in the plane of the film. Therefore, the sample geometry for measuring  $\rho_{perp}$  is that of an extremely short resistor with a comparatively large cross section, resulting in a very small resistance. The first goal of this work was to develop a technique for measuring  $\rho_{perp}$ . Chapter 2 describes resistivity measurements made both parallel and perpendicular to the layers of Ag-Co LMS.

Magnetization measurements have been made on a variety of LMS by other workers. Various surface effects have been reported including both increases and decreases in the magnetic moment of the magnetic material as a result of being layered with nonmagnetic materials. We have made magnetization, Hall effect and magnetoresistance measurements on the Ag-Co LMS. The results are described in Chapter 3. The saturation magnetization  $\mathbf{M}_{\mathbf{S}}$  of the Ag-Co system has been previously studied by Takahashi et al. [Ta84]. They found that  $\mathbf{M}_{\mathbf{S}}$  decreases with A over a wide range of Co thickness whereas we have found it to be nearly constant. An explanation of the discrepancy is discussed in Chapter 3.

Of course, before any measurements can be made, one must first produce and characterize the samples. All of the samples for this

thesis were produced by sputtering and characterized by X-ray diffraction measurements. The subject of Chapter 1 is the production and characterization of the samples.

#### CHAPTER 1

#### PRODUCTION AND CHARACTERIZATION OF THIN FILM SAMPLES

#### A. Introduction

All of the thin films were produced with the M.S.U. sputtering system. It is a cryopumped four-source sputtering system with several unique features including a versatile substrate positioning and masking apparatus (SPAMA) driven by a computer controlled stepping motor. Although the basic system was built by L. M. Simard, Inc., the design and construction of the SPAMA and the computer interfacing and programming were done as a part of this thesis.

An important consideration in the design of this sputtering system was that it should be able to produce samples for the measurement of the electrical resistivity perpendicular to the layers of LMS. The sample design we have used is illustrated in Figure 1.1. These samples are made by first depositing a Nb strip on the substrate, followed by the sample film and finally a top Nb strip. Since the Nb strips are superconducting, a single strip can be used as both a current and voltage lead for a four-probe resistance measurement. The part of the sample film which carries the bulk of the current is that which is bounded above and below by the leads; this region defines the "effective sample." There are fringing currents around the edges of the effective sample which will introduce some error in the calculated resistivity. The lateral extent of the fringing current is of the order of the thickness of the sample film. Thus, for a sample film 1µm thick and an

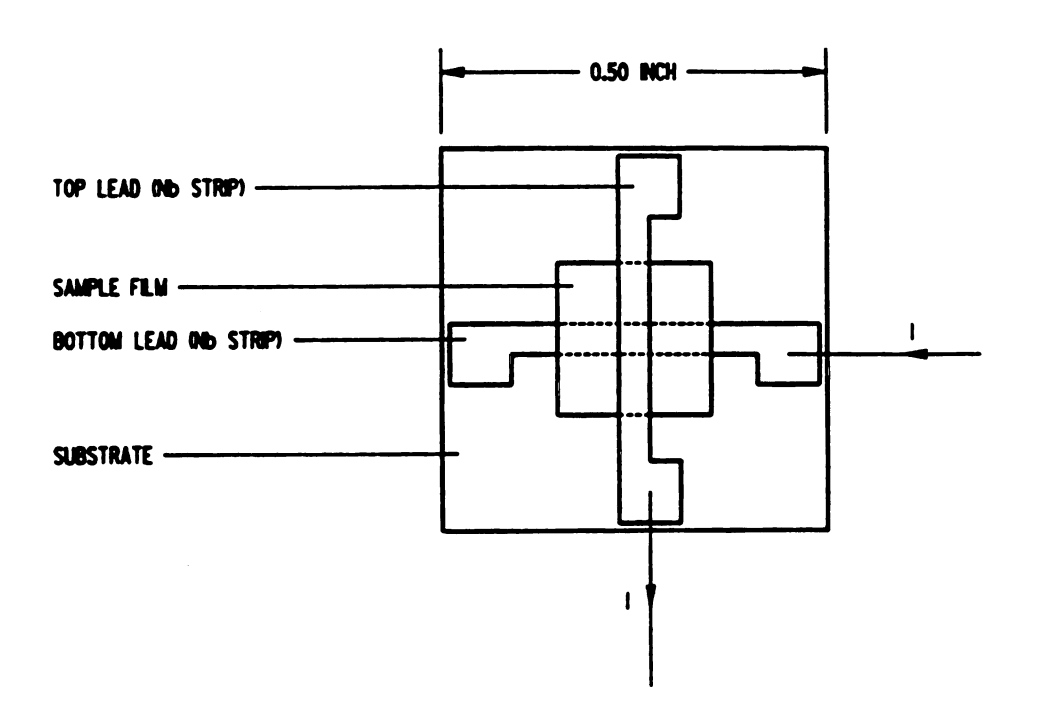


Figure 1.1 Sample design for perpendicular resistance measurement.

effective sample with a cross-section of  $1mm^2$ , the error in the calculated resistivity due to the fringing current is  $\sim 0.4\%$ .

The shapes of the leads and the sample film are formed by placing masks over the substrate during deposition. The masks must be changed without opening the vacuum chamber so that the interfaces between the leads and the sample film do not contain excessive amounts of impurities. The SPAMA, described in detail below, was designed to make this possible.

The shape of the film used to measure the resistivity parallel to the layers  $\rho_{par}$  is shown in Figure 1.2. This shape is made during deposition by pressing the sapphire substrate against a mask having the desired shape cut in it.

Samples for magnetization measurements were deposited on single crystal Si substrates with no mask. Both (111) and (110) orientations of Si were used.

### B. Sputtering System Overview

A schematic view of the sputtering system is shown in Figure 1.3.

The vacuum chamber is an 18 inch diameter by 19 inch high stainless steel cylinder with a copper wire seal flange at the top. In order to minimize the leak rate into the chamber the sputtering sources and all accessories are mounted on UHV conflat type flanges. Four ten inch flanges on the circumference of the tank accomodate the four sputtering source assemblies, each of which may be removed without disturbing the others. A cryopump (CTI Cryo-Torr 8 [CTI]) is mounted on another ten inch flange with a gate valve separating it from the chamber. This pump

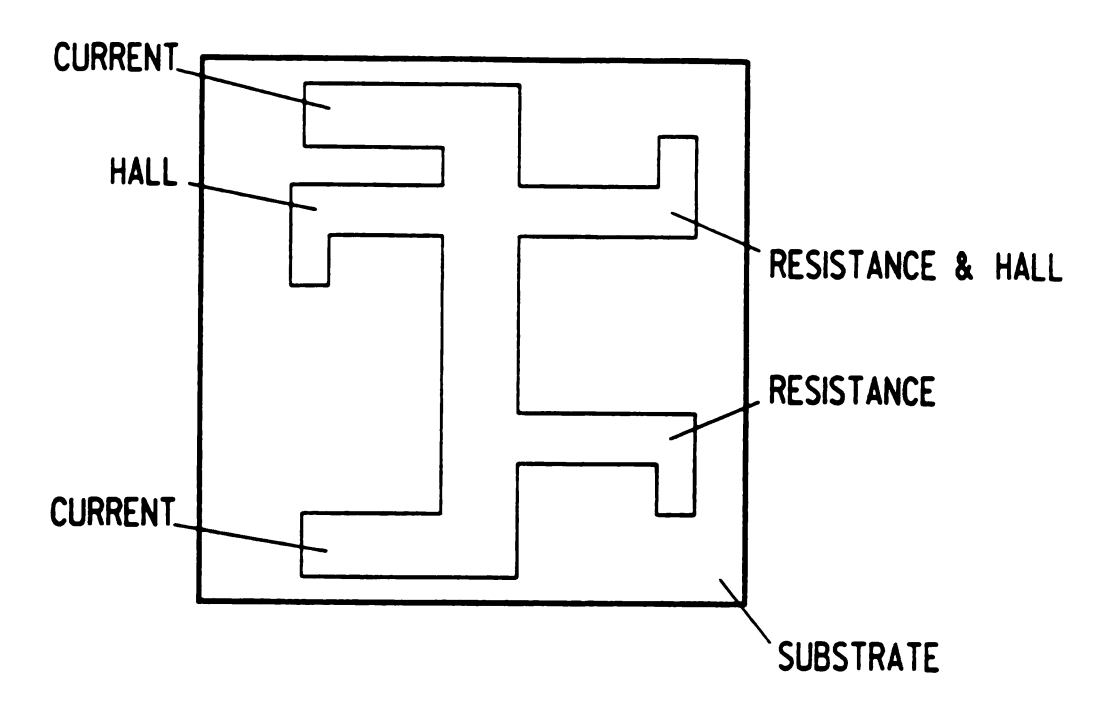
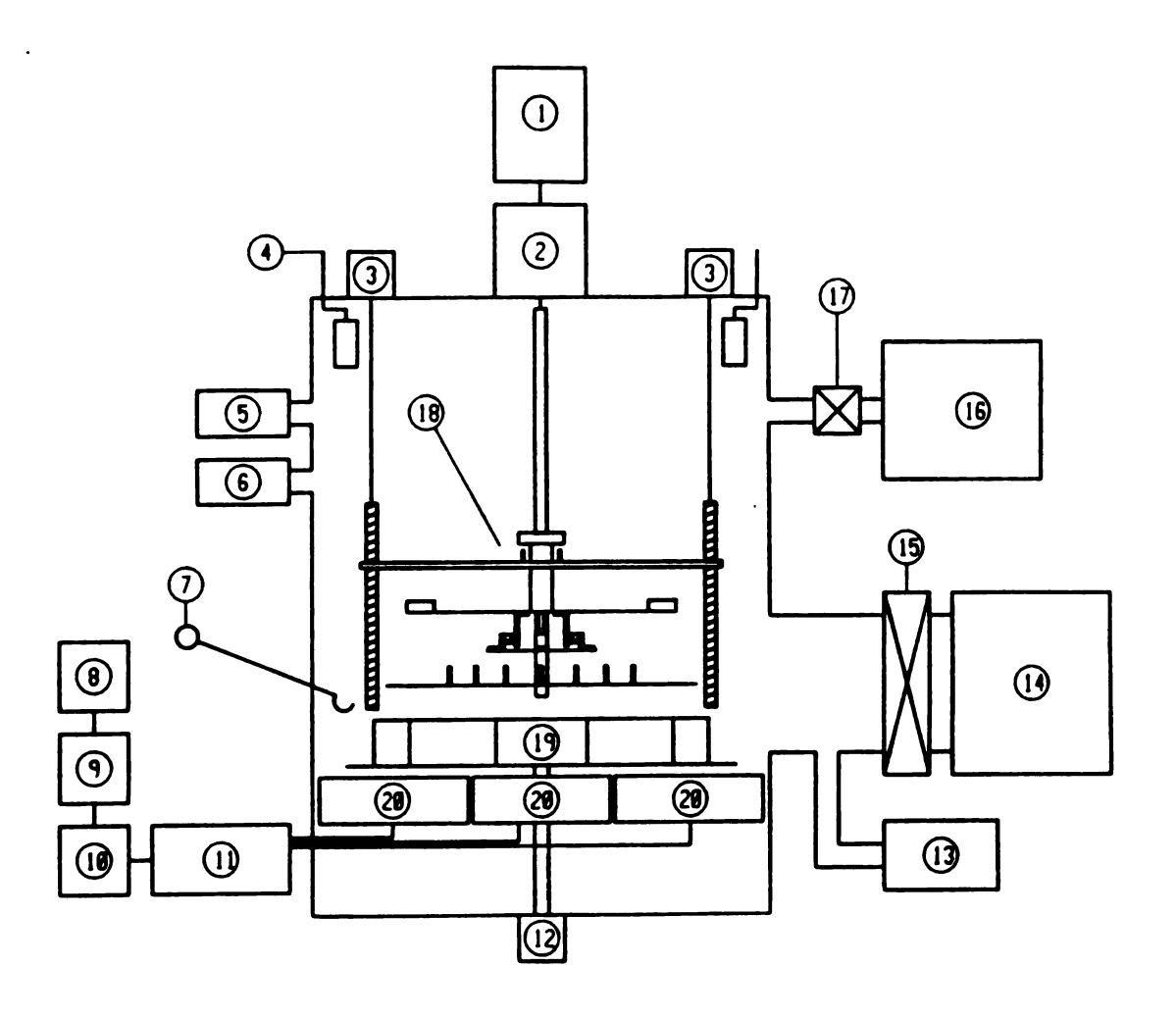


Figure 1.2 Sample design for parallel resistance measurement.



- 1. Stepping motor
- 3. Rotary feedthrough
- 5. Ionization gauge
- 7. Wobble stick
- 9. Cold-trap gas purifier
- 11. Gas flow controller
- 13. Residual gas analyzer
- 15. Gate valve
- 17. Bellows sealed valve
- 19. Shutter assembly

- 2. Rotary feedthrough
- 4. Meissner trap
- 6. Convectron gauge
- 8. UHP Ar tank
- 10. Hydrox gas purifier
  - 12. Rotary feedthrough
  - 14. Cryopump
  - 16. Mechanical pump
  - 18. SPAMA
- 20. Sputtering source

Figure 1.3 Schematic view of the sputtering system.

provides high pumping speeds (1500 l/s air, 4000 l/s water) with no oil vapor contamination. Typically the system is pumped to < 0.5 torr with the mechanical pump and then further pumped to  $< 1 \times 10^{-8}$  torr with the cryopump and the Meissner trap.

During sputtering the chamber contains Ar at a pressure of 3 to 15 mtorr. The Ar pressure is held constant ,within < 0.5%, by fixing the gas flow, via individual gas flow controllers for each gun, and throttling the cryopump by partially closing the gate valve. The gas supply is a cylinder of ultra-high purity Ar [UC]. After leaving the cylinder, the Ar is further purified by passing first through a cold trap, designed and built by Gregory Kenning, which is held at approximately 100K to freeze out the water vapor, and then through a Hydrox [MAT] gas purifier which removes impurities such as  $0_2$  and  $0_2$  by reaction with a hot Ti based alloy.

A Granville-Phillips [GP] model 303 vacuum process controller (VPC) is connected to an ionization gauge and one convectron gauge inside the chamber and an additional convectron gauge on the mechanical pump pumping line. The convectron gauges can measure pressures between 1 mtorr and 999 torr, however, their accuracy and resolution are poor in the pressure range used for sputtering. The ionization gauge is a Varian [VAR] type 564 Bayard-Alpert gauge tube with a range of 4 X 10<sup>-10</sup> to 0.1 torr. The ionization gauge is used to measure the pressure of the Ar gas during sputtering.

A Dycor [DYC] model M100 residual gas analyzer (RGA) is used before or after sample making to measure the partial pressure as a function of mass number of the residual gas in the vacuum chamber. It cannot be

used at sputtering pressures but the information it gives about the composition of the residual gas in the vacuum chamber at base pressure can be used to diagnose problems such as air or water leaks.

#### C. Sputtering Sources

There are four L. M. Simard [SIM] "Tri-Mag" sputtering sources located on a 10.875 in. diameter circle facing upward. Each source is part of an assembly, including water cooling lines, electrical connections and their appropriate vacuum feedthroughs, mounted on a 10 inch conflat flange which is bolted to the vacuum chamber. This design allows a source to be removed for repair or maintenance without affecting the operation of the rest of the system. Each source has two L. M. Simard power supplies: one to hold the sputtering target at a negative potential and one to create the plasma above the target. Target voltages from 0 to -1000 V, at up to 2 A current, are supplied by the TS/2 target power supplies. The plasma and filament currents are supplied by PD/200 power supplies for two sources and PD/20 power supplies for the other two.

Since the sources face upward, the substrate must be moved over the gun to make a sample (see Figure 1.4). The particle beams are shielded from each other by chimneys placed above the sources. The chimneys are fixed to a rotating table, controlled with an external handle via a bellows sealed rotary vacuum feedthrough, so that a source can be covered by rotating a closed chimney over it.

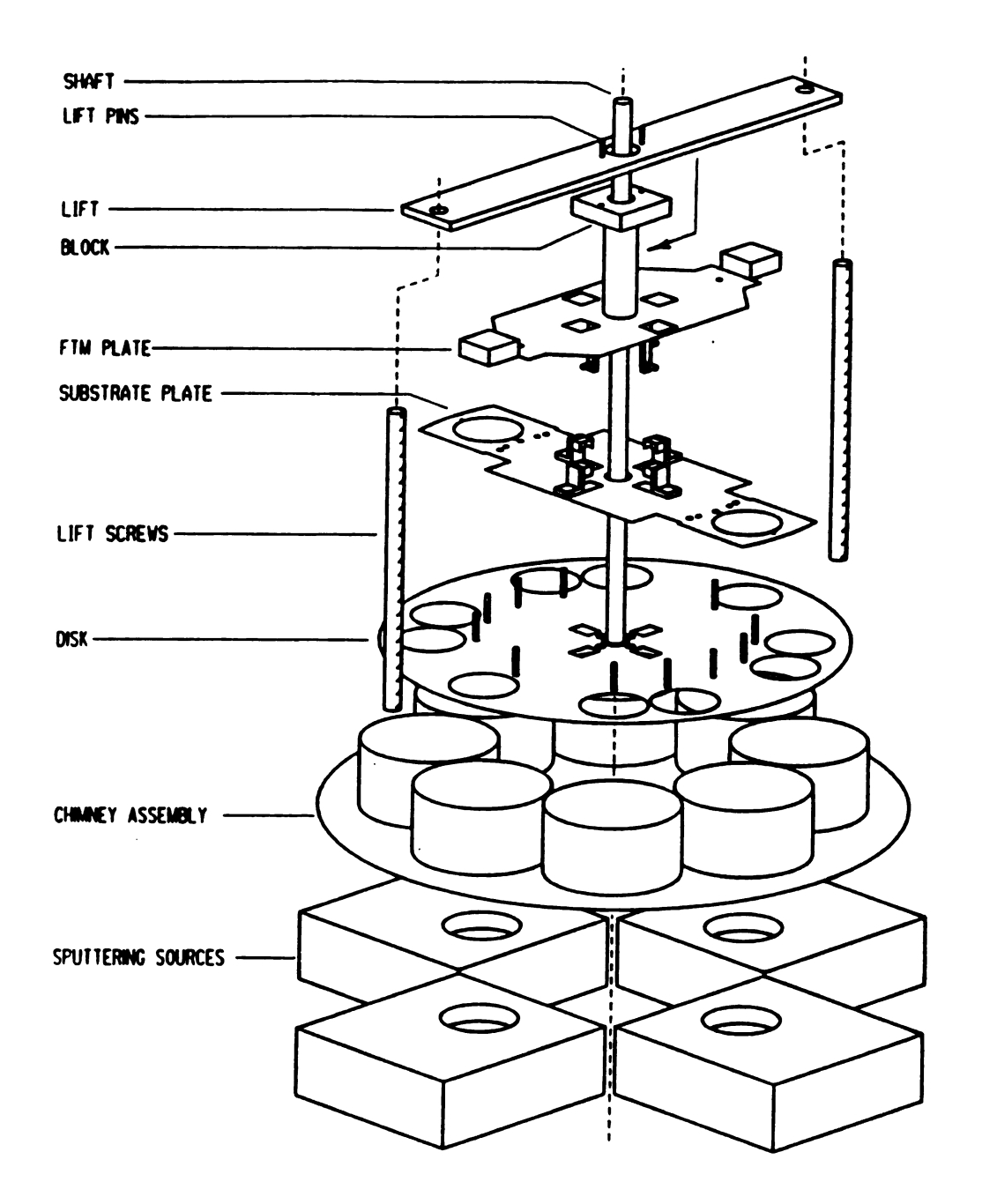


Figure 1.4 Exploded view of SPAMA, sources and chimneys.

#### D. Substrate Positioning and Masking Apparatus

The SPAMA is used for positioning both the substrates and two Temescal [TEM] model FTM-3000 quartz crystal film thickness monitors (FTMs) above the desired sources. An exploded view of the SPAMA, sputtering sources and chimneys are shown in Figure 1.4. The water cooling lines for the FTMs, which coil loosely around the shaft above the monitors, have been left out of the figure for clarity. The lift is shown above the block in the exploded view but during operation the lift fits below the block and lifts up on the block to raise the FTM plate.

A computer controlled stepping motor is mounted outside the vacuum chamber and is coupled to the stainless steel SPAMA shaft through a bellows sealed rotary vacuum feedthrough. Inside the vacuum chamber the aluminum SPAMA disk is fixed to the shaft. The disk has eight 2" diameter holes, which can be used to mount substrate holders or mask holders as described below, and two holes for the FTMs to go into when they are being used.

Two plates, the substrate plate and the FTM plate, can be lowered onto the disk when it is necessary to rotate them. The FTM plate is suspended from the lift and the substrate plate is suspended from the FTM plate. The small arms which come down from the bottom of the FTM plate are engaged with the arms which come up from the substrate plate to suspend the substrate plate. The vertical movement of the two plates is accomplished through the use of the lift, which moves up and down when the two lift screws are rotated by the operator. The screws are each fixed to separate bellows sealed rotary feedthroughs which are operated by a chain and hand crank mechanism outside of the chamber. When the lift is lowered the substrate plate moves downward until it

lands on top of the disk and stops moving, causing the arms to disengage. Once the arms are disengaged the substrate plate will rotate with the disk while the FTM plate remains fixed - still hanging from the lift.

There are two basic configurations of the SPAMA. In the first, the substrates are loaded into holders on the substrate plate and the masks are mounted in the disk. Mask changing is accomplished by using the lift to raise the substrate plate above the pins in the disk so that the disk can be rotated until the desired mask is positioned below the substrate. Lowering the substrate plate once again onto the disk completes the operation. When the substrate plate is lowered onto the disk, the pins from the disk go into holes in the substrate plate thus the allowed positions of the substrate plate are determined by these holes.

If the SPAMA is positioned so that the suspended substrate plate is rotated 90 degrees with respect to the FTM plate and the disk is such that the FTM holes are directly below the FTMs, as shown in Figure 1.5, then the SPAMA is in the "neutral position." Starting from this position, lowering the lift will put the substrate plate down on the disk, such that the substrates are covered by the disk, and will put the FTM plate down on the substrate plate with the FTMs positioned in the appropriate holes in the disk. The operator stops lowering the lift when the lift pins have disengaged from the block which supports the FTM plate, at which point the FTMs are free to rotate with the disk. A FTM can then be positioned over a source to measure its deposition rate.

In the second configuration, substrate holders are mounted in the disk and the substrate plate is not used. In this configuration it is

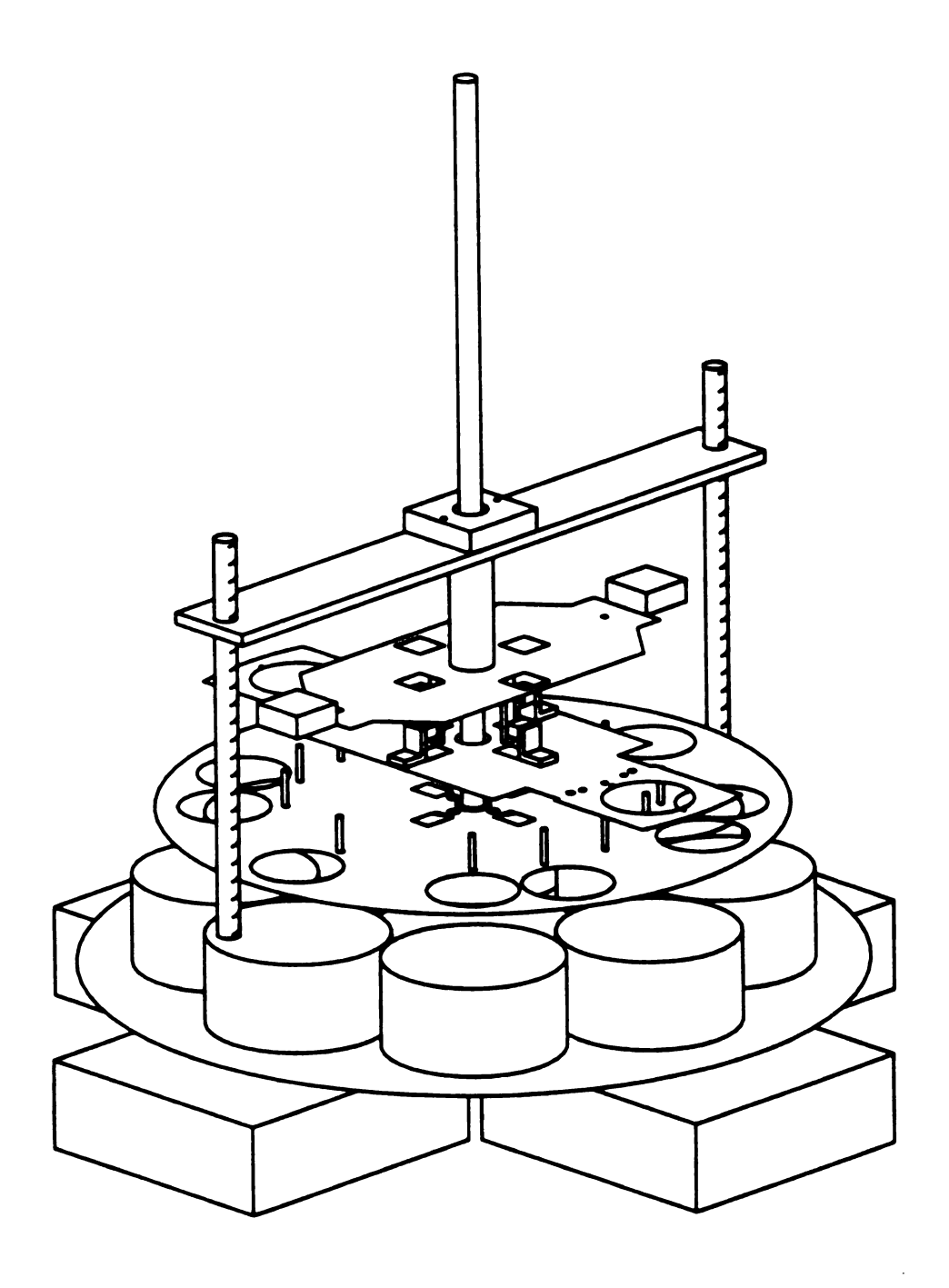


Figure 1.5 Neutral position of SPAMA.

possible to make 16 independent samples since each substrate holder holds two substrates and has a rotating shutter which allows substrates to be exposed individually or in pairs. A wobble stick is used to operate the substrate shutters. The FTM plate operates as before except that it will continue to move down with the lift until it rests on the disk, at which time the lift pins will begin to disengage.

Single material films are produced by positioning the substrate over the desired source with the time spent over the gun determining the thickness. Layered structures are produced in the same way by moving the substrate quickly between sources. Since the movement of the SPAMA disk is computer controlled, errors in thickness due to timing errors are negligible.

The rotary feedthrough for the shaft is a Temescal [TEM] model BR-1F. The two rotary feedthroughs for the lift screws are Vacuum Generators [VG] model RD6. The stepping motor is a Compumotor [COM] model M106-178.

When making perpendicular transport samples, there is typically a 2 minute delay while the mask is being changed. During this 2 minutes the sample surface, which will be the interface between a strip and the sample film in the completed sample, is exposed to the atomsphere in the sputtering chamber. To minimize the effect of the exposure, we deposit a 75Å overlayer of comparatively unreactive Ag onto the first Nb strip and we always begin and end the making of the LMS sample film with a layer of Ag. Following this procedure insures that any impurities deposited during the 2 minute delay will be sandwiched between layers of Ag.

#### E. Computer interfacing and software

Figure 1.6 shows how information is passed to and from the IBM Personal Computer XT. The computer controls the production of samples by sending commands to the stepping motor indexer (PC21). These are high level commands that specify angular accelerations, velocities and positions as well as defining loops and time delays. The PC21 sends pulses, representing steps, to the motor driver and can be instructed to send carriage return characters back to the computer to signal the execution of selected commands. The computer communicates with the PC21 via the I/O memory addresses 300-303. Details of the communication scheme can be found in the Compumotor PC21 indexer manual. The computer prompts the operator to move chimneys or operate the SPAMA lift when necessary. During production of the samples the Ar pressure and the target voltages and currents are monitored, to aid the operator in keeping these parameters constant, and recorded on disk for future The analog-to-digital converters (ADCs) on a Data reference. Translation [DT] DT-2801 I/O board are used to read the target parameters from outputs on the TS/2 power supplies. The DT-2801 has 8 differential ADC inputs assigned as shown in Figure 1.6. The two digital-to-analog converters (DACO and DAC1) are set aside for control of the PD/200 plasma power supplies. The computer communicates with the DT-2801 via I/O memory addresses 2BC-2BD and DMA channel #1. Details of the communication scheme can be found in the Data Translation DT-2801 manual. The RGA and the VPC communicate via RS232 interfaces designated as devices COM1 and COM2 respectively.

The control software is organized into subroutines as shown in Figure 1.7. The POSITION subroutine is used by the operator to set the

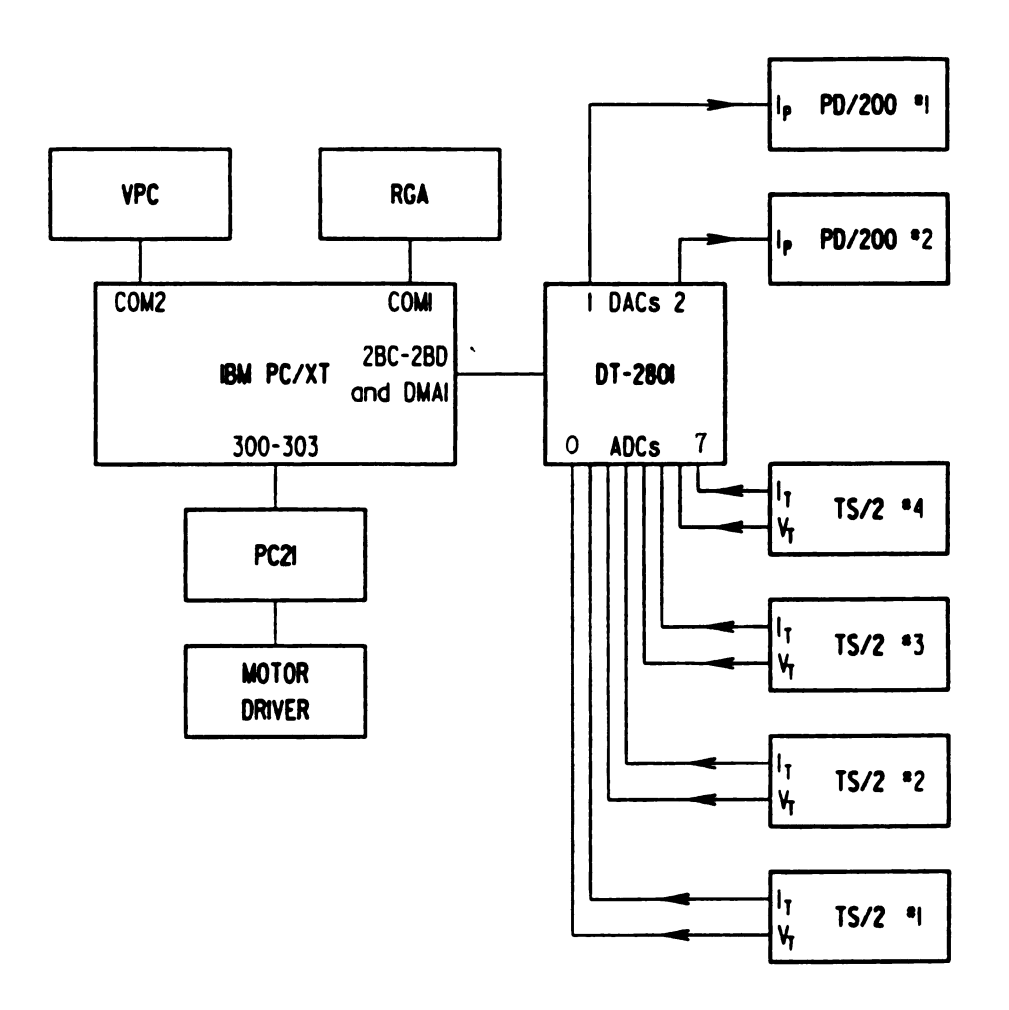


Figure 1.6 Connections to IBM Personal Computer XT.

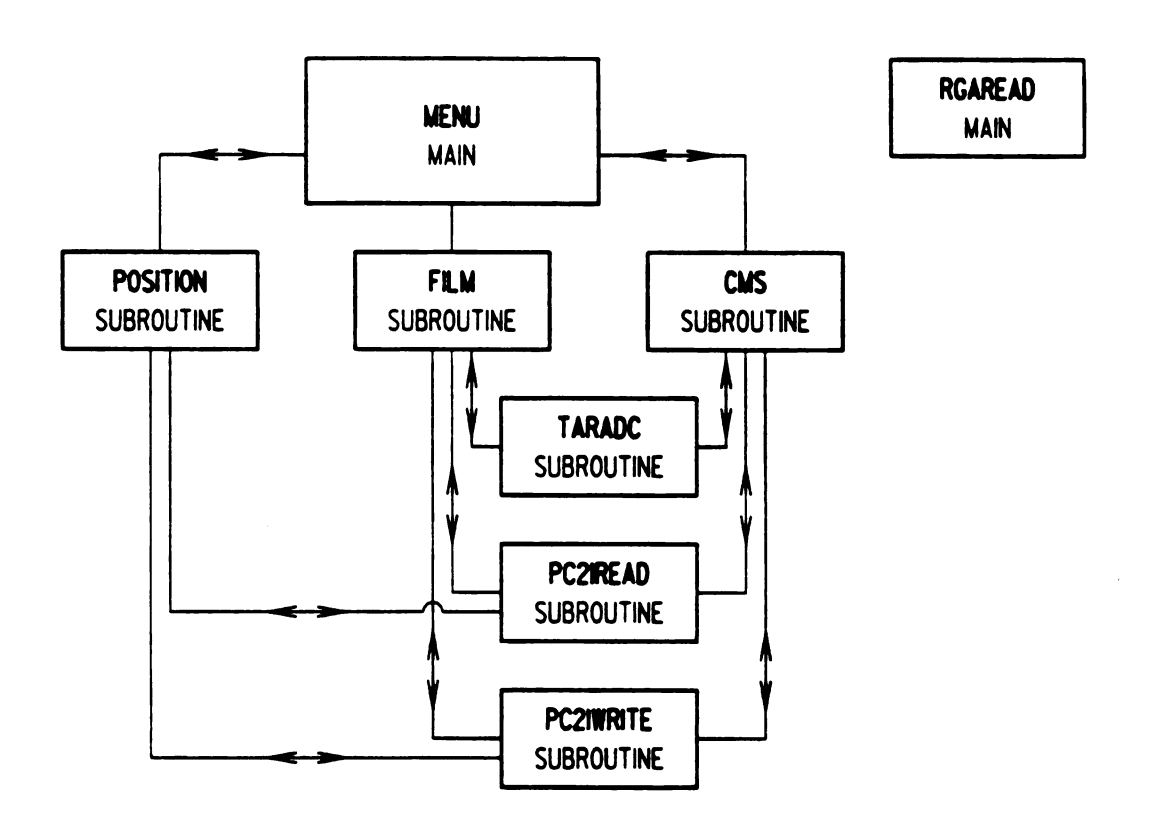


Figure 1.7 Control software organization.

stepping motor to the "zero" reference position at the start of the run. The motor zero position is the position of the motor when the SPAMA is in the neutral position. The CMS subroutine is used to produce compositionally modulated structures (periodic structures formed by a repeated bilayer, metallic or otherwise). The FILM subroutine is used to produce simple films with up to ten layers. Both FILM and CMS contain routines to input sample parameters from disk or keyboard, measure deposition rates, move samples to the window or wobble stick, create disk files which document the individual samples and print such documents. TARADC is the subroutine which samples the target power supply parameters and returns the current and voltage averaged over a 0.33 second interval. PC21READ and PC21WRITE are subroutines for communicating with the PC21 indexer. RGAREAD is a program which sets the RGA parameters, inputs data, and outputs a histogram of partial pressure versus mass number.

#### F. System Performance

Two figures of merit for sputtered superlattices (FMSS) have been proposed by C.M. Falco [FAL84]. The first, FMSS1, estimates the upper limit of the concentration of impurities incorporated into the film expressed in volume percent. The second, FMSS2, estimates the upper limit fraction of a monolayer of impurity atoms which will form at the interfaces. Falco presents these in the following form:

FMSS1 
$$< 9.1 \times 10^{4} \frac{[P_{\text{sputt}} \text{ (mTorr)}] [Q_{\text{leak}} \text{ (scem)}]}{[R_{\text{sputt}} \text{ (Å/s)}] [Q_{\text{Ar}} \text{ (scem)}]}$$
 (1.1)

$$[t (sec)] [P_{sputt} (mTorr)] [Q_{leak} (smmm)]$$

$$= [Q_{Ar} (secm)]$$
(1.2)

The definitions of the variables used and their typical values for this system are shown in Table 1.1.

Table 1.1 Typical production parameters and FMSS

Parameter	Typical value	Definition
Psputt	5 mtorr	Ar pressure while sputtering
R Sputt	10 Å/s	Deposition rate
Q <sub>leak</sub>	$3 \times 10^{-3} \text{ seem}$	Leak rate of impurity gasses
Q <sub>Ar</sub>	90 seem	Total flow of sputtering gas (A
t	0.22 s	Time lapse between layers
Results for	this system:	
FMSS1 < 1.5	%	
FMSS2 < 0.0	17 monolayer	

The leak rate into the chamber was estimated using a typical base pressure of 1  $\times$  10<sup>-8</sup> torr with a pumping speed of 4000 1/s (since the majority of the residual gas at base pressure is water the pumping speed for water is used). The result is shown in Table 1.1. Both FMSS are near the low end of the spectrum of values possible for sputtering systems now in use.

If the deposition rate is measured as a function of angular displacement from the center of the target it is found to drop to zero

between 20 and 35 degrees depending upon the size of the hole in the chimney top. Considering that the sources are separated by 45 degrees and that the time between sources is approximately 0.2 s it is clear that the shielding is sufficient to prevent mixing in either case.

#### G. X-ray Diffraction Theory

The structure of a real LMS may differ from that of an ideal superlattice in many ways. In addition to the flaws one might find in any other crystal, there are deviations from perfection that are unique to layered structures. Below is a list of flaws which can be addressed and in some cases quantified by X-ray diffraction.

- 1. Diffusion may occur at the interface causing a loss of chemical order.
- 2. If the two components of the LMS are not lattice matched there will be induced strains and dislocations at the interfaces. In some cases the strain energy may actually lead to the stablization of a different phase of one of the components.
- 3. The period may not be constant throughout the structure. In this case there is a loss of chemical order even though the structural order may be good. The variation in period may be caused by deposition rate fluctuations during sample production or nonuniform layers due to island formation.
- 4. The sample may be made of crystallites with various orientations. Many LMS, including Ag/Co, are polycrystalline and textured [Mc85]. By textured we mean that the crystallites have a dominant orientation, although other orientations may be present. Typically when a film is produced by sputtering or evaporation the

dominant orientation is the one which results in the most dense crystallograppic planes being parallel to the surface of the substrate. Thus, for metals with FCC, HCP and BCC structures we find (111), (0001) and (110) textures, respectively.

A structure which is made up of small blocks with slight differences in orientation, where each block is nearly a perfect crystal, is called a mosaic structure. Since most LMS are made up of small crystallites and are textured, it is often useful to think of a LMS as a mosaic structure.

When analyzing the X-ray diffraction patterns for any crystal one will find that the peaks have finite width. This width has two main contributions; instrumental width and that due to the coherence length of the crystal. After correcting for the instrumental contribution it is possible to work backwards from the peak width  $2\Delta\theta$  to find the coherence length L using the Scherrer equation [WA69]

$$2\Delta\theta \approx \frac{\lambda}{L\cos\theta}$$
. (1.3)

Since in reality the crystallites have a distribution of sizes, the coherence length is just the apparent dimension of the mosaic blocks in the idealized structure.

The geometry for  $\theta$ -2 $\theta$  diffraction and rocking curves is shown in Figure 1.8. When doing  $\theta$ -2 $\theta$  diffraction  $\phi$  is fixed at zero so that the incident and reflected angles are equal making the momentum transfer normal to the layers. Thus, in this case, the peak width gives the coherence length in the normal direction. Rocking curves are generated by varying the rocking angle  $\phi$ , while keeping  $\theta$  and  $2\theta$  fixed. The

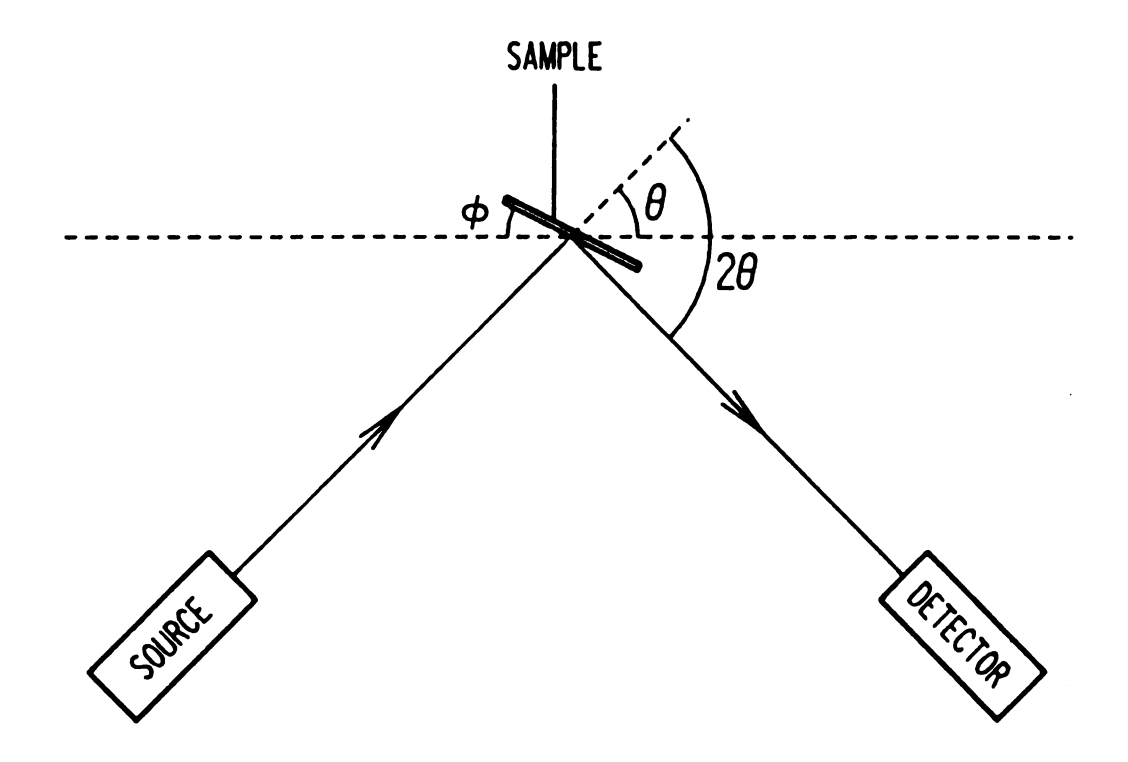


Figure 1.8 X-ray diffractometer geometry.

rocking curve shows how the orientations of the mosaic blocks are distributed.

The  $\theta$ -2 $\theta$  diffraction patterns of Ag-Co LMS typically show a series of satellite peaks, the spacing of which is determined by the period of the structure. In order to learn more about the structure one needs a specific model from which peak intensities can be calculated. A useful and simple model proposed by Segmuller and Blakeslee [Se73] is the one-dimensional periodic step function or "step" model. In this model each layer is made up of an integer number of atomic planes with the same planar spacing as in the bulk material (see Figure 1.9). In [Se73] the structure factor is given as

$$S(q) = \frac{\sin(N\Lambda q/2)}{\sin(\Lambda q/2)} \left\{ f_1 \frac{\sin(n_1 a_1 q/2)}{\sin(a_1 q/2)} + f_2 \frac{\sin(n_2 a_2 q/2)}{\sin(a_2 q/2)} \exp(i\Lambda q/2) \right\}$$
(1.4)

where N is the number of periods in the structure, q is the momentum-transfer wave vector  $(q = \frac{4\pi}{\lambda} \sin\theta)$  where  $\lambda$  is the X-ray wavelength) and  $f_i$  is the atomic scattering factor for material i. The diffracted intensity corresponding to equation (1.4) is

$$I \sim F^{2}(N,\Lambda) \left\{ f_{1}^{2} F^{2}(n_{1},a_{1}) + f_{2}^{2} F^{2}(n_{2},a_{2}) + 2f_{1}f_{2}F(n_{1},a_{1})F(n_{2},a_{2})\cos(\Lambda q/2) \right\}$$
(1.5)

where

$$F(n,a) = \frac{\sin(naq/2)}{\sin(aq/2)}.$$

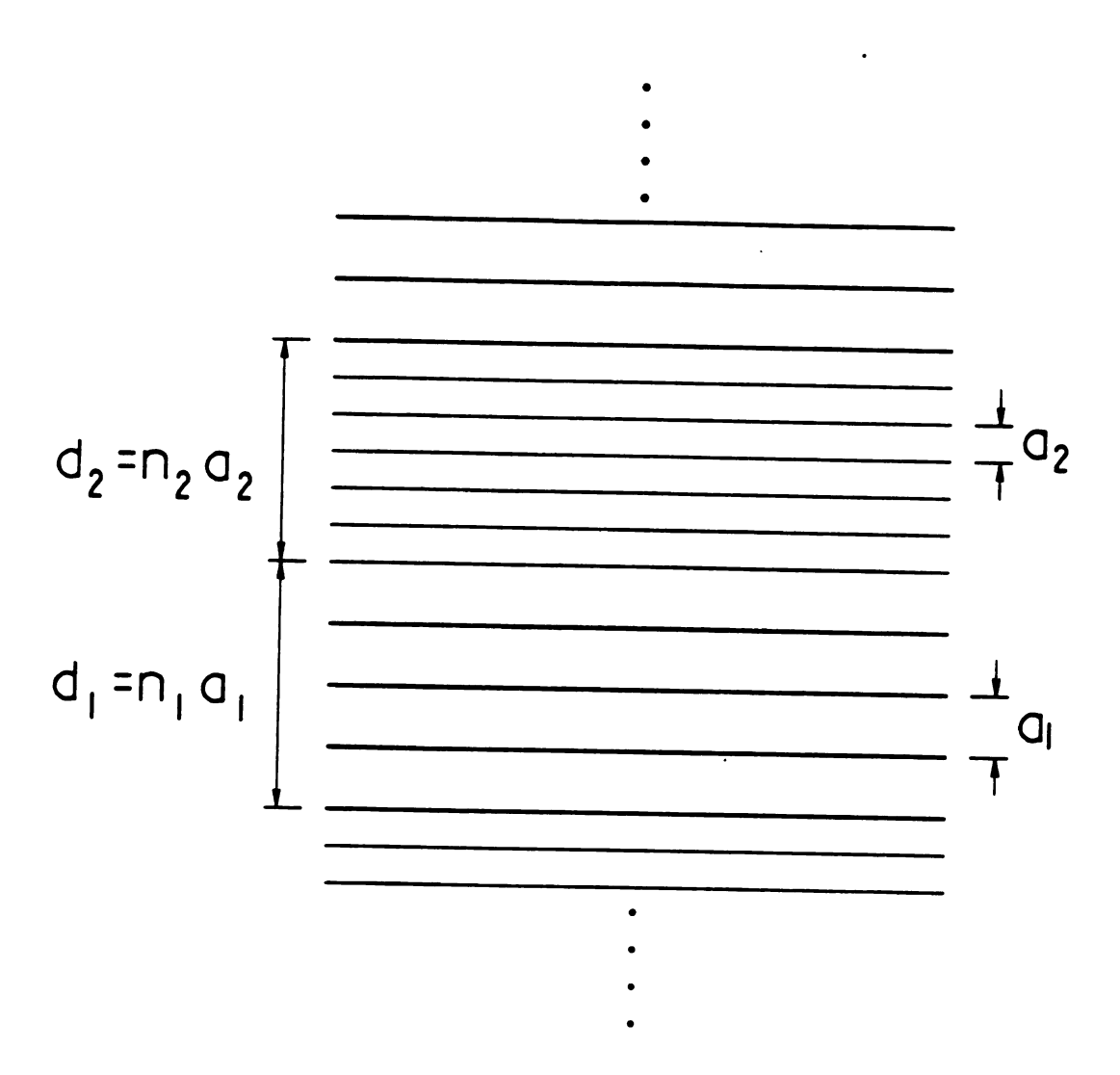


Figure 1.9 Step model of a LMS.

After carefully working through the derivation of equation (1.5) we find that the expression for the intensity should be

$$I \sim F^{2}(N,\Lambda) \left\{ f_{1}^{2} F^{2}(n_{1},a_{1}) + f_{2}^{2} F^{2}(n_{2},a_{2}) + 2f_{1}f_{2}F(n_{1},a_{1})F(n_{2},a_{2})\cos((\Lambda + a_{1} - a_{2})q/2) \right\}.$$
(1.6)

In the system that Segmuller and Blakeslee were interested in (Ga-GaAs $_{1-x}P_x$ ) the difference  $a_1-a_2$  is very small compared to  $\Lambda$  so that they were justified in neglecting it. For Ag-Co that difference is still fairly small compared to  $\Lambda$  ( $\frac{a_1-a_2}{\Lambda}$  < 0.05) but equation (1.6) was used for the calculations nonetheless.

We must define what we mean by the scattering factors  $\mathbf{f}_i$  in the step model. Equation (1.6) is the diffracted intensity from a one-dimensional chain of atoms. If the LMS were made up of materials with the same structure and lattice constant, then treating the  $\mathbf{f}_i$  simply as atomic factors would be correct. But in the case of Ag-Co the materials have different structures and furthermore the atomic planes in question have different in-plane parameters for the different materials. The differences are taken into account by defining the scattering factors  $\mathbf{f}_i$  as the product of the atomic scattering factor  $\mathbf{f}_{\circ i}$  and the in-plane atomic density  $\alpha_i$  of material i:

$$f_{i} = f_{o_{i}} \alpha_{i}. \tag{1.7}$$

That is, we assume that the scattering amplitude from a plane is proportional to the density of atoms in the plane. To improve on this assumption one would have to know the atomic structure at the interface

so that a three-dimensional unit cell could be defined. For Ag-Co and most other LMS these details of the structure are not known.

We wish to use the step model result to calculate  $\theta$ -2 $\theta$  spectra which can be compared to the experimental spectra. Before the comparison can be made there are three corrections which must be applied to equation (1.6) [Wa69].

1. The Debye-Waller correction takes into account the reduction in the atomic scattering factors due to the thermal vibrations of the atoms. The effective scattering factor f has the form

$$f = f_o \exp(\frac{-B\sin^2\theta}{\lambda})$$
 (1.8)

where  $f_{o}$  is the usual atomic scattering factor and B is the Debye parameter.

2. The intensity depends upon the polarization of the incident beam. For an unpolarized beam the intensity is modified by the polarization factor

$$\frac{1}{2} \left\{ 1 + \cos^2(2\theta) \right\} \tag{1.9}$$

3. The angular velocity factor is a correction that must be applied if one is calculating intensities measured by a diffractometer which sweeps through  $\theta$  with constant angular velocity  $\mathring{\theta}$ . The correction arises from the fact that if  $\mathring{\theta}$  is constant then the rate at which a point in the reciprocal lattice passes through the Ewald sphere is a function of  $\theta$ . This correction is usually put together with equation (1.9) to form the "Lorentz-Polarization" factor

$$LP = \frac{1 + \cos^2(2\theta)}{2\sin(2\theta)}.$$
 (1.10)

Applying the corrections to equation (1.6) yields the corrected intensity

$$I_{corr} \sim F^{2}(N,\Lambda) \left\{ f_{01}^{2} \alpha_{1}^{2} \exp\left(\frac{-2B_{1} \sin^{2} \theta}{\lambda^{2}}\right) F_{1}^{2} + f_{02}^{2} \alpha_{2}^{2} \exp\left(\frac{-2B_{2} \sin^{2} \theta}{\lambda^{2}}\right) F_{2}^{2} + 2f_{01} f_{02} \alpha_{1}^{2} \alpha_{2} \exp\left(\frac{-(B_{1} + B_{2}) \sin^{2} \theta}{\lambda^{2}}\right) F_{1} F_{2} \cos\left((\Lambda + a_{1} - a_{2}) q/2\right) \right\} LP \quad (1.11)$$

where  $F_i = F(n_i, a_i)$  and  $F(n_i, a_i)$  are as defined above.

Co is known to occur in three different structures. Bulk Co at room temperature is mostly hcp with a small fcc component but in thin films a pure bcc phase has been stabilized on a substrate of GaAs [Pr85]. We have shown with X-ray diffraction measurements that thick Co films (5KÅ) produced in our sputtering system are predominantly hcp with a (0001) texture, however, there is no reason to believe that the Co structure will be the same in a LMS. In order to show the effect of the Co structure on the X-ray diffraction spectra, three model spectra have been calculated for each A of interest. The three cases are hcp-Co (0001), bcc-Co (110) and fcc-Co (111) layered with fcc-Ag (111). Table 1.2 gives the parameters used for fcc-Ag and the three phases of Co in Calculating the intensities. The case of bcc-Co (111) was also Considered but these results are not shown since the calculated spectra were not at all similar to the experimental spectra.

Figure 1.10 illustrates the basic features of the  $\theta$ -2 $\theta$  spectra of Ag-Co. The top curve (heavy line) is a measured spectrum from a  $\Lambda$ \*21.5 Å sample with equal Ag and Co layer thicknesses. The rapid rise on the far left is the edge of the beam's central maximum and the peak nearest to it is the first order peak due to the superstructure. The curve

Table 1.2 Parameters for step model calculations

material	d	а	В
	(Å)	(Å <sup>-²</sup> )	(Ų)
fcc-Ag (111)	2.36	0.138	0.54
hcp-Co (0002)	2.035	0.183	0.27
fcc-Co (111)	2.05	0.183	0.27
bcc-Co (110)	1.99	0.179	0.27
bcc-Co (111)	1.62	0.146	0.27
	<u>-</u> -		

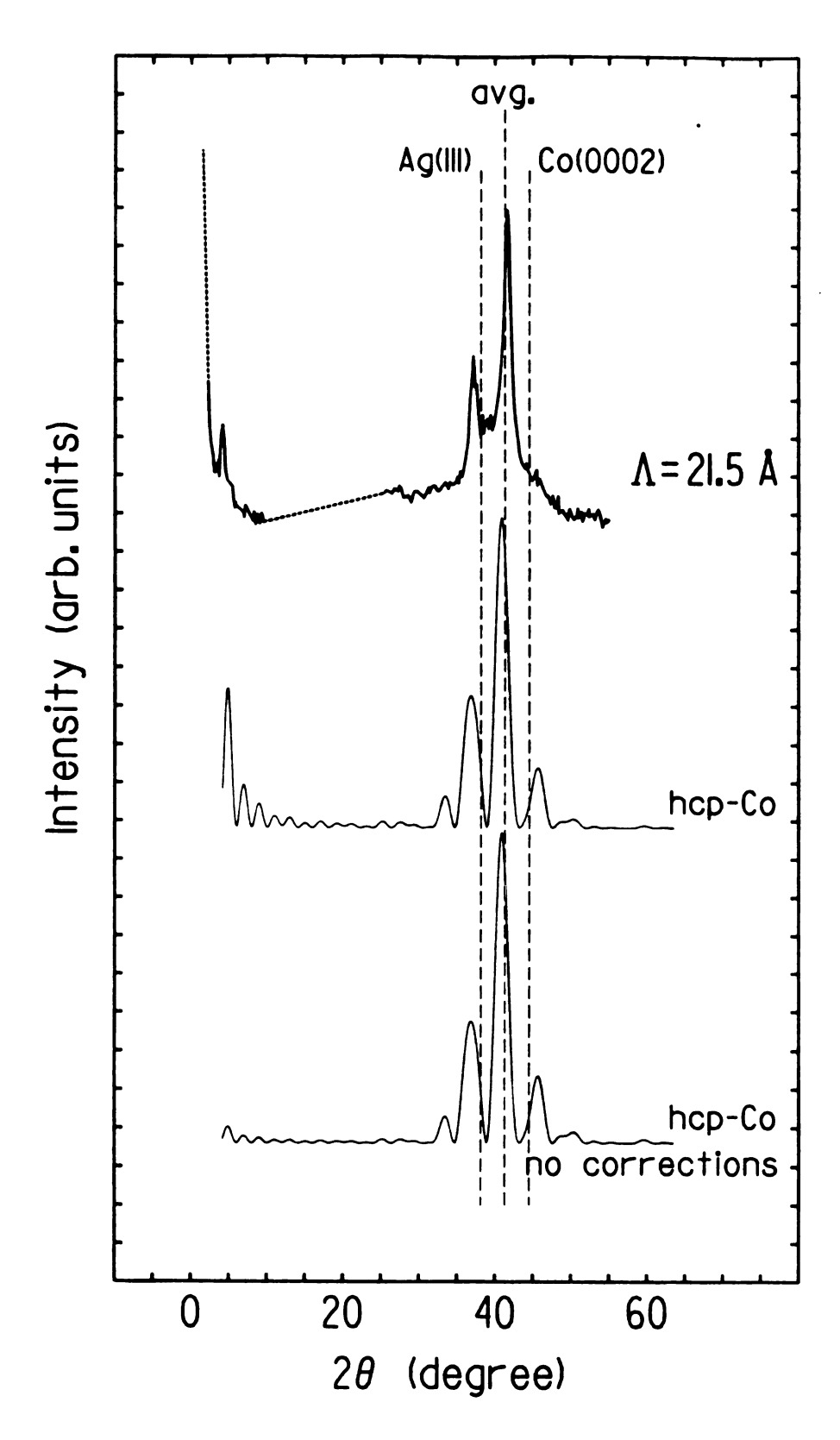


Figure 1.10  $\theta$ -20 spectra for  $\Lambda$ =21.5 $\Lambda$ : Experimental and step model.

labeled hcp-Co is a step model calculation using hcp-Co. The number of periods in the model structure (N) was chosen to be 2 in order to produce a peak width similar to that found in the measured spectrum. The bottom curve shows the result of a calculation which did not include the Lorentz-polarization and Debye-Waller corrections.

The basic features of both calculated and experimental spectra are the following.

- 1. There are peaks at low angles which can be identified as low order diffraction peaks from the superstructure.
- 2. There are peaks near the positions where the bulk material peaks would be found. For large  $\Lambda$  they appear as slightly broadened bulk peaks of Ag and Co but as  $\Lambda$  decreases the individual satellite peaks become distinguishable.
  - 3. The satellite peak corresponding to the average lattice spacing

$$d_{ave} = \frac{\Lambda}{n_1 + n_2}$$
 (1.12)

increases in intensity as  $\Lambda$  decreases. For equal layer thickness Ag-Co LMS the average lattice peak falls at approximately  $2\theta$ =41.3°. In Figure 1.10 the average lattice peak is the most intense due to the relatively small period.

The positions of the low-angle peaks and the satellites are determined by the prefactor in equation (1.6)

$$F^{2}(N,\Lambda) = \frac{\sin^{2}(N\Lambda q/2)}{\sin^{2}(\Lambda q/2)}$$

which is sharply peaked when the Bragg condition for the artificial period  $\boldsymbol{\Lambda}$ 

$$n\lambda = 2\Lambda \sin\theta \tag{1.13}$$

is satisfied. The integer n is the order of the peak.

For the high-angle peaks it is often convenient to index the satellite peaks with respect to the average lattice peak. Let m be the satellite index such that m=0 for the average lattice peak (which has  $n=n_1+n_2$ ). We can then rewrite equation (1.13) as

$$q = \frac{2\pi m}{\Lambda} + b \tag{1.14}$$

where b is a constant for a particular sample. Clearly, if we plot the experimental data as q versus m we can expect it to be linear with slope  $\frac{2\pi}{\Lambda}$  if the structure is a LMS. Figure 1.11 is such a plot for sample 3805.

# H. X-ray Diffraction: Experimental Results and Model Calculations

All of the  $\theta$ -20 X-ray diffraction measurements shown here were made with a Rigaku [RIG] Geigerflex diffractometer using Cu-K $_{\alpha}$  radiation ( $\lambda$ =1.5418Å). The rocking curve measurements were made with a Huber [HUB] triple-axis diffractometer and a Rigaku Rotaflex rotating anode source using Mo-K $_{\alpha}$  radiation ( $\lambda$ =0.7107Å). Some  $\theta$ -20 measurements were made on the triple-axis machine and they agree with those made on the first machine but are not shown here.

The low-angle peaks are only rarely observed since the equipment used is not optimized for low-angle diffraction from thin films. If  $\Lambda$  is large then the low-order peaks are lost in the central maximum. If  $\Lambda$  is small the first order peak position is outside the central maximum but its intensity is very small, due to the rapid drop with increasing angle of the velocity factor, making it again unobservable. Low-angle peaks were only seen for  $\Lambda$  near 20Å (as in Figure 1.10) when the first

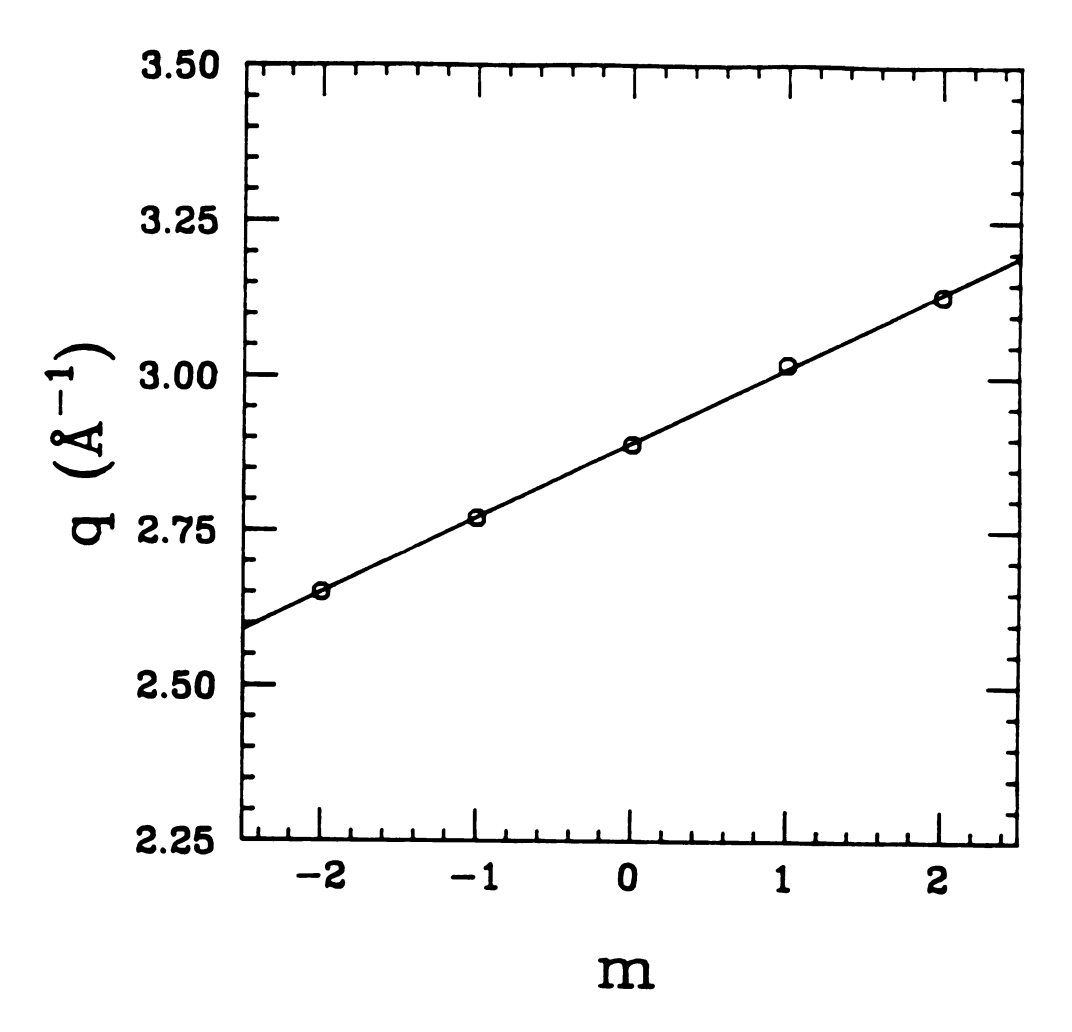


Figure 1.11 Momentum transfer q versus index m for sample 3805.

order peak is in the small region of  $2\theta$  where it is observable with the diffractometer used.

Figures 1.12 through 1.19 show experimental spectra and spectra calculated with equation (1.11). The experimental curves are shown at the top of each figure and are labeled with the period as determined from the spacing of the peaks. All of the samples discussed here have nominally equal thickness Ag and Co layers. For each experimental spectrum there are three model calculations shown; one for each of the three structure combinations using the parameters shown in Table 1.2. Only the high-angle satellite peaks are shown because of the difficulties in obtaining low-angle peaks. Positions of "bulk" peaks corresponding to the fcc-Ag (111) and hcp-Co(0002) planes as well the position of the average lattice peak for the LMS made with hcp-Co are shown on the figures for reference.

One difficulty in applying the step model is the restriction that there be an integer number of atomic planes in each layer ( $n_1$ ,  $n_2$  integer). This restriction makes it impossible to choose parameters such that the layers are of equal thickness and the period is equal to the measured period of the LMS. For the calculated spectra shown, if the parameters  $n_1$  and  $n_2$  could not be chosen so that the thicknesses were within a few tenths of an angstrom then they were chosen to make  $d_{Ag} \geq d_{Co}$ . This criterion was used because there is some evidence that the LMS studied were Ag rich, as explained later in this chapter, and because the best fits to experiment were obtained for the Ag rich case. The extra Ag shifts the average lattice peaks in the simulations to the left, particularly for the small A simulations.

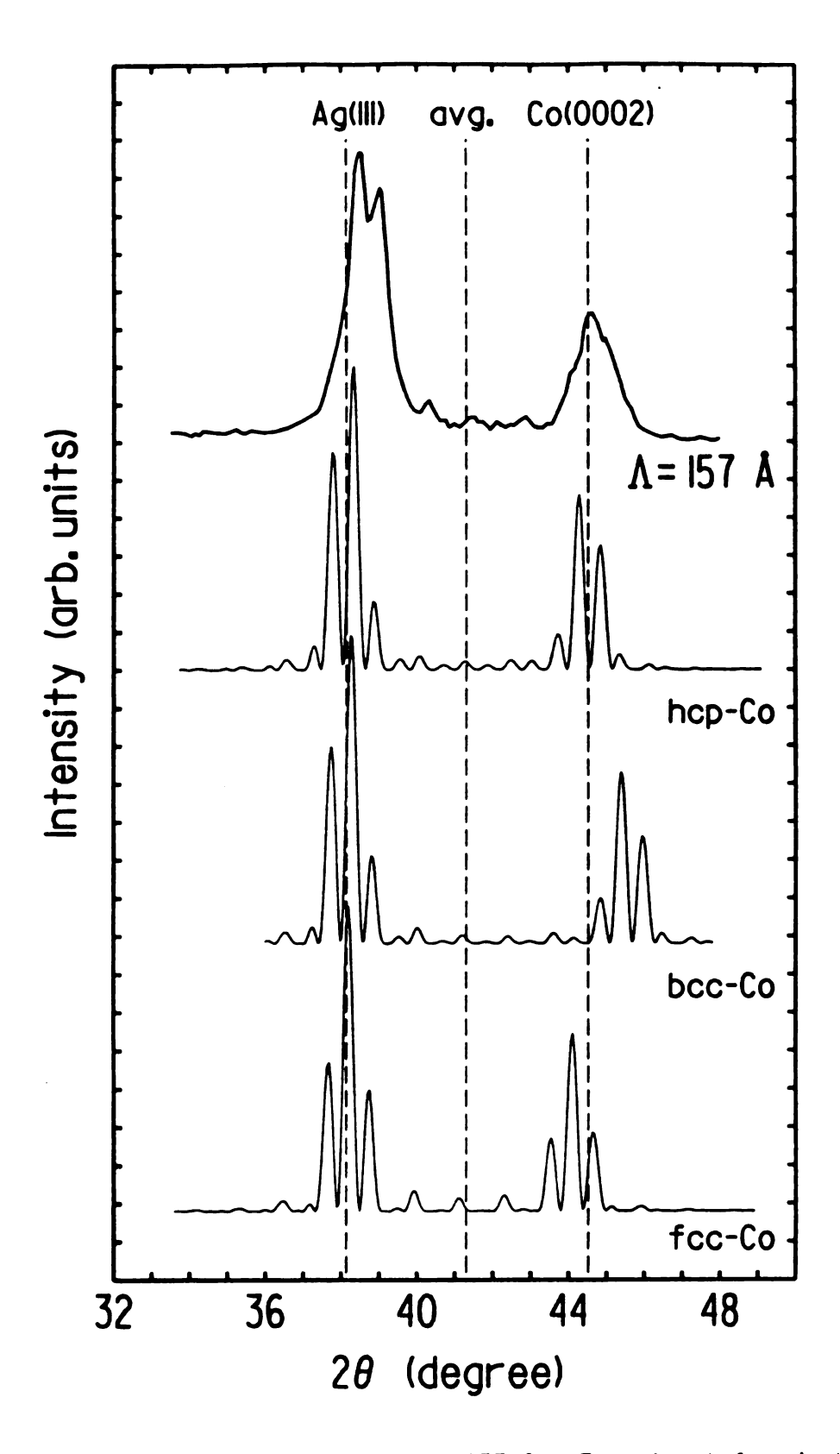


Figure 1.12  $\theta$ -20 spectra for  $\Lambda$ =157 Å: Experimental and step model.

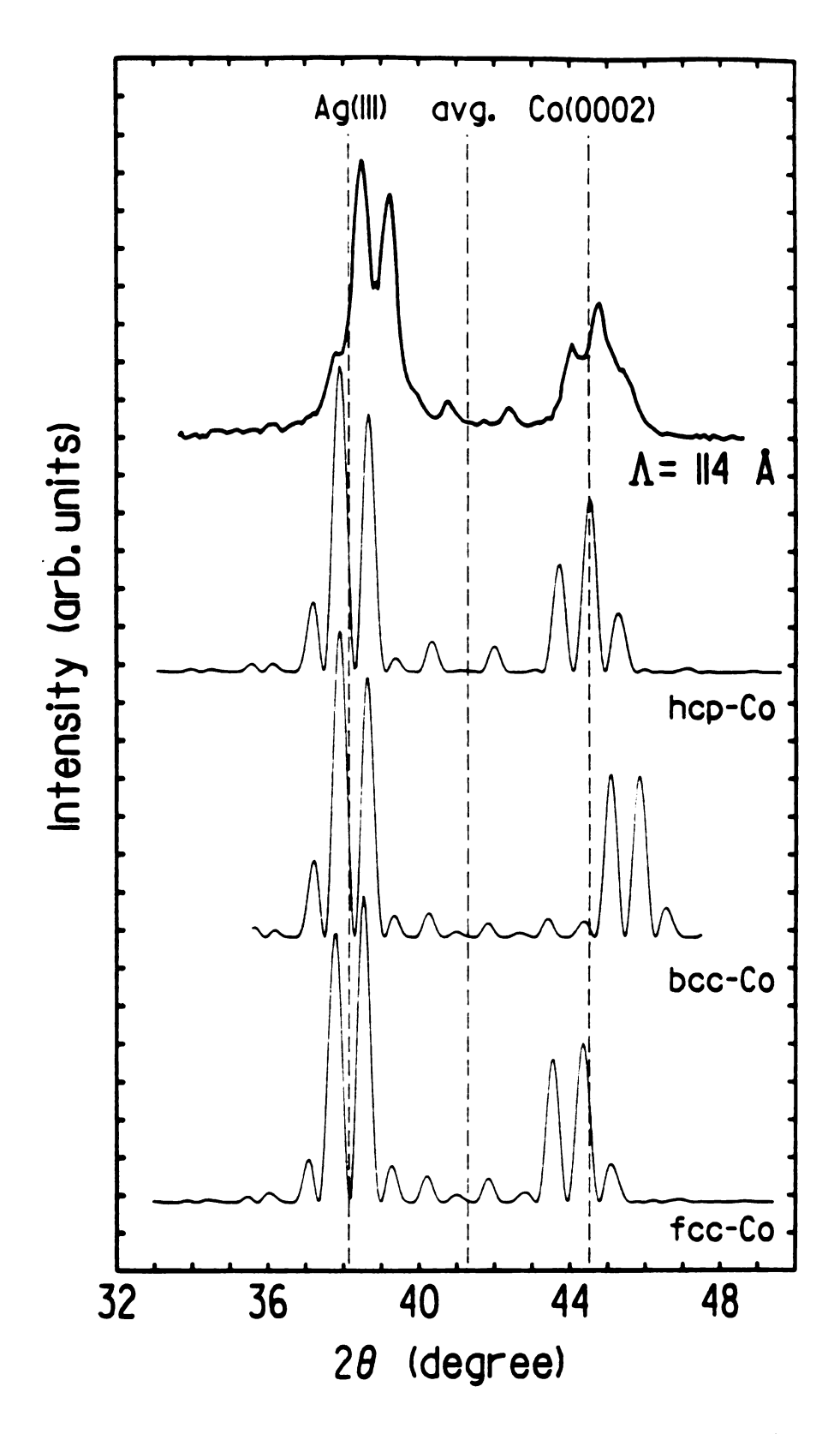


Figure 1.13  $\theta$ -20 spectra for  $\Lambda$ =114 Å: Experimental and step model.

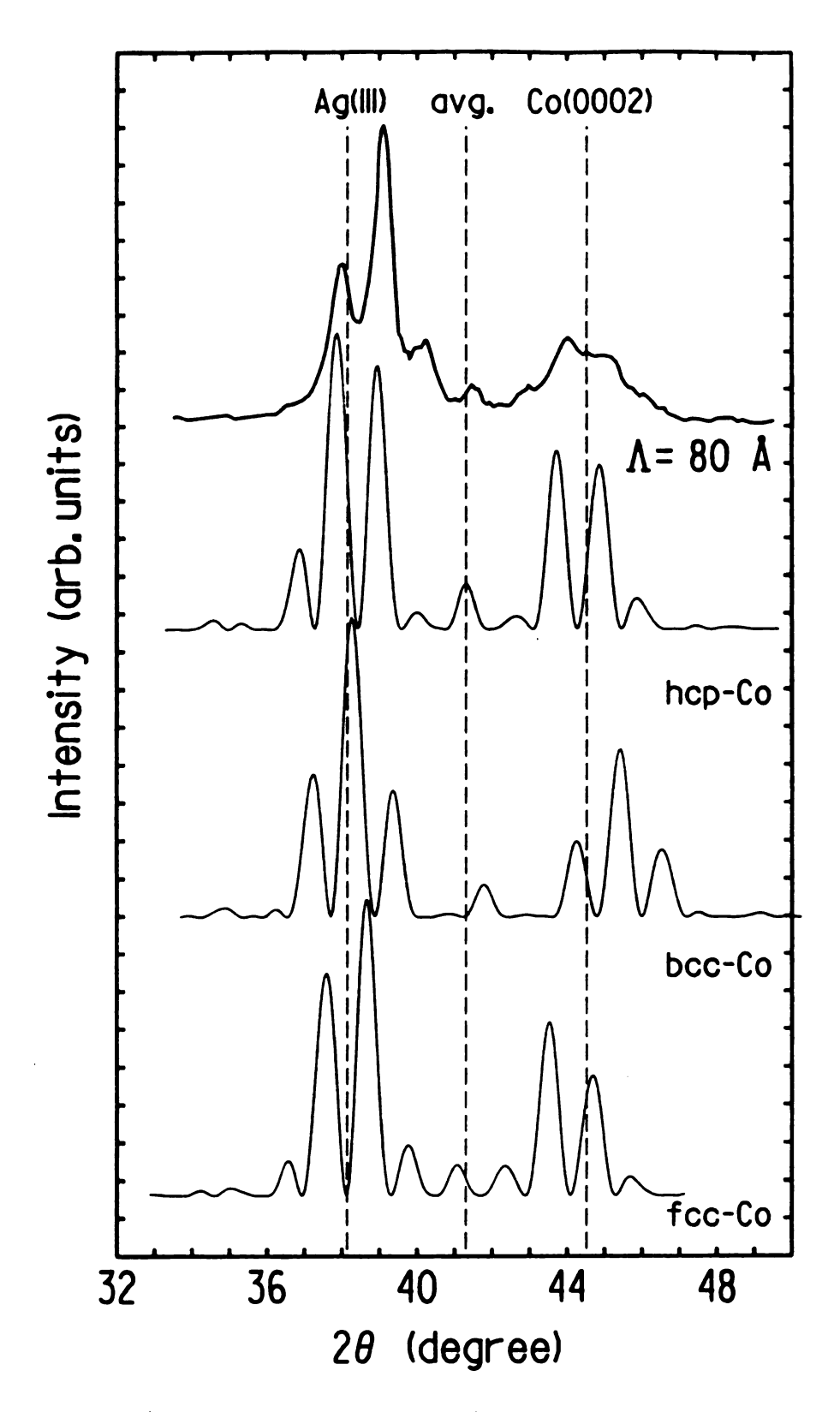


Figure 1.14  $\theta$ -20 spectra for  $\Lambda$ = 80 Å: Experimental and step model.

39

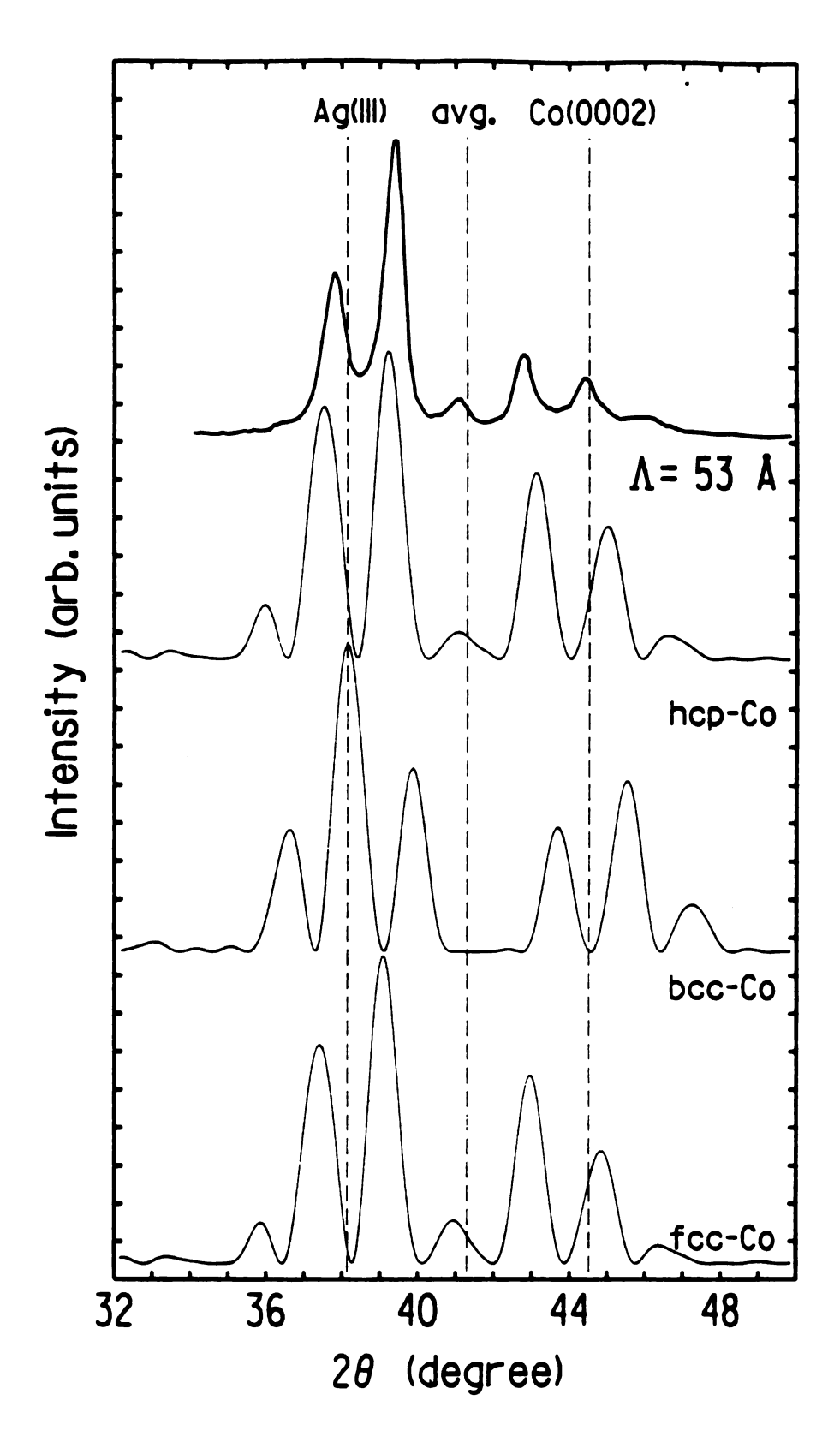


Figure 1.15  $\theta$ -20 spectra for  $\Lambda$ = 53 Å: Experimental and step model.

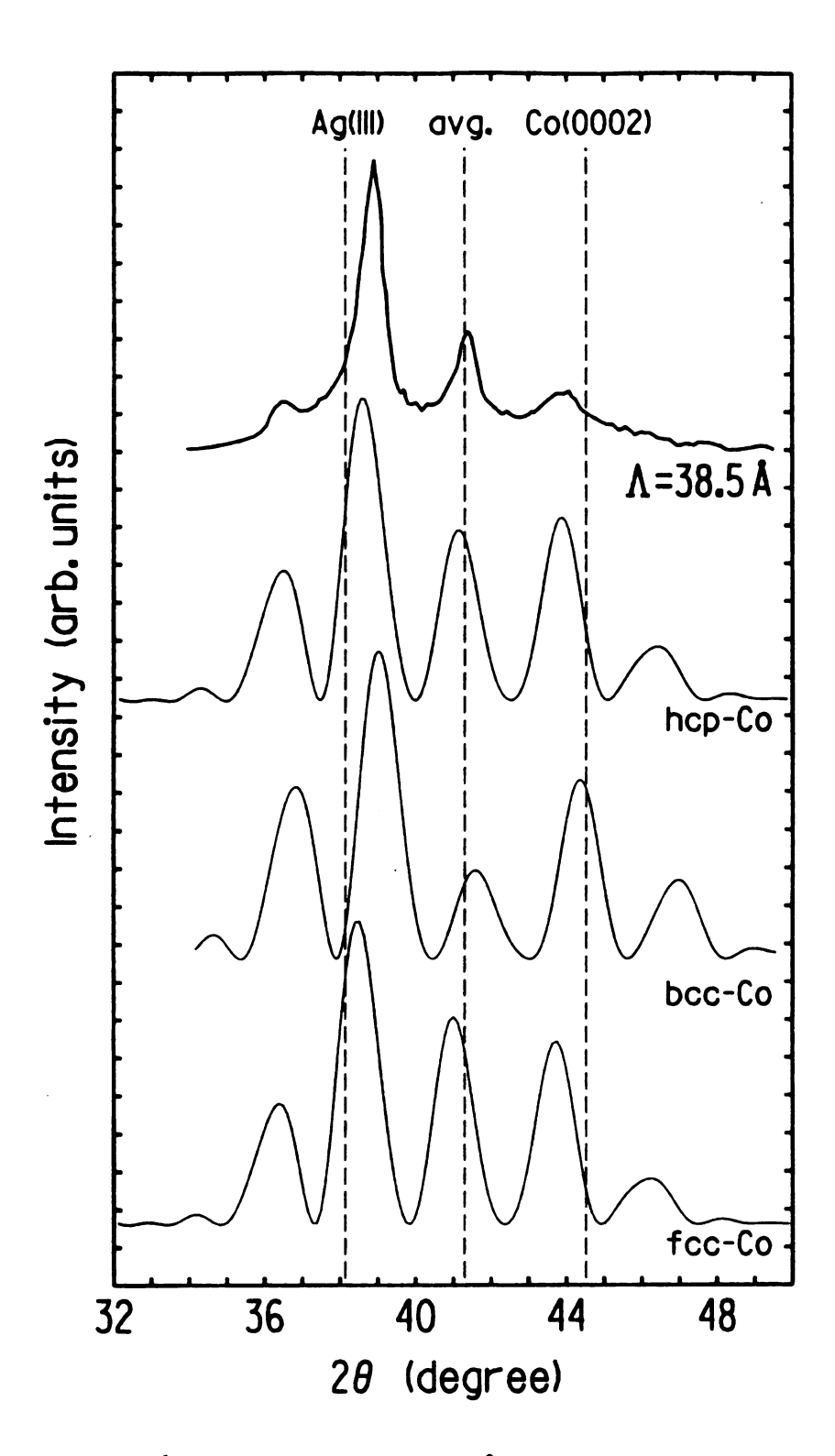


Figure 1.16  $\theta$ -20 spectra for  $\Lambda$ =38.5Å: Experimental and step model.

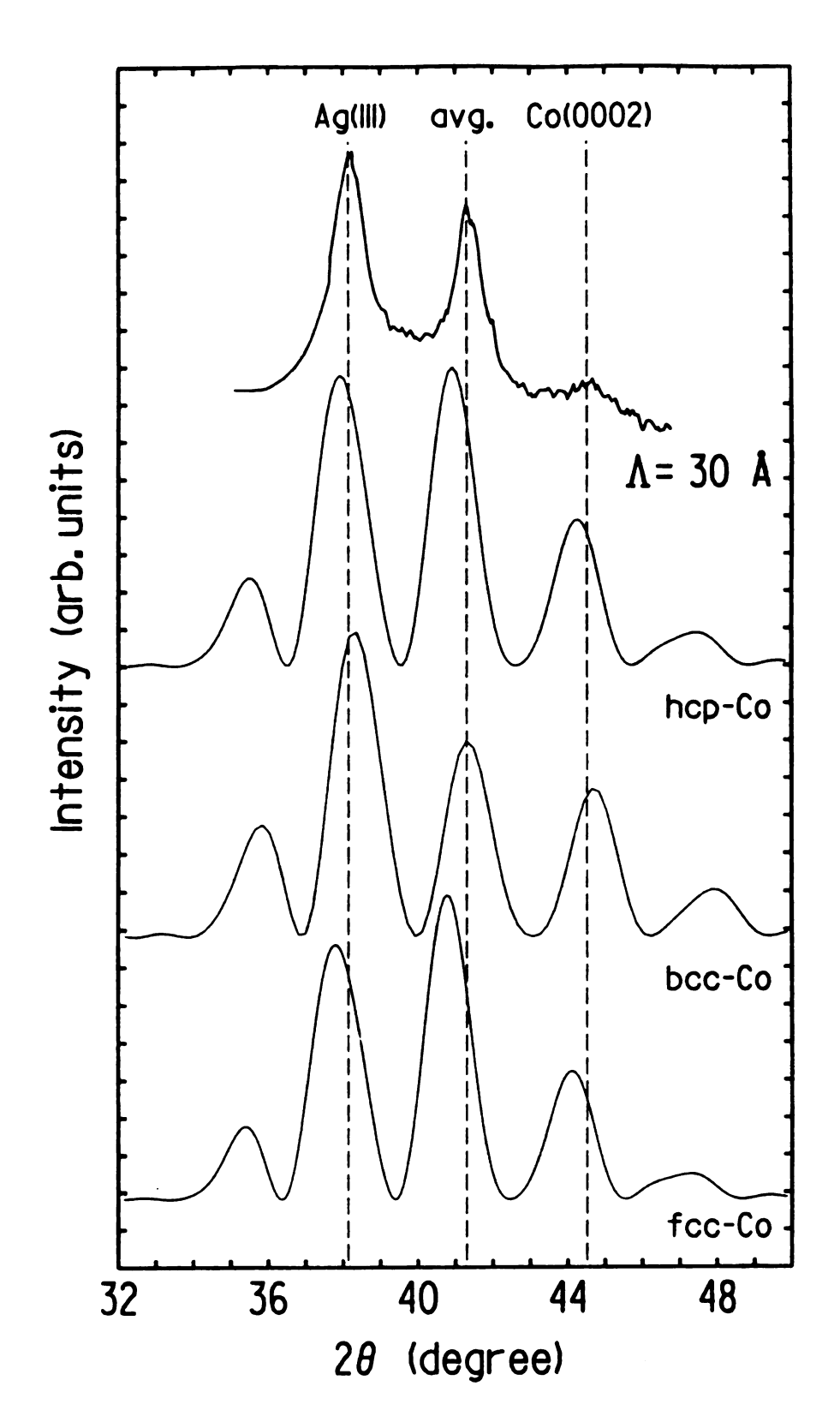


Figure 1.17  $\theta$ -20 spectra for  $\Lambda$ = 30 Å: Experimental and step model.

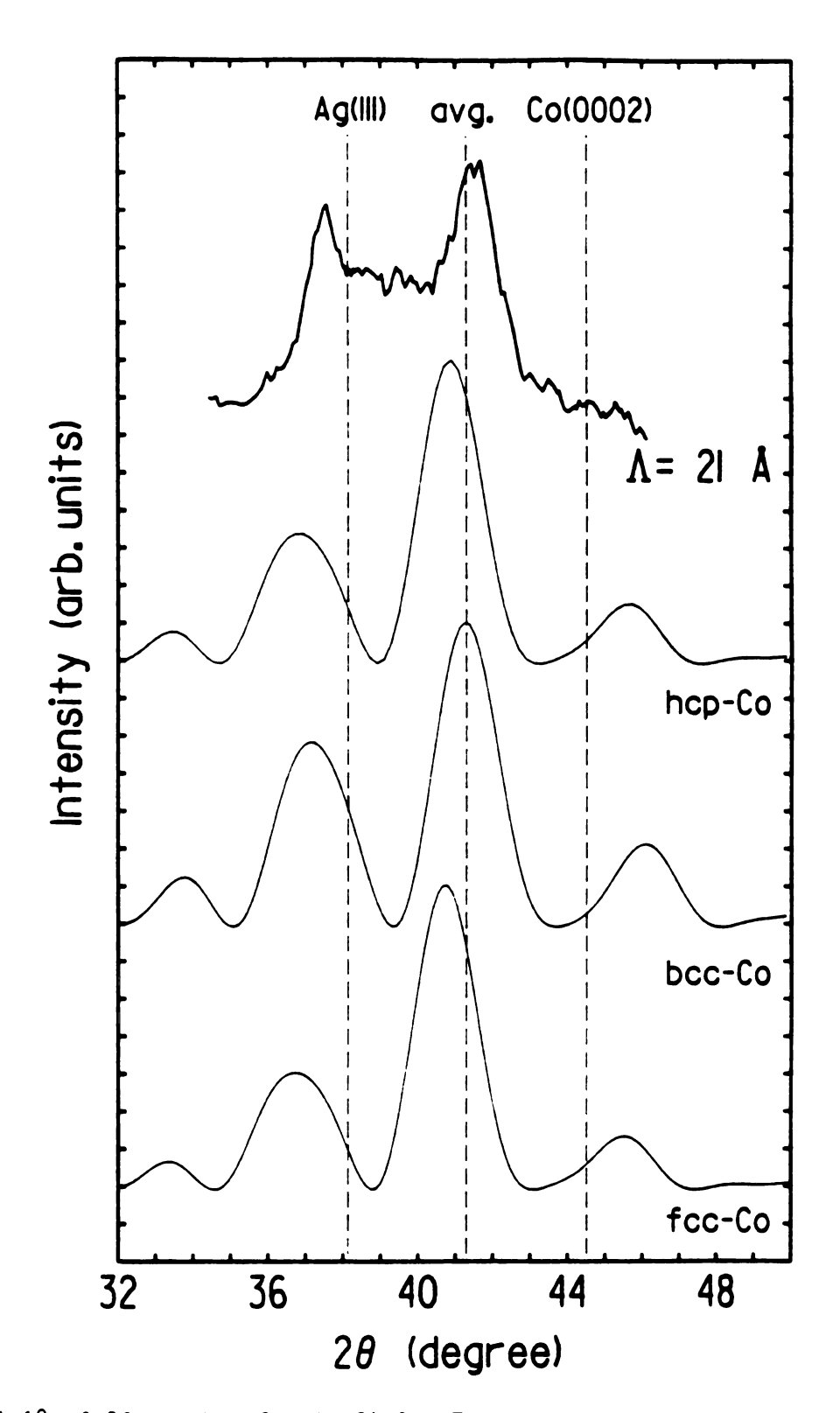


Figure 1.18  $\theta$ -2 $\theta$  spectra for  $\Lambda$ = 21 Å: Experimental and step model.

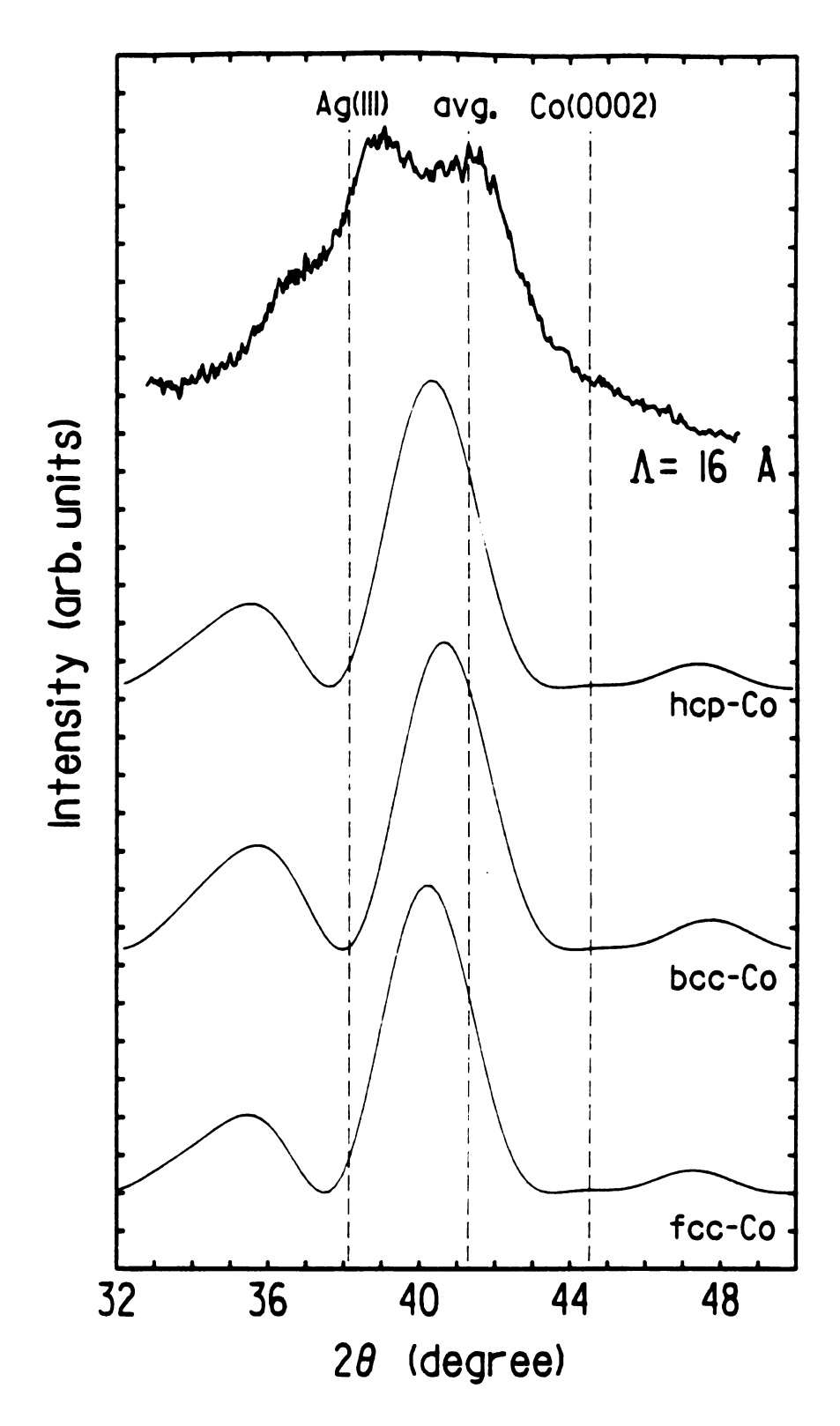


Figure 1.19  $\theta$ -20 spectra for  $\Lambda$ = 16 A: Experimental and step model.

For all of the simulated spectra shown, the number of periods N was taken to be 2. Clearly some of the simulated spectra have peak widths greater than the corresponding experimental spectra indicating in these cases that the coherence length in the sample is greater than  $2\Lambda$ . The coherence length calculated from the experimental spectra, using equation (1.3), varies smoothly from ~100Å to ~200Å as  $\Lambda$  varies from 21Å to 160Å.

In comparing experimental data to the theoretical curves one must remember that the experimental spectra may be shifted by up to 0.5° (due to backlash in the mechanism) and the theoretical curves may be shifted toward the Ag side (as explained above). The best way to make comparisons is to compare peaks by order rather than by angle.

For  $\Lambda \geq 38.5 \text{Å}$  the bcc-Co simulations give very poor fits to the experimental data. The shapes of the bcc-Co spectra in the region  $\Lambda \geq 80 \text{Å}$  sometimes look deceptively similar to the experimental spectra but if one carefully compares the satellite peaks order by order one finds that the peaks predicted by the bcc-Co model cannot be reconciled with experiment. The calculated spectra for the three model structures become increasingly similar with decreasing  $\Lambda$ . For  $\Lambda < 38.5 \text{Å}$  the calculated spectra are so similar that it is impossible to eliminate any of the three structures.

In the region  $38.5 \text{\AA} \le \Lambda \le 80 \text{\AA}$  the fcc-Co calculations fit the experimental spectra slightly better than the hcp-Co calculations. But for  $\Lambda > 80 \text{\AA}$  the hcp-Co fits slightly better than the fcc-Co.

Table 1.3 summarizes the results of the comparisons. These results should not be taken as proof of particular Co structures in the Ag-Co

Table 1.3 Summary of step model results

	(1=best	(1=best fit, 3=worst)			
Λ (Å)	hep	fcc	bec		
157	1	2	3		
1 14	1	2	3		
80	2	1	3		
53	2	1	3		
38.5	2	1	3		
30	?	?	?		
21	?	?	?		
16	?	?	?		

LMS. They should be used only as indicators, pointing the way to further studies.

Figure 1.20 shows the experimental spectrum for a nominal  $\Lambda=5\text{\AA}$  sample, in the heavy line, and the calculated spectrum in the light line. The calculated spectrum has a large average lattice peak (slightly shifted to the left since the model structure is somewhat Agrich) and another satellite peak that should be observable at  $20\approx35^{\circ}$ . The experimental spectrum shows a bulk Ag peak, shifted to the right, and a bulk Co peak, slightly shifted to the left. This sample is not layered.

X-ray measurements also show that there is a large difference in the structure of samples made on cool ( $T\sim30\,^{\circ}$ C) and hot ( $T\sim80\,^{\circ}$ C) substrates. Samples with a nominal period of  $80\,^{\circ}$  made on hot substrates show only a few broad remnants of satellite peaks.

The rocking curves for all of the LMS samples have a full width at half maximum of ~12°. This result shows that there is a distribution of orientations of crystallites with the majority of them within  $\pm 6$ ° of the preferred direction.

# I. Determining the Sample Geometry

In order to calculate resistivity from a measured resistance one must know the geometry of the sample. For LMS samples we have two methods of determining the actual film thickness: X-ray diffraction and a Dektak IIA surface profiler [SLN].

To determine the film thickness from the X-ray diffraction data one must first calculate  $\Lambda$  from the spacing of the satellite peaks, then the

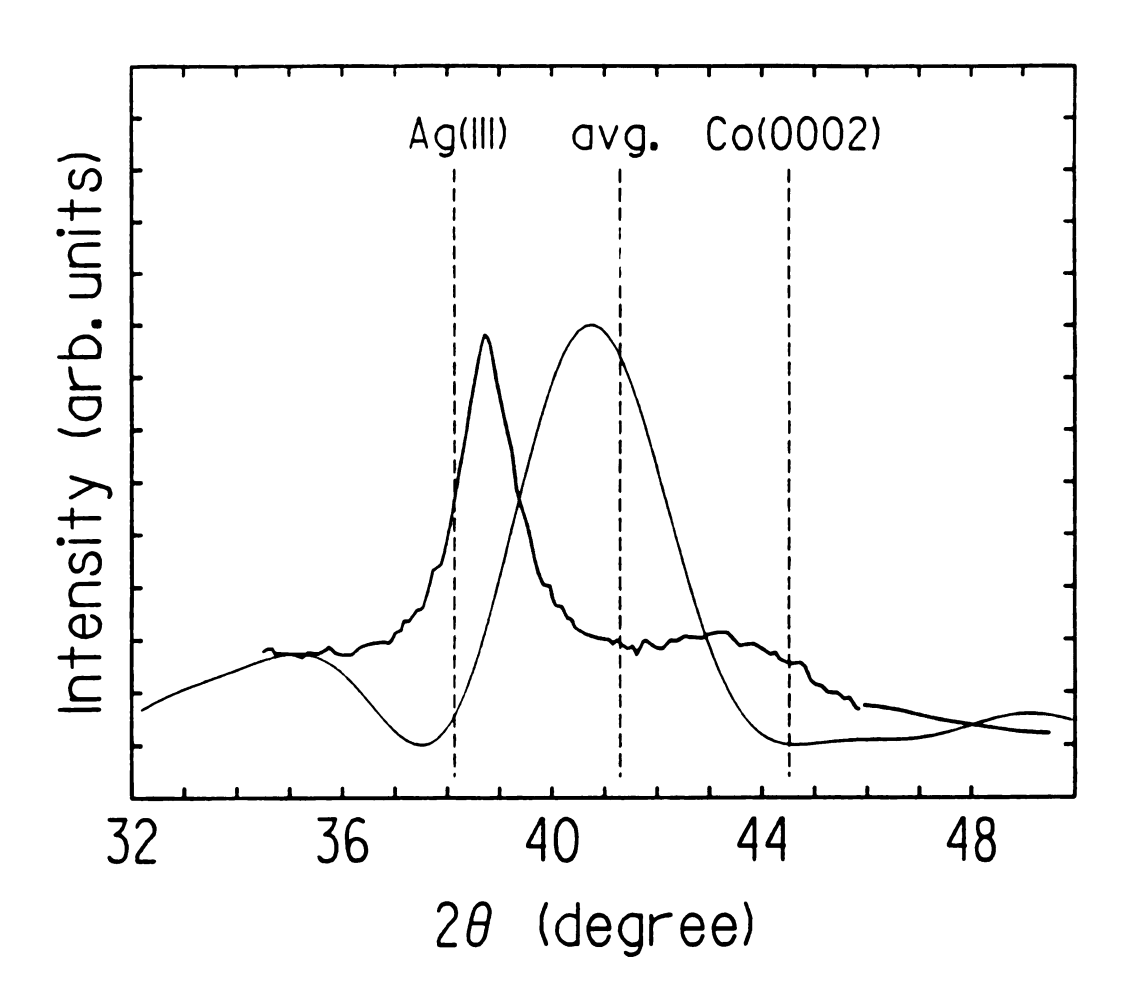


Figure 1.20  $\theta$ -20 spectra for "A= 5Å": Experimental and step model.

thickness t is just the product of the number of periods in the sample and the period  $\Lambda$ . This method works well for samples with many well separated satellite peaks. For samples with only two satellites or with satellites that are to close together to be accurately distinguished the Dektak method is more accurate.

The Dektak surface profiler measures the profile of thin films by passing a stylus over the film and measuring the deflection of the stylus electromechanically. The largest source of error in these measurements is that associated with substrate imperfections such as curvature and slope discontinuities. Since the edges of the films are not perfectly sharp the height of a step must be measured over some horizontal displacement. If the substrate curves or has a discontinuity in the transition region it becomes difficult to determine the film thickness. This problem leads to an uncertainty in the thickness of approximately ±200Å.

The two most valuable features of the Dektak are its ability to measure the thickness of pure films and other films for which the X-ray method cannot be used and its ability to measure the horizontal extent (width) of the films. The latter feature is necessary to determine the geometry of the perpendicular transport samples. Since the widths of the Nb strips determine the area of the effective sample, and the widths can vary depending on how well the substrate presses down on the mask, it is very important to measure the width of every strip. The method we have used to measure the width of a strip is to find the points where the strip is 100Å thick and measure the distance between them using the Dektak. The 100Å criterion is somewhat arbitrary but the idea is to consider all of the Nb that is superconducting as part of the width.

The full thickness of the Nb strips is ~5000Å. An example of a Dektak profile of a strip is shown in Figure 1.21.

The resistivity  $\boldsymbol{\rho}$  is calculated from the measured resistance R using the relation

$$\rho = R \frac{A}{1} \tag{1.15}$$

where the A is the cross-sectional area and 1 is the length of the sample. For perpendicular transport samples A is the product of the widths of the strips and l is the thickness of the sample film. The uncertainty in the geometrical factor  $\frac{A}{1}$  is typically ±10% for the perpendicular transport samples if the strip widths and the sample thickness are measured with the Dektak. For some samples with particularly irregular substrates or fuzzy Nb strips the uncertainty may be larger. For the parallel transport the geometrical uncertainty is much smaller. The area for a parallel sample is the product of the film thickness and its width and the length is just the distance between the voltage leads (5.3mm). The relative uncertainty of the length is very small and the widths are more constant than the widths of the Nb strips since a fixed mask is used to produce the shape. Therefore most of the error in the parallel resistivity comes from the thickness determination. For LMS samples with As which make it possible to use the X-ray method, the uncertainty is  $\sim 3\%$ , for other samples it is  $\sim 5\%$ .

A comparison of the nominal production  $\Lambda s$ , the Dektak values and those determined from X-ray diffraction for the samples made in run 38 is given in Table 1.4. We find reasonable agreement between the different values of  $\Lambda$ .

Table 1.4 Comparison of nominal and measured sample parameters

sample		Λ (Å)	
	nominal	Dektak	X-ray
3809	14	16	19±3
3808	20	21	22
3814	20	21	23
3815	28	30	30
3807	36	38	38.5
3805	50	-	52
3813	80	78	80±3
3810	120	120	114±5
3811	160	157	165±10

\_\_\_\_

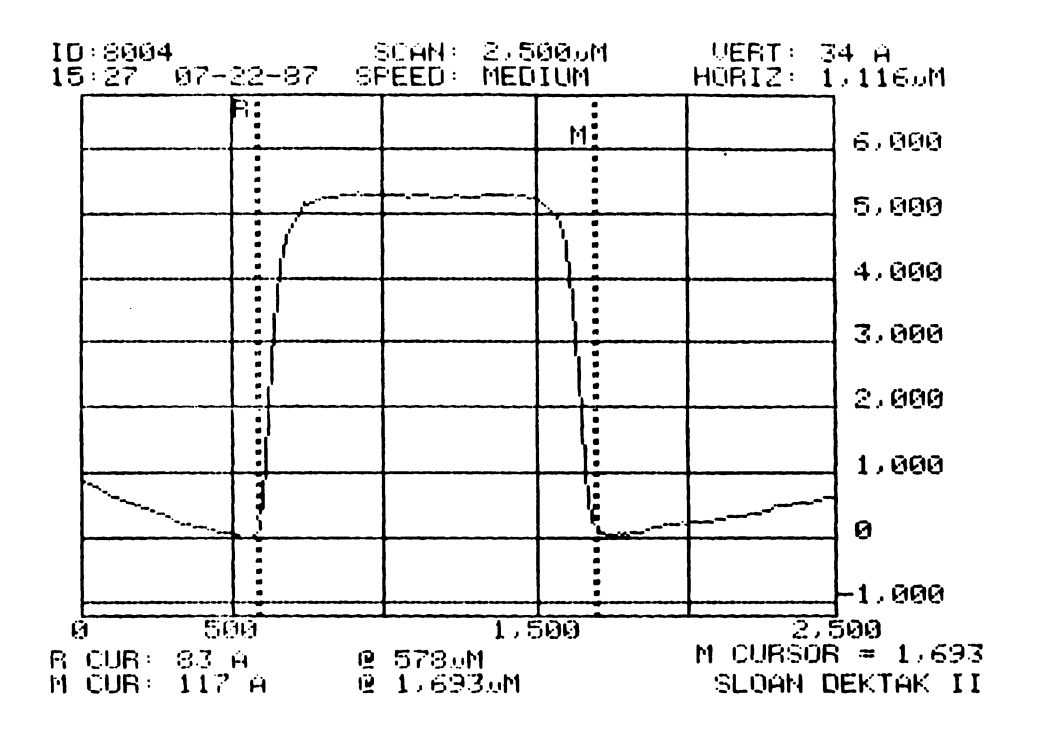


Figure 1.21 Dektak profile of a Nb strip.

#### CHAPTER 2

### RESISTIVITY PARALLEL AND PERPENDICULAR TO THE LAYERS

### A. PARALLEL RESISTIVITY

### 1. Introduction

Figure 2.1 shows  $\rho_{par}$  measured at room temperature as a function of  $\Lambda$  for a variety of LMS measured by several workers [Gu86, Kh83, We82, Ca83, Ca85]. Clearly  $\rho_{par}$  for the Ag-Co system is lower than that reported for any other LMS. Associated with this low resistivity there must be a relatively long electronic mean free path  $\ell$  in one or both materials forming the layers. A specific model of electron transport in a LMS is needed to find the  $\ell$ s for the Ag and Co layers independently, but, to get an idea of their magnitude we can calculate an effective mean free path  $\ell_{eff}$  which is just  $\ell$  calculated as if the material were homogeneous. For Ag-Co,  $\ell_{eff}$  can be easily estimated using a free electron theory since the free electron Fermi velocities  $\mathbf{v}_F$  of these two metals are nearly the same. In free electrons n and the relaxation time  $\tau$  by the relationship [As76]

$$\rho = \frac{m}{ne^2\tau} \tag{2.1}$$

where e and m are the electronic charge and mass respectively. The expression for n in terms of the Fermi wave vector  $\mathbf{k}_{\mathrm{F}}$  is

$$n = \frac{1}{3\pi^2} k_F^3 \tag{2.2}$$

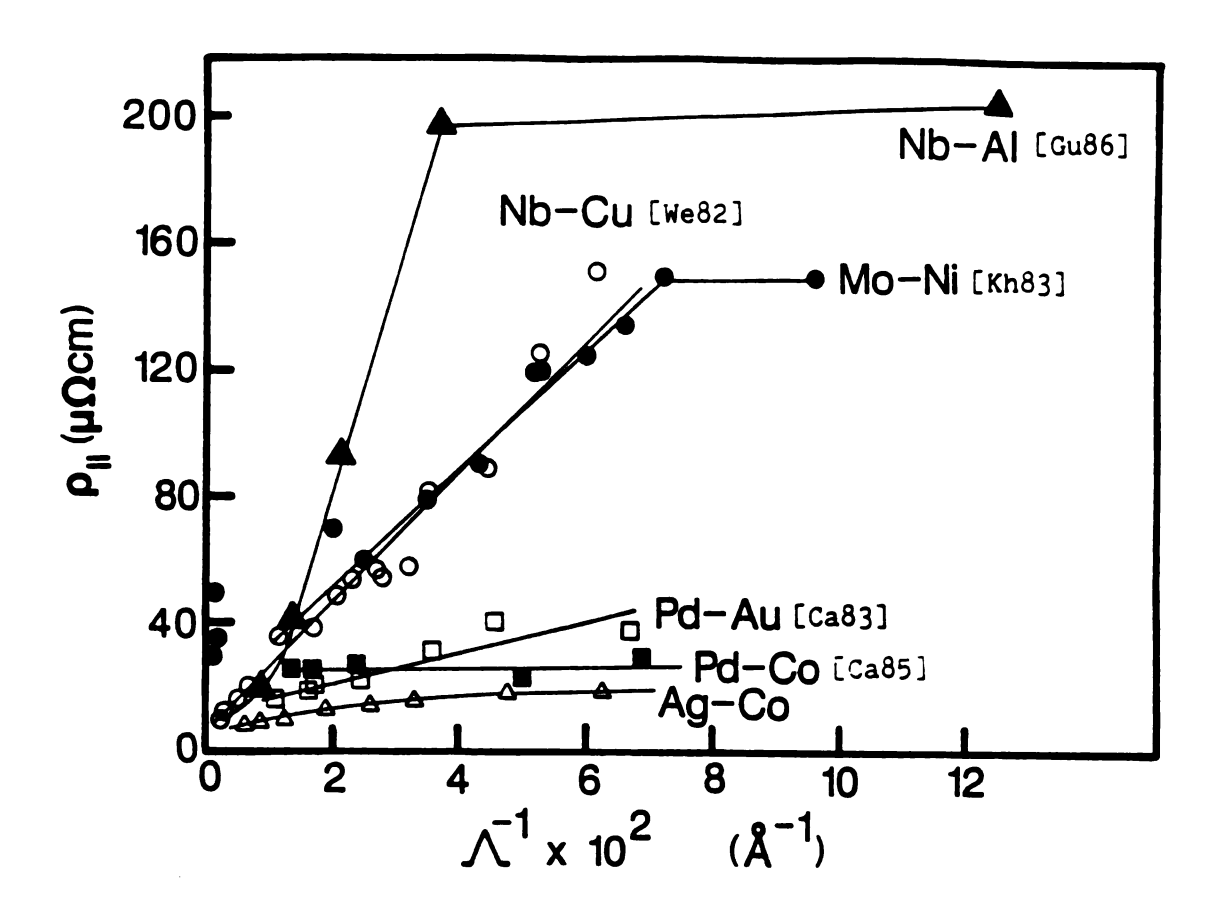


Figure 2.1  $\rho_{par}$  at room temperature for various LMS.

where 
$$k_F = \frac{2\pi m v_F}{h}$$
.

Combining (2.1) and (2.2), and recalling that  $\ell$  =  $v_F^*\tau,$  we can write  $\ell$  in terms of  $v_F$  and  $\rho$  as

$$\ell = \frac{3}{8\pi} \frac{h^3}{(mv_E e)^2} \frac{1}{\rho}$$
 (2.3)

where h is Plank's constant. For both Ag and Co  $v_F \approx 1.4 \times 10^8$  cm/s [Mo58] so that equation (2.3) can be rewritten as

$$\rho l_{eff} = 8.3 \times 10^{-12} \Omega cm^2$$
. (2.4)

Equation (2.4) is in agreement with the experimental values for Ag published in Landolt-Bornstein [Ba85] but there is some disagreement about the correct value of pl for Co. The justification for applying equation (2.4) to Co is addressed in section 2c - Determining the Bulk Parameters.

The result of this simple calculation, shown in Figure 2.2, is that  $\ell_{\rm eff}$  is greater than an individual layer thickness for  $\Lambda \le 160 \mbox{\AA}$  over the temperature range of 4.2 to 295K. Clearly a significant fraction of the electrons encountering an interface must be either reflected or transmitted.

# 2. Parallel Transport Theory

Two models were used to fit the  $\rho_{par}$  vs.  $\Lambda$  data. The first assumes transmission and diffuse scattering at the interfaces whereas the second assumes reflection and diffuse scattering. Both models are free

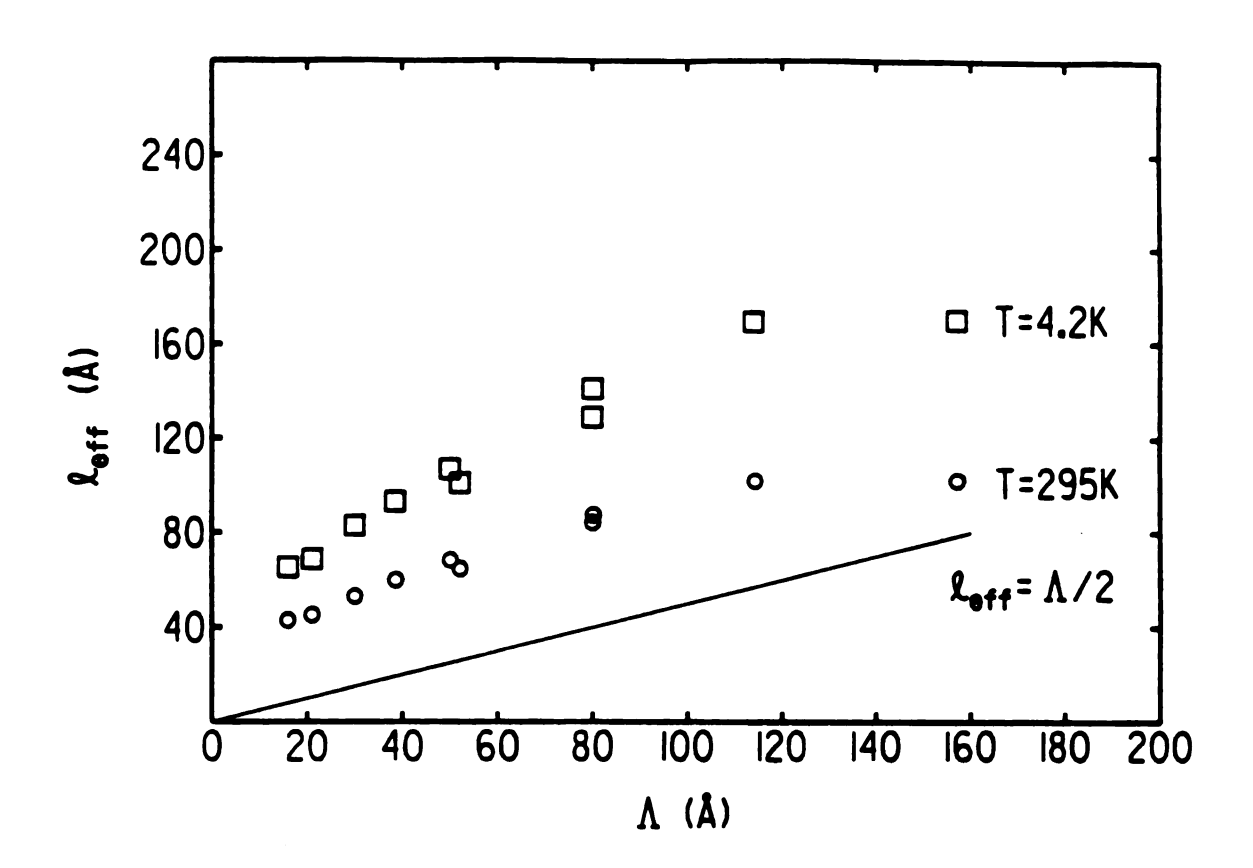


Figure 2.2  $\ell_{\mbox{eff}}$  versus A for Run 38 Ag-Co LMS.

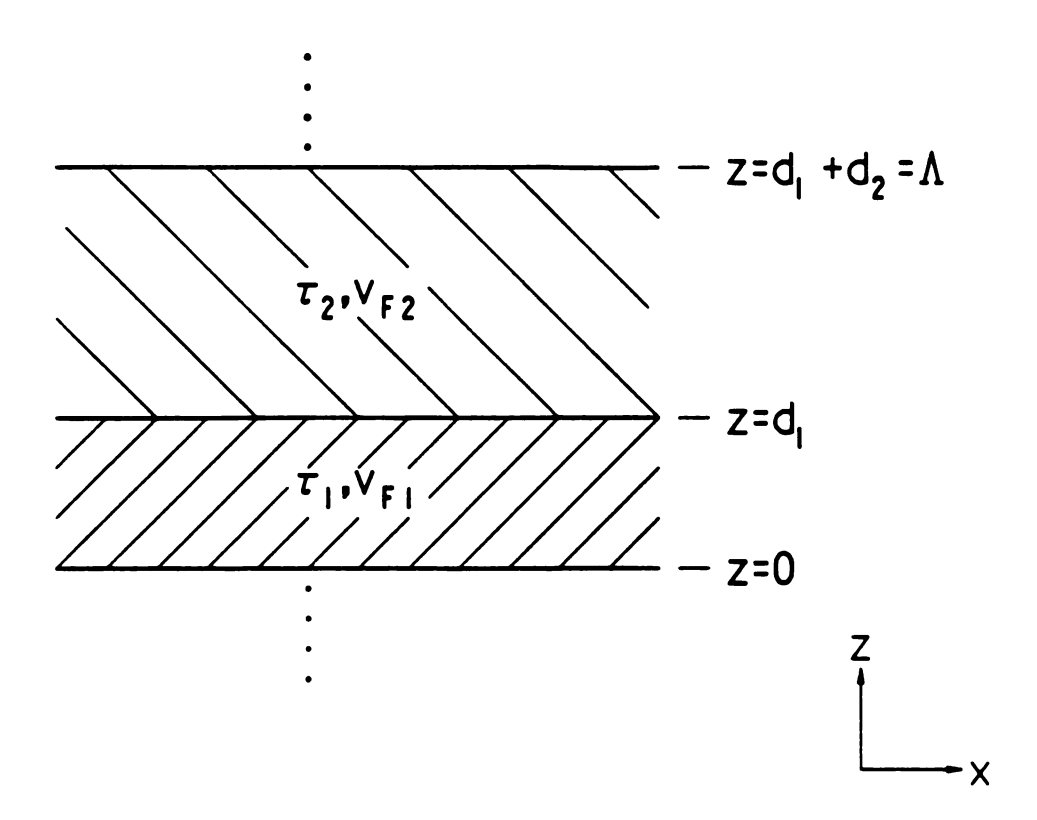


Figure 2.3 Fuchs model geometry of a LMS.

electron models based on the Fuchs-Sondheimer treatment of thin film conduction [Fu38, So52]. The original treatment is modified to take into account the layered geometry shown in Figure 2.3. The materials are characterized by their Fermi velocities and relaxation times;  $\mathbf{v}_{F1}$ ,  $\tau_1$  and  $\mathbf{v}_{F2}$ ,  $\tau_2$  for materials 1 and 2 respectively. The free electron approximation is better for Ag than for Co since the latter has a more complicated band structure which is being ignored in this treatment.

### a. Model 1 - transmission

Model 1 assumes that electrons encountering an interface are either diffusely scattered or else transmitted without deflection. The probability of transmission t is a free parameter. In this model the layers are not independent and cannot be treated as resistors in parallel. However,  $\rho_{par}$  can be found following the method used by Sondheimer for the case of a single thin film [So52].

We begin by writing the electronic distribution function f as

$$f = f_0 + g(\vec{v}, z) \tag{2.5}$$

where g is a function of the space variable z but not x or y (see Figure 2.3),  $\dot{v}$  is the velocity and  $f_o$  is the equilibrium distribution function (Fermi function). The Boltzmann transport equation in the relaxation time approximation then reduces to

$$\frac{\partial \mathbf{g}}{\partial \mathbf{z}} + \frac{\mathbf{g}}{\mathbf{v}_{\mathbf{v}}} = \frac{\mathbf{e}\mathbf{E}}{\mathbf{m}\mathbf{v}_{\mathbf{v}}} \frac{\partial \mathbf{f}_{\mathbf{o}}}{\mathbf{v}_{\mathbf{v}}} . \tag{2.6}$$

The general solution is

$$g(\vec{v}, z) = \frac{e \tau E}{m} \frac{\partial f_o}{\partial v_x} \left\{ 1 + F(\vec{v}) \exp\left(\frac{-z}{\tau v_z}\right) \right\}, \qquad (2.7)$$

where E is the magnitude of the electric field,  $\tau$  is the relaxation time and  $F(\vec{v})$  is an arbitrary function of  $\vec{v}$ .

The function  $F(\tilde{\mathbf{v}})$  is determined by applying boundary conditions near the interfaces. The boundary conditions are a mathematical way of saying that the distribution function of electrons moving away from an interface evaluated very near the interface has two parts; the part due to diffusely scattered electrons and the part due to electrons transmitted across the interface from the other material. The appropriate boundary condition for the z=0 interface evaluated an infinitesimal distance above the interface  $(z=0^+)$  is

a. for 
$$z=0^+$$
 and  $v_2>0$ 

$$f_{01} + g_1(\vec{v}, 0^+) = (1-t)f_{01} + t\{f_{02} + g_2(\vec{v}, \Lambda^-)\}$$
 (2.8)

where the left side is by definition and the right side represents the sum of the diffusely scattered electrons from material 1 and the electrons transmitted from material 2 (with probability t). The periodicity of the structure is used to write  $\Lambda^-$  in place of  $0^-$ . Three more boundary conditions can be written for the other interfaces which make up one period of the structure.

b. for 
$$z=d_1$$
 and  $v_z<0$ 

$$f_{01} + g_1(\vec{v}, d_1^-) = (1-t)f_{01} + t\{f_{02} + g_2(\vec{v}, d_1^+)\}$$
 (2.9)

c. for 
$$z=d_1^+$$
 and  $v_z>0$ 

$$f_{02} + g_2(\vec{v}, d_1^+) = (1-t)f_{02} + t\{f_{01} + g_1(\vec{v}, d_1^-)\}$$
 (2.10)

d. for  $z=\Lambda^-$  and  $v_z<0$ 

$$f_{02} + g_2(\vec{v}, \Lambda^-) = (1-t)f_{02} + t\{f_{01} + g_1(\vec{v}, 0^+)\}.$$
 (2.11)

Applying the boundary conditions to the general solution (2.7) yields four equations which are solved to find the four unknown functions defining the distribution function for a LMS. The distribution functions are integrated to give the current density according to the relation

$$j_x = -2e(m/h)^3 \int v_x g(\bar{v}, z) d^3v.$$
 (2.12)

Working in spherical coordinates the integral over v can be done by recalling that for a degenerate electron gas

$$\int_{0}^{\infty} \Psi(\mathbf{v}) \frac{\partial \mathbf{f}_{o}}{\partial \mathbf{v}} d\mathbf{v} = -\Psi(\mathbf{v}_{\mathbf{F}}). \tag{2.13}$$

The  $\phi$  integral is trivial and the  $\theta$  integral must be done numerically. The current density is integrated over the layer of material 1 to find the conductivity

$$o_1 = o_{o_1} \{ 1 + \frac{3\ell_1}{4d_1} (I_1 + I_2) \} - to_{o_2} \frac{\tau_1 v_{F2}}{d_1} (I_3 + I_4)$$
 (2.14)

where the  $\mathbf{I}_{\alpha}$  have the form

$$I_{\alpha} = \begin{cases} \theta_{2} & \{C_{1} - C_{2} \exp(-C_{3}/\cos\theta)\} \{ 1 - \exp(-C_{4}/\cos\theta) \} \\ C_{3} \exp(-(C_{3} + C_{4})/\cos\theta) - C_{4} \end{cases} \sin \theta \cos\theta d\theta$$

(2.15)

and  $\sigma_{ei}$ ,  $\ell_i$ ,  $\tau_i$ , and  $v_{Fi}$  are the bulk conductivity, mean free path, relaxation time and Fermi velocity respectively of material i. The  $C_{\sigma}$ 

and  $\boldsymbol{\theta}_{\alpha}$  are given in Table 2.1. The integrals  $\boldsymbol{I}_{\alpha}$  must be done numerically.

Since identifying a layer as 1 or 2 is arbitrary, the expression for  $\sigma_2$  can be found simply by exchanging all subscripts referring to materials 1 and 2. Finally the resistivity of the LMS is given by

$$\rho_{\text{par}} = \frac{d_1 + d_2}{\sigma_1 d_1 + \sigma_2 d_2}.$$
 (2.16)

Equation 2.16 looks like the formula for resistivity parallel to the layers where the layers are treated as independent resistors, but it is not since the  $\sigma_i$  are not the bulk conductivities.

The bulk parameters will be determined from thick pure metal films as described below and t will be adjusted to give the best fit to the experimental data.

#### b. Model 2 - reflection

Consider the case where an electron encountering an interface has probability p of being specularly reflected and probability (1-p) of being diffusely scattered. Now the layers are decoupled and can be treated as independent resistors so that the conductivity of an LMS with equal thickness layers is related to the conductivities of the layers according to the relation

$$2\sigma_{par} = \sigma_1 + \sigma_2$$
. (equal thickness layers) (2.17)

The  $\sigma_i$  in equation (2.17) are not the bulk conductivities of the materials but the actual conductivities of the layers including the interface scattering contribution. The conductivity  $\sigma$  of a layer in

Table 2.1 Definition of parameters for model 1 integrals

	Ι,	I 2	Ι,	Ι,
C,	1	t <sup>2</sup>	1	1
C <sub>2</sub>	t <sup>2</sup>	1	1	1
С,	<sup>d</sup> 2 <sup>1</sup> 2 <sup>v</sup> F1	<sup>d</sup> <sub>2</sub> τ <sub>2</sub> ν <sub>F1</sub>	d <sub>2</sub> l <sub>2</sub>	d <sub>2</sub>
С.,	d <sub>1</sub> 2 <sub>1</sub>	$\frac{d_1}{\ell_1} \frac{d_2}{\tau_1}$	1  / <sub>F2</sub>	<sup>d</sup> <sub>1</sub> <sup>τ</sup> 1 <sup>v</sup> F2
C,	t <sup>2</sup>	1	t <sup>2</sup>	1
C.	1	t <sup>2</sup>	1	t <sup>2</sup>
Θ,	0	$\frac{\pi}{2}$	0	$\frac{\pi}{2}$
Θ₂	<u>1</u> 2	π	<del>1</del> /2	π

this model is given by the Fuchs result for a thin film of thickness d with specular reflection coefficient p [So52]

$$\frac{\sigma}{\sigma_0} = 1 - \frac{3}{2} \frac{\ell}{d} (1-p) \int_{1}^{\infty} \left( \frac{1}{x^3} - \frac{1}{x^5} \right) \frac{1 - \exp(-xd/\ell)}{1 - \exp(-xd/\ell)p} dx.$$
 (2.18)

Equation 2.18 is often approximated by simpler formulae which are valid in certain limits of  $\frac{\ell}{d}$  but in the present case we wish to perform calculations over a large range of  $\frac{\ell}{d}$  so we have no choice but to perform the integration numerically.

In this model p is a free parameter and the same bulk parameters as in model 1 are used to describe the Ag and Co.

### c. Determining the Bulk Parameters

In order to apply the models we must determine the bulk parameters  $v_F(Ag)$ ,  $\ell_{Ag}$ ,  $\tau_{Ag}$ ,  $v_F(Co)$ ,  $\ell_{Co}$  and  $\tau_{Co}$ . We again used  $v_F = 1.4 \times 10^8$  cm/s for both Ag and Co so that for both materials we have

$$\rho l = 8.3 \times 10^{-12} \Omega \text{cm}^2 \tag{2.19}$$

just as in equation (2.4). The measured resistance of a thick film of pure metal, produced under the same conditions used to produce the LMS, is used to determine  $\ell$  and  $\tau$  for that metal. If the film thickness is comparable to  $\ell$ , then the resistivity of the film will not be the bulk resistivity but will have a "size effect" contribution due to scattering from the film surfaces. An approximate form of the resistivity  $\rho$  of a film made of metal with bulk resistivity  $\rho_0$  as a function of its thickness d and coefficient of specular reflection  $\rho$  is

$$\frac{\rho}{\rho_0} \approx 1 + (1-p)\frac{3}{8}\frac{\ell}{d}$$
 (2.20)

in the limit of  $\frac{\ell}{d}$  << 1. Equation (2.20) was first derived by Fuchs [Fu38] in 1938. Although this relation is strictly valid only in the large d limit, in fact it yields a value of  $\frac{\rho}{\rho_0}$  at  $\ell$ =d that differs from the exact value by only 6% and the comparison becomes steadily more favorable with increasing d [So52]. Equation (2.20) was used to calculate  $\rho_0$  from the measured resistivities of the thick films of Ag using p=0. The assumption that p=0 is justified since published values of  $\rho\ell$  determined from the size effect using p=0 are in agreement with equation (2.4) and with each other [Ba85]. If a different value of p is used then a different  $\rho\ell$  would be needed. It was not necessary to correct the Co resistivity for size effects since  $\ell$ /d=0.02 for a 5000Å Co film at 4.2K.

As was mentioned earlier, there is some disagreement about the value of pl for Co. Equations (2.4) and (2.19) are calculated from the value of  $v_F$  given in [Mo58]. The pl value for Co given in Landolt-Bornstein, 460 X  $10^{-12}~\Omega {\rm cm}^2$ , is from the work of Pal et al. [Pa76] on evaporated films. This value seems unreasonable and, in addition, the resistivities of their films are more than an order of magnitude higher than ours. As a check, we used our resistivity data from pure Co films with thicknesses of 500Å and 5000Å to calculate  $\rho_o l$  for Co using equation (2.20) with p=0. Since we did not perform a complete study we were only able to extract an upper limit of  $\rho_o l \sim 20~\mathrm{X}~10^{-12}~\Omega {\rm cm}^2$ . Although our experiment did not determine  $\rho_o l$  we believe it shows that

the [Pa76] value is in error. As a result, we used the older data given in [Mo58].

#### 3. Experiment

Wires were connected to the films using In solder or silver paste.

Measurements were made at 4.2, 77, and 295K using the apparatus shown in

Figure 2.4. The current is reversed to cancel thermal emfs.

Most of the  $\rho_{par}$  data is from samples made in production run 38. In this run we produced samples with a variety of As as well as films of pure Ag and pure Co. The pure films were used to determine the bulk parameters using the procedure described above and the results are shown in Table 2.2. Measurements made on layered samples produced in other runs agreed with the measurements made on the run 38 samples. Table 2.3 shows measured resistivities for samples produced in run 38. For all LMS samples discussed here the layer thicknesses are nominally equal.

The measured  $\rho_{par}$  for samples from run 38 are shown in Figures 2.5 - 2.7 together with the theoretical fits from the two models. Note that the X-ray data, shown in chapter 1, indicates that the  $\Lambda$ =16 Å sample does not have continuous layers. For that reason it was not considered in the fitting.

Model 1 fits the data well with t varying from 0.55 to 0.63 as T varies from 295 K to 4.2 K. Model 2 fits the data only slightly worse than model 1 with p varying from 0.45 to 0.50. The fits are sufficiently close so that, on the basis of these fits alone, we cannot rule out the possibility that reflection plays a significant role in the conduction process. We conclude that approximately 1/2 of the electrons

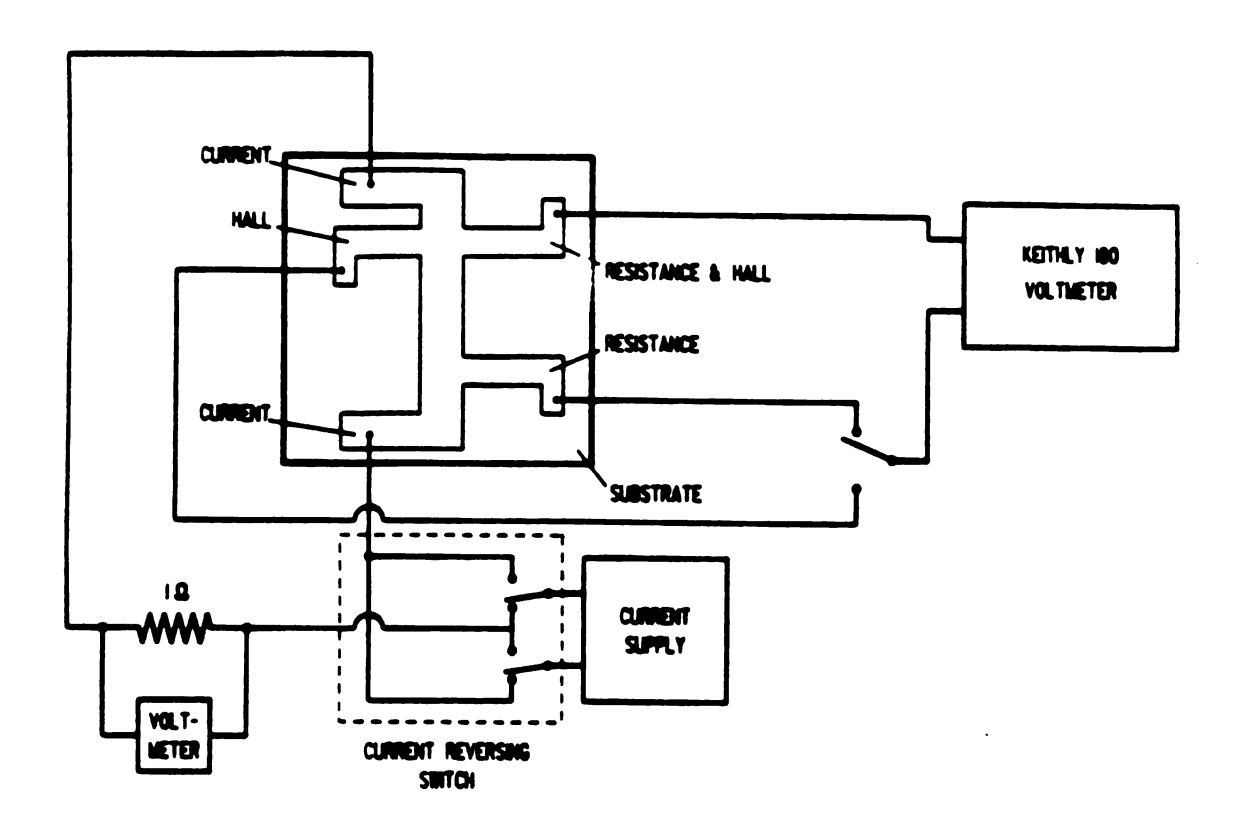


Figure 2.4 Apparatus used for  $\rho_{\mbox{\scriptsize par}}$  and Hall measurements.

Table 2.2 Free electron parameters for bulk Ag and Co

		T=295K	Т=77К	T=4.2K
OAg	(μΩcm)-1	0.454	1.01	1.29
<sup>l</sup> Ag	(Å)	379	840	1070
<sup>τ</sup> Ag	(10 <sup>-15</sup> s)	27.1	60.2	72.3
°Co	(μΩcm) <sup>-1</sup>	0.0762	0.109	0.118
<sup>l</sup> Co	(Å)	55.9	90.7	98.5
<sup>†</sup> Co	(10 <sup>-15</sup> s)	3.99	6.48	7.04

Table 2.3 Run 38 sample summary

sample	Λ (Å)	N	ρ <sub>par</sub> (μΩcm)		
			T=295K	T=77K	T=4.2K
3809	16	360	19.1	13.9	12.7
3808	21	252	18.3	13.0	12.1
3815	30	180	15.7	10.8	10.0
3805	52	250	12.9	8.88	8.28
3812	50	101	12.2	8.20	7.82
3806	. 80	63	9.96	6.89	6.47
3813	78	125	9.57	6.37	5.88
3810	114	42	8.16	5.30	4.90
3811	157	32	8.14	5.39	4.89

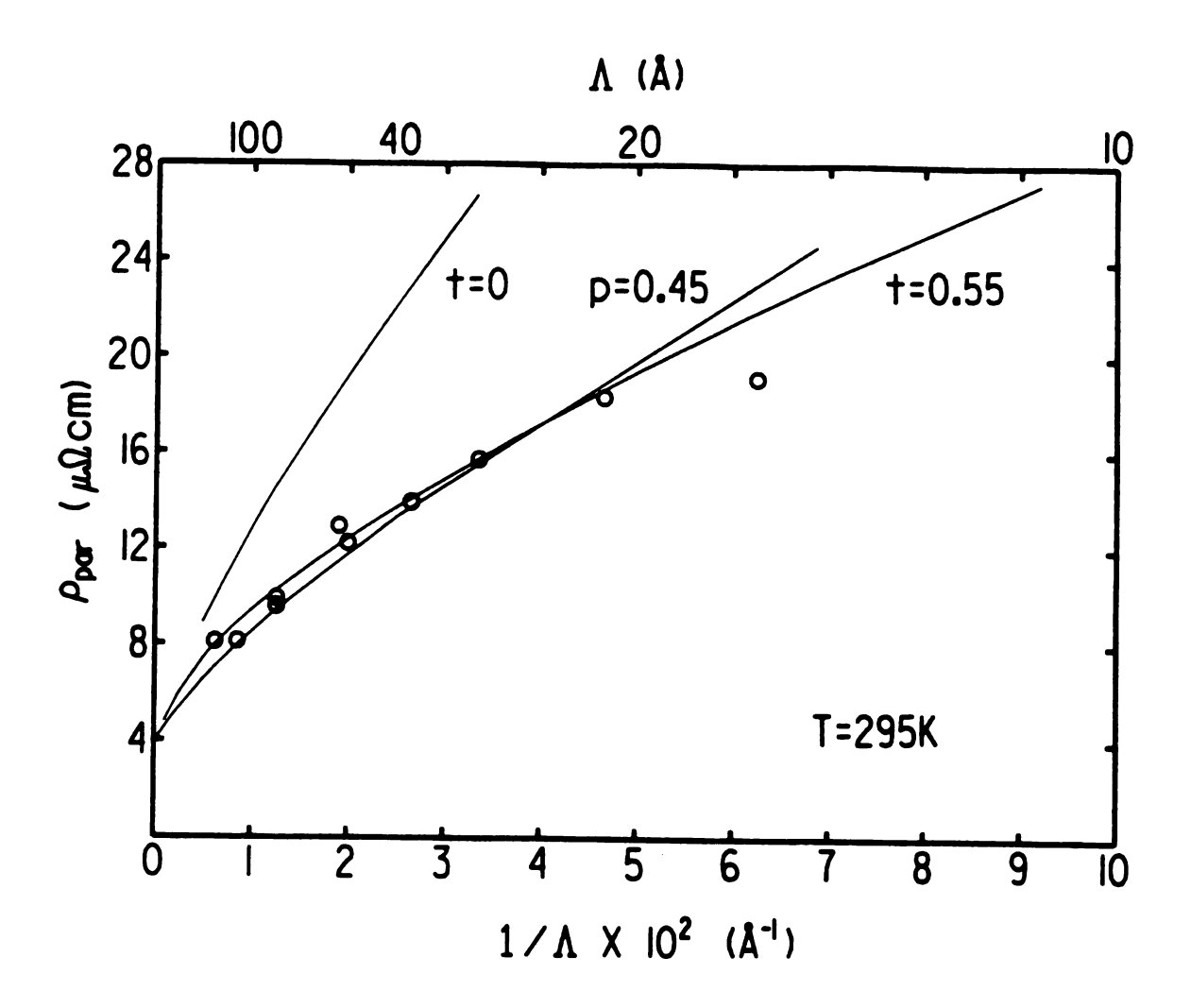


Figure 2.5  $\rho_{\mbox{\scriptsize par}}$  versus 1/A at room temperature.

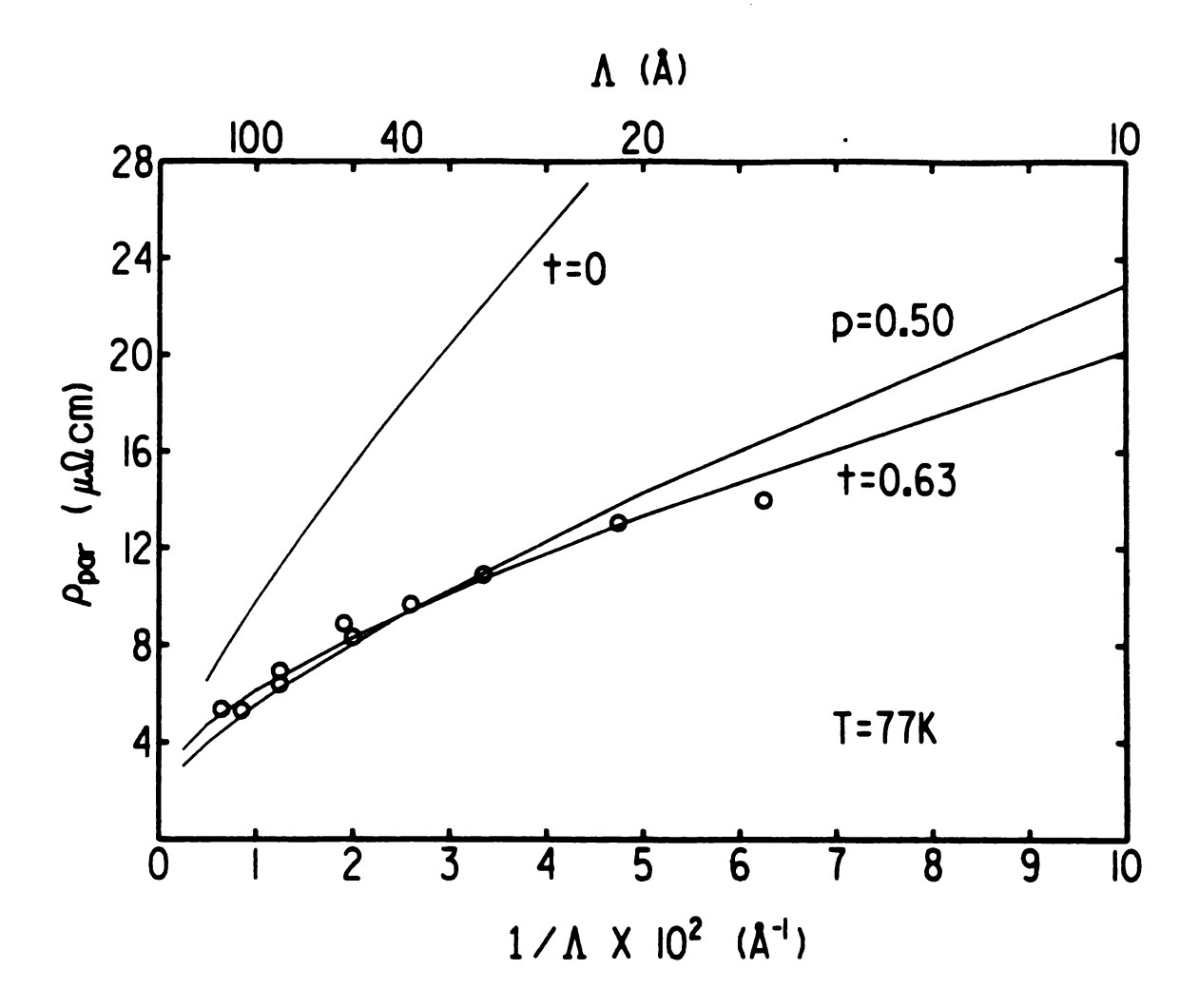


Figure 2.6  $\rho_{\mbox{\scriptsize par}}$  versus 1/A at liquid nitrogen temperature.

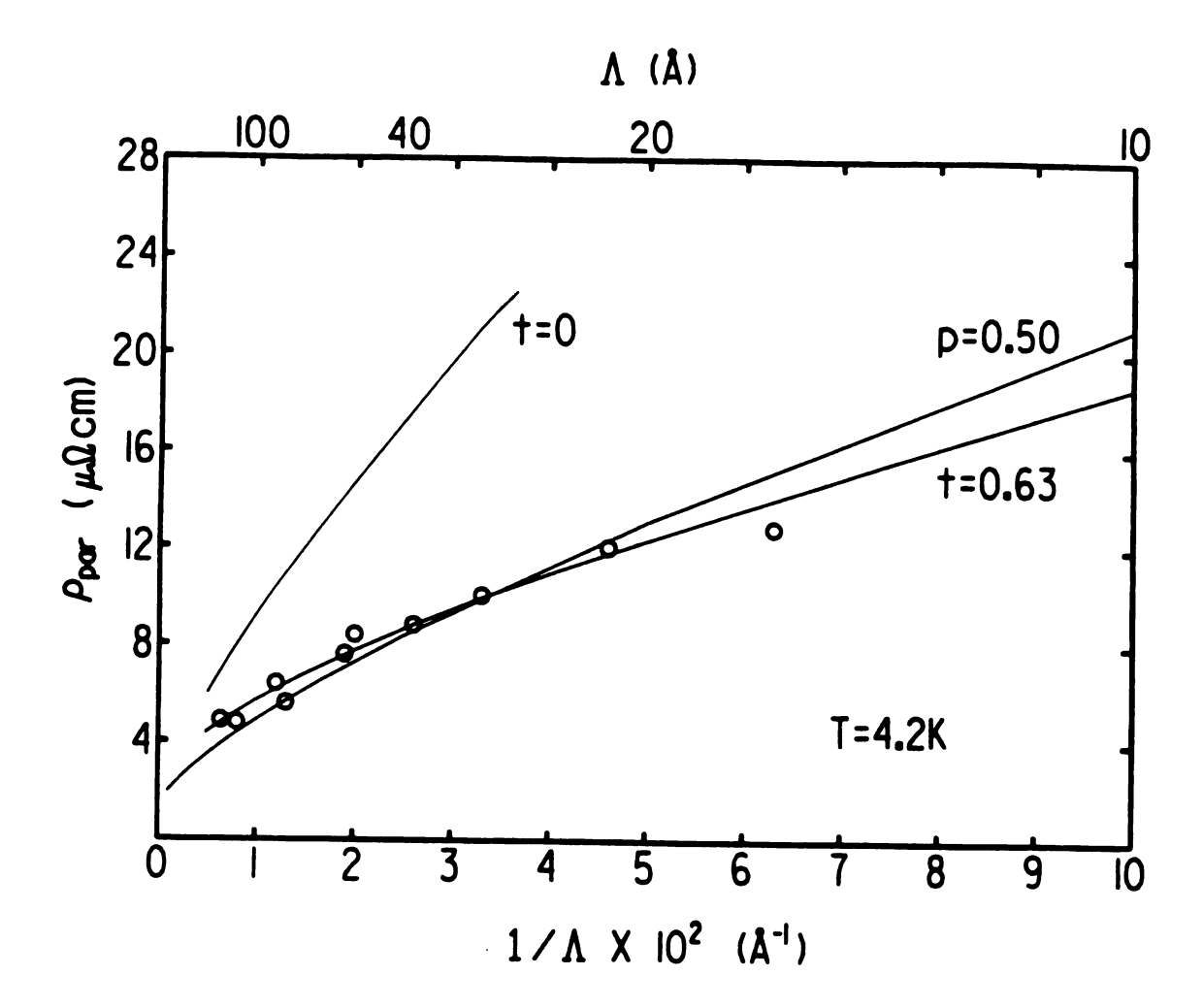


Figure 2.7  $~\rho_{par}~versus$  1/Å at liquid helium temperature.

striking an interface are diffusely scattered while the remainder undergo some type of specular scattering.

#### B. PERPENDICULAR RESISTIVITY

## 1. Free-electron Perpendicular Transport Theory

Consider a free-electron model of conduction with specular and diffuse scattering at interfaces as before. In the case of electron transport perpendicular to the layers of a LMS the effect of transmission at the interfaces is to decrease the resistivity, just as in the parallel case, but, unlike the parallel case, the effect of reflection is to increase the resistivity. To understand the effect of reflection it it useful to think of the simple case in which an electron striking an interface has probability p of being specularly reflected and probability (1-p) of being diffusely scattered. When the electric field is parallel to the layers, the momentum gained by an electron in the direction of the field is not lost when the electron is reflected. When the electric field is perpendicular to the interfaces the component of momentum parallel to the field is reversed upon reflection, causing an increase in the resistivity over what it would be if there were complete diffuse scattering at the interfaces.

There are, in the literature, theories which treat electron transport in a metal with a periodic array of scattering barriers [Sz86, Ma70]. Although these theories were intended to describe transport in polycrystalline metals we have adapted one of them, by Szczyrbowski and Schmalzbauer, in an effort to describe perpendicular transport in a LMS.

Szczyrbowski and Schmalzbauer (refered to henceforth as SS) developed a theory for scattering from grain boundaries in a metal beginning with a periodic array of boundaries [Sz86]. They consider both transmission and reflection at the boundaries for currents parallel and perpendicular to the boundaries. Their results for the reflection case, with current perpendicular to the boundaries, can be adapted to the problem of perpendicular transport in an LMS with reflection at the interfaces since we can consider the layers independent. By independent we mean that the electrons which go across the interface enter the new metal in local equilibrium, carrying no attributes of the metal on the other side. In the case of specular transmission the layers are not independent. Electrons specularly transmitted into metal 2 can carry drift velocity gained, from the electric field, while in metal 1.

To adapt the SS theory to the case of a LMS we will use their results to calculate the resistivities of the individual layers and then calculate  $\rho_{perp}$  for the layers in series. The particular case of the SS theory we consider is the case of diffuse and specular scattering in one dimension. In the one dimensional model there is a periodic array of barriers oriented perpendicular to the current density. The coefficients t and p represent the transmittance and reflectance respectively and 1-t-p represents the fraction of electrons diffusely scattered at the boundary. The expression for the conductivity is

$$\sigma_{\text{perp}} = 3\sigma_{\circ}C \int_{0}^{1} u^{2}H(u)du, \qquad (2.21)$$

where

$$H(u) = \alpha\Delta \left[ \ln \left( \frac{2A-1-\Delta}{2A-1+\Delta} \frac{2A\exp(\alpha)-1+\Delta}{2A\exp(\alpha)-1-\Delta} \right) \right]^{-1},$$

$$\Delta = (1-4A^2e^{\alpha})^{1/2}$$

$$\alpha = \frac{D}{\varrho_u}$$

$$A = \frac{[1+(p-t)]e^{-\alpha}}{2[1+(p-t)e^{-\alpha}]},$$

and

$$C = \frac{1+b/D}{1+b/Dt}.$$

D is the spacing between barriers, b is the barrier thickness,  $\ell$  and  $\sigma_0$  are the mean free path and conductivity of the single crystal material. Equation (2.21) refers to the conductivity of the material in this model; however, since the material has a periodic structure, equation (2.21) also represents the conductivity of a single period (layer) embedded in such a structure. It is the former interpretation which allows us to use (2.21) to represent the conductivity of a layer in a LMS.

SS take  $\ell$  and  $\sigma_0$  to represent single crystals since they are considering boundaries between crystallites, but we will use them as the bulk parameters calculated for the thick films and given in Table 2.2. SS make this same replacement when they show that their result for the case of boundaries parallel to the current reduces to the Fuchs result in the t=0 limit. We will take the barrier thickness to be zero, so that C=1, to keep the model similar to the parallel models, with the justification that Ag and Co are insoluble. D becomes the thickness of one layer:  $d_1$  or  $d_2$ . The integrals are done numerically as before.

After the conductivity of each material is found using equation (2.21),  $\rho_{\text{perp}} \ \text{is calculated using the formula for resistances in series}$ 

$$\rho_{\text{perp}} = \frac{\rho_1 d_1 + \rho_2 d_2}{d_1 + d_2} \tag{2.22}$$

where  $\rho_i = 1/\sigma_i$ . For the case of equal thickness layers,  $d_1 = d_2 = \Lambda/2$ ,

$$\rho_{\text{perp}} = \frac{\rho_1 + \rho_2}{2}.$$
 (2.23)

It is interesting that in this model the conductivity of a layer depends on the difference (p-t). If we define a parameter R=p-t, then -  $1 \le R \le 1$ . For the case of complete diffuse scattering at the interfaces p=t=0 and R=0. But since  $\rho_{perp}$  depends only on R and not on p or t individually, as long as p=t the resistivity will be the same as if there were complete diffuse scattering. R>O will increase the resistivity above the R=O value and R<O will decrease it.

For the case of transmission at the interfaces this model cannot strictly be applied since in a LMS the metals on either side of the interface are not the same whereas in the SS model the interface is a boundary in a single metal. Nevertheless we will find it informative to allow transmission within this model to get a rough idea of how transmission will affect the predictions.

A model which can be applied to some layered systems but unfortunately does not apply to Ag-Co is that of Trevedi and Ashcroft [Tr87]. They developed a theory for transport in a "superlattice with average periodic order" by considering scatterers in slabs of thickness s embedded in a metallic environment. The slabs are repeated periodically with separation d where d is less than the mean free path

of electrons in the host metal but d>>s. They include correlations between the atoms within a slab but neglect any correlation between atoms in different slabs. They solve the Boltzmann equation for this geometry and obtain both the in-plane and out-of-plane resistivity, denoted  $\rho_{\rm XX}$  and  $\rho_{\rm ZZ}$  respectively. Their solution leads to a resistivity anisotropy ,  $\rho_{\rm ZZ}-\rho_{\rm XX}$ , which can be positive or negative depending upon the thickness of the slabs. Since the requirement d>>s is never satisfied in the present samples, we cannot apply their results directly.

# 2. Band Structure Theory for LMS

by

Although many band structure calculations have been performed for semiconductor superlattices, unfortunately few have been done for LMS. In the absence of a calculation for Ag-Co, I here summarize results of a calculation for Al-Au as an illustration of what can happen to the band structure of metals when they are layered. Koehler has calculated the band structure of layered Al-Au within the nearly-free-electron theory for structures with a 2, 3 and 4 atomic planes in each layer. He chose Al-Au because these metals are both fcc and have a good lattice match. He finds the resulting Fermi surfaces to be figures of revolution about the axis normal to the layers (z) with band gaps occurring at values of the wave number associated with propagation in the z direction k<sub>z</sub> given

$$k_{z} = \pm \frac{n\pi}{\Lambda}. \tag{2.24}$$

The size of the band gaps can be large. Values from .015 to 12.2eV were found for Al-Au which has a Fermi energy of 14.0eV. He finds contributions to the band gaps from two physical properties of the metals: the valences of the two metals and their pseudopotentials. Metals with the same valence would have no contribution from the valence effect but would still have a pseudopotential contribution.

Koehler concludes that all properties of the solid which depend on the band structure will be influenced by layering. In particular he points out that for an electric field in the x direction the structure will exhibit metallic conduction but in the direction perpendicular to the layers the conductivity should be low, especially if the band gaps are large.

The biggest problem in observing such band structure effects in LMS is that, for most systems produced to date, the electron mean free path is shorter than the period of the structure [Gu86]. In the case of small  $\ell$ , the basic assumption that the electronic wavefunctions can be described by Bloch functions with the periodicity of the superstructure breaks down and one cannot expect to observe band gap effects.

#### 3. Superconductor - Normal Metal Interfaces

A perpendicular transport sample is made up of three films: the bottom Nb strip, the sample film and the top Nb strip (see Figure 1.1). The Nb strips function as both potential and current leads for a four-probe resistance measurement. The measured resistance includes the resistance of the sample film  $\mathbf{R}_{\mathbf{S}}$  as well as the resistance due to the interfaces between the superconducting leads and the sample film  $\mathbf{R}_{\mathbf{i}}$ .

The resistance of a SN interface has been studied both experimentally and theoretically by several workers. Pippard et al. [Pi71] measured the interface resistance in SNS sandwiches and reported that R<sub>i</sub> rises as the transition temperature of S (T<sub>c</sub>) is approached from below with the main effect taking place above  $0.8T_{\rm c}$ . Hsiang and Clarke [Hs80] studied various SNS sandwiches, some made by successive evaporation and others consisting of a foil with a superconducting film evaporated onto each side. They found R<sub>i</sub> to be zero within experimental error (~1%) at T~0.4T<sub>c</sub>. R<sub>i</sub> increased with increasing T with the largest part of the increase above  $0.8T_{\rm c}$ .

Hsiang and Clarke, Pippard et al. and others (see [Ha74, Wa75]) have considered the SN interface problem theoretically. The basic mechanism is as follows.

1. In the T<<T<sub>C</sub> limit, quasiparticles from the N side encountering the NS interface are reflected with a change of character; electrons are reflected as holes and vice versa (this is called Andreev reflection). There is a small boundary resistance associated with this process due to the fact that the quasiparticles are scattered over a finite distance in S. The distance is  $\sim \xi_0$  in a clean superconductor (clean means  $\ell >> \xi_0$ ) and it is  $\sim (\xi_0 \ell)^{1/2}$  in a dirty superconductor (dirty means  $\ell << \xi_0$ ) where  $\xi_0$  is the BCS coherence length of S and  $\ell$  is the normal state mean free path in S. The resulting interface resistance is given by

$$R_i \sim \rho_s \xi_o / A$$
 ,  $\ell >> \xi_o$ ,  $T << T_c$ 

$$R_i \sim \rho_s(\xi_0 \ell)^{1/2}/A$$
 ,  $\ell < \xi_0$ ,  $T < T_c$  (2.25)

where  $\rho_s$  is the normal state resistivity of S and A is the area of the interface. For the Nb-Ag interface in our samples we find R  $_i$ ~10 $^{-9}\Omega$  (approximately 2% of the sample resistance).

2. In the case of  $T \sim T_c$ , some quasiparticles enter over the superconductor energy gap  $\Delta$  and propagate into S. The result is an additional interface resistance that increases rapidly as  $T + T_c$ . In the limit as T + 0 this contribution to  $R_i$  decreases exponentially as  $\exp(-\Delta/k_BT)$ .

In the present work we are concerned with measuring the sample resistance, the SN interface resistance is a side-effect of the measurement technique which we will try to eliminate. To minimize the magnitude of the interface resistance we can perform measurements at  $T\!<\!<\!T_c$ . If it is found that  $R_i$  is significant, even at low temperatures, it is possible, in principle, to determine the interface resistance by measuring the resistance of samples which are identical in every way except their total thickness. The measured resistance  $R_m$  of a sample is given by

$$R_{m} = \rho_{S} \frac{t}{\Delta} + R_{i} \tag{2.26}$$

where  $\rho_s$  is the resistivity of the sample film, t is its thickness and A the cross-sectional area. A plot of R versus t for a set of such samples would be linear. The slope and intercept would give  $\rho_s$  and R respectively.

### 4. Experiment

# a. Technique for Measuring the Perpendicular Resistivity

The preparation of the films has been described in Chapter 1. Here we describe the procedures used to make electrical and thermal contact with the sample and perform the resistivity measurements.

The perpendicular measurements can only be made in the temperature range where the Nb strips are superconducting, i.e. T < 9K. Since the SN interface resistance is large for  $T > \frac{1}{2}T_c$  we must use a refrigerator capable of reaching temperatures below 4.2K. A schematic view of the refrigerator, designed and built by W.P. Pratt, Jr. and V.O. Heinen, is shown in Figure 2.8. The calibrated Ge resistance thermometer is used in a feedback circuit with the heater to control the temperature. This refrigerator typically reaches a minimum temperature of 1.3K and, using the heater, measurements can be taken at temperatures up to approximately 9K. Thermal contact is made between the refrigerator and the sample by fixing the sapphire substrate to a flat Cu holder with a thin layer of Apiezon [AP] "N" grease.

The total thickness of a film is typically 0.5 to 1 $\mu$ m and the width of the Nb strips is 1mm (the problem of determining the actual width of the strips is discussed in Chapter 1). The resulting resistance of a perpendicular transport sample is then  $\sim 0.05 \mu\Omega$  at 4.2K. In order to measure such a small resistance with accuracy we used the SQUID based circuit shown in Figure 2.9, where the SQUID is used as a null detector. The ratio of the reference current  $I_{ref}$  to the current through the sample  $I_s$  is adjusted, using a high precision current comparator, to null the current through the SQUID. When the circuit is balanced the

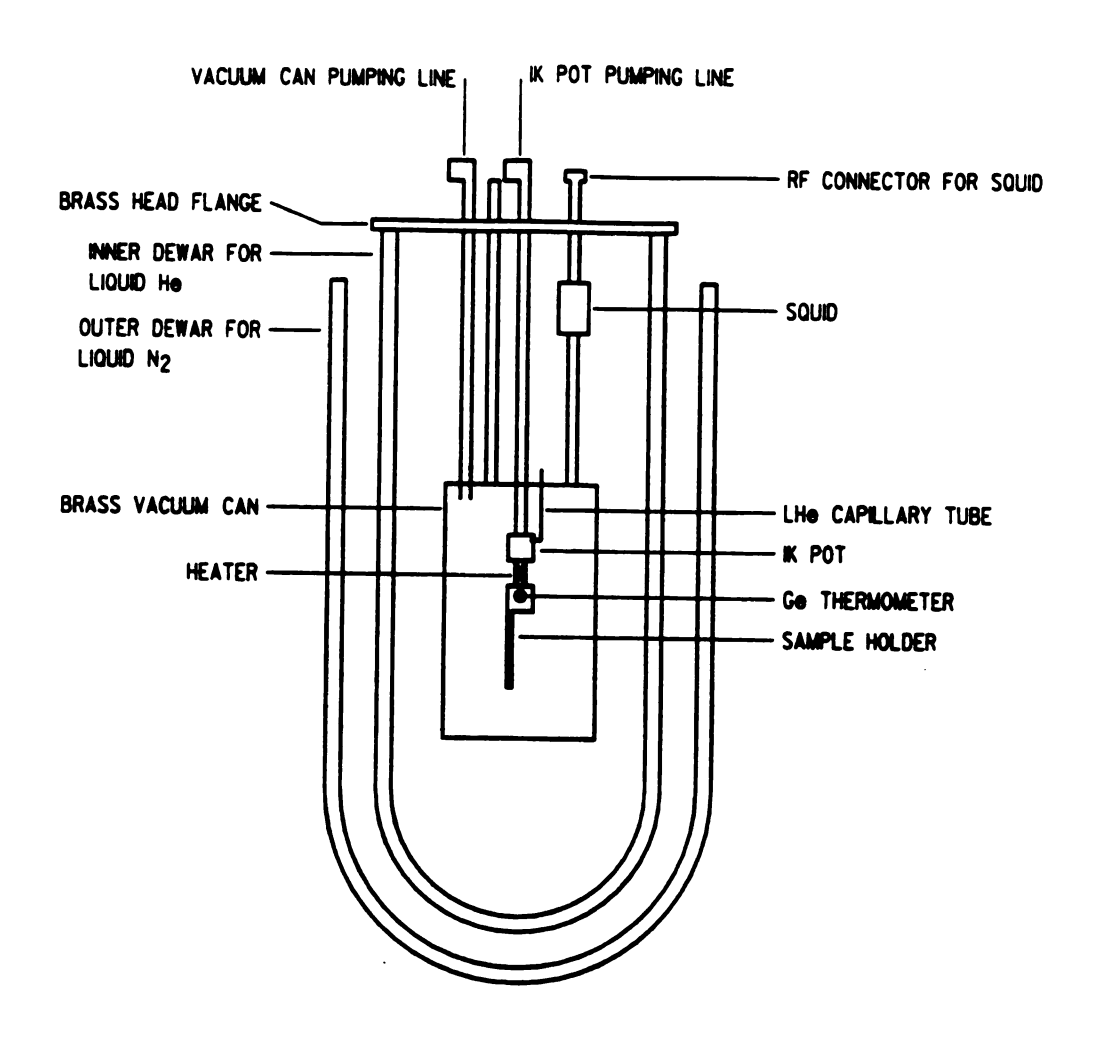


Figure 2.8 Schematic view of "1K" refrigerator.

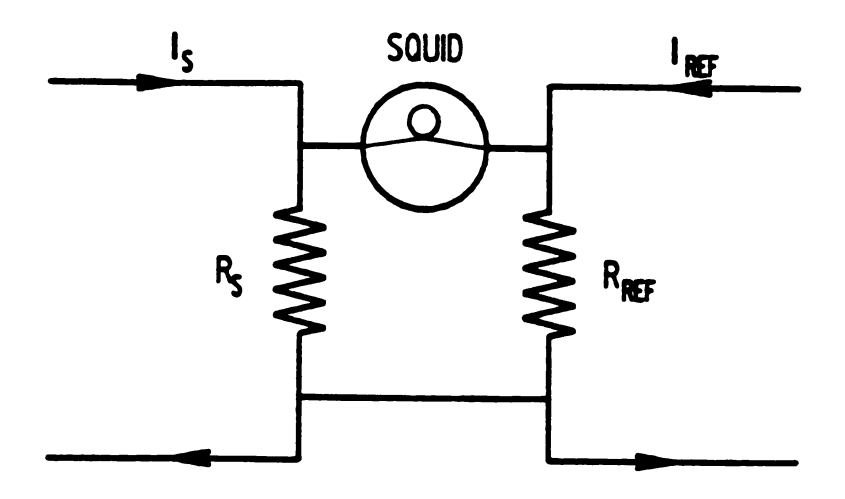


Figure 2.9 SQUID circuit for resistance measurement.

ratio of the sample resistance  $\mathbf{R}_{\mathbf{S}}$  to the reference resistance  $\mathbf{R}_{\mathbf{ref}}$  is given by

$$\frac{R_s}{R_{ref}} = \frac{I_{ref}}{I_s}.$$
 (2.27)

A 1.6 $\mu\Omega$  Cu(Ag) alloy reference resistor was used for the measurements presented here. Details of the current comparator can be found in Edmunds et al. [Ed80]. For a more detailed description of the use of this equipment for measuring small resistances and the special considerations involved in measuring small resistances at low temperatures see Steenwyk [St80] Chapter II.

It is important to make superconducting contact between the Nb strips and the four Niomax CN [IMI] wires used for the measurement. The current contacts should be superconducting to eliminate the problem of ohmic sample heating by the current flow through those contacts. The potential contacts should be superconducting since the sensitivity of the SQUID decreases as the resistance of the SQUID circuit increases. The contacts were made by first applying In to the Nb strip with an ultra-sonic soldering iron. The excess In was then cut off with a razor blade leaving only a thin sheet of In, approximately 0.5mm thick. The Niomax wire, which was tinned as described in Steenwyk [St80] page 76, was then soldered to the In using Cerroalloy 117 and an ordinary soldering iron. No flux was used on the sample during the soldering process.

### b. Simple film measurements

In order to test the perpendicular technique we produced samples in which the sample films were pure Ag or pure Co. When the sample film

was Ag, 75Å Ag overlayers were deposited on the Nb strips immediately after completing the strips. With Co sample films, two kinds of overlayers were used on the Nb strips: Ag and Co. The two types of Co samples, those with Co directly in contact with the Nb and those with a 75Å Ag layer between the Co and the Nb, were made to check how much the SN interface resistance is dependent on the details of the interface between the sample film and the Nb strip.

Figure 2.10 shows  $\rho_{meas}$  versus T for a 2.8µm thick Ag film and a 0.7µm thick Co film. In both cases the rise due to the SN interface contribution as T + T is clear.

At low T the Ag film begins to superconduct, at suitably low sample current, due to the proximity effect. The fact that the Ag film superconducts shows that impurities deposited near the NS interface during sample production do not form a barrier through which the Cooper pairs cannot tunnel. Therefore in all of the samples we can safely assume that the thin Ag layer between the Nb and the first Co layer is superconducting.

The Co film does not even show current dependence at the lowest temperature, indicating that the ferromagnetism effectively inhibits the proximity effect in this sample.

The residual resistivities of the samples are in good agreement with measurements made in the parallel geometry.

Table 2.4 lists the pure film samples made and their characteristics.

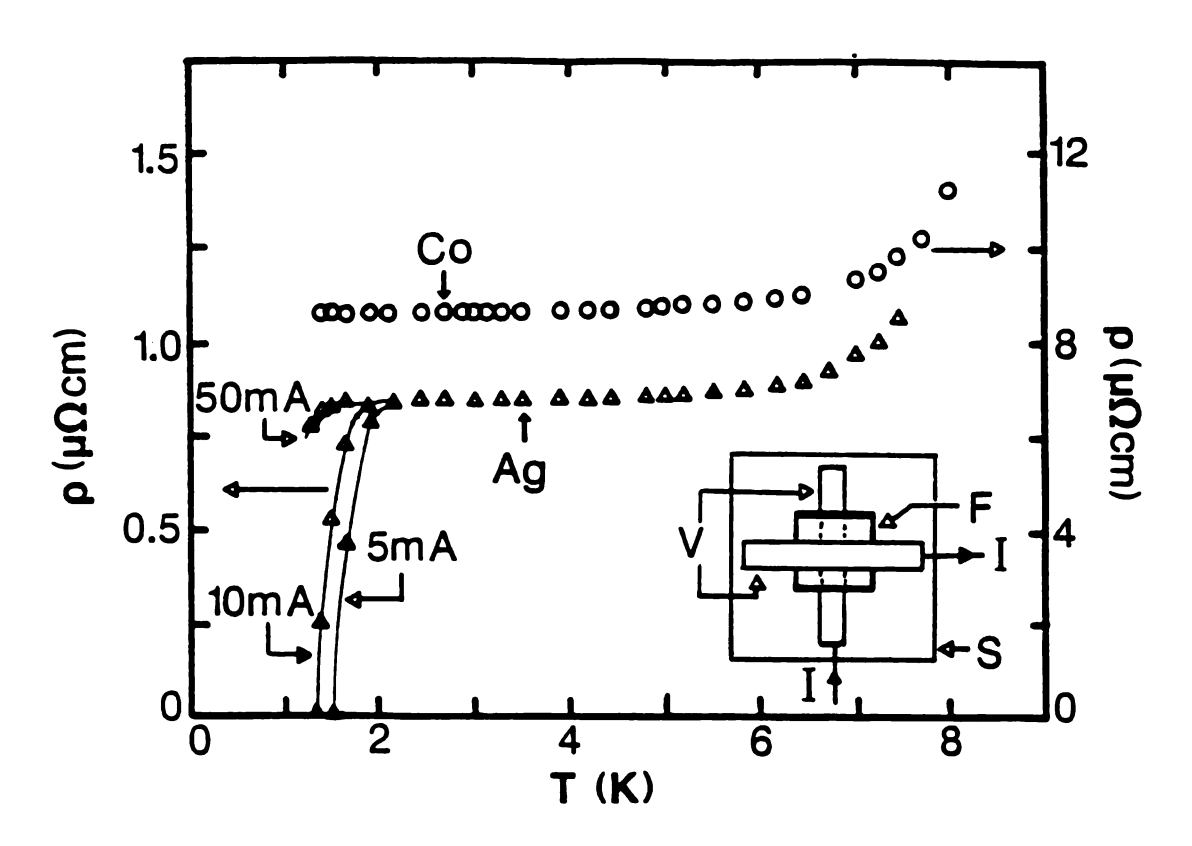


Figure 2.10 Perpendicular resistivity for pure films of Ag and Co.

Table 2.4 Pure film samples for  $\rho_{\mbox{\scriptsize perp}}$  measurements

sample	description	t	A/t	ρο	ρ(4.2K)
		( µm )	(cm)	(μΩem)	(μΩcm)
8004	Co with Co overlayers	.70	166	6.06	6.10
7504 <b>*</b>	Co with Co overlayers	.60	290	7.13	7.37
7104	Co with Ag overlayers	1.40	89.5	7.31	7.47
6602	Co with Ag overlayers	.69	174	7.94	8.25
6604**	Co with Ag overlayers	. 69	160	6.64	6.85
6401	Ag	2.70	39.5	.929	.973
6402***	Ag - paused 5 min. at	2.69	44.8	.945	1.01
	Nb-Ag interface				

The samples with asterisks have larger than normal uncertainties associated with the measurements of the sample geometry for the reasons listed below.

<sup>\*</sup> Sample has a Nb strip with fuzzy edges and large substrate curvature.

<sup>\*\*</sup> Sample has large substrate curvature.

<sup>\*\*\*</sup> Sample has a Nb strip with fuzzy edges.

### c. Sandwich Samples

In order to test the ability of thin layers of Co to inhibit the proximity effect we produced sandwich samples made of a thick film of Ag with thin layers of Co near the SN interfaces as shown in Figure 2.11. Samples were made on both cool ( $T\sim30^{\circ}$ C) and hot ( $T\sim80^{\circ}$ C) substrates.

The results are shown in Figure 2.12. A sample with 25Å of Co near the SN interfaces made on a cool substrate shows no current dependence even at the lowest temperature. The same type of sample made on a hot substrate shows a large current dependence for T<6.5K and becomes superconducting at the lowest temperatures for  $I_s \le 25 \text{mA}$ . A sample with 15Å of Co shows a current dependent resistance but does not become superconducting even at the lowest temperatures and with  $I_s = 5 \text{mA}$ .

We interpret these results as follows. The Co layers are effective in inhibiting the proximity effect as long as they are continuous. As the Co layers get thinner they develop gaps. If the substrate is hot the gaps develop at greater Co thickness than if the substrate is cool. This interpretation is consistent with the X-ray measurements which show a loss of coherent layers for  $\Lambda<20\text{\AA}$  in samples made on cool substrates and for  $\Lambda\sim80\text{\AA}$  in samples made on hot substrates.

### d. LMS Samples

The resistance of LMS samples with  $\Lambda$  between 23 and 380Å having equal Ag and Co thickness was measured using the perpendicular technique. Table 2.5 lists the characteristics of these samples. Figure 2.13 shows  $\rho$  versus T for a typical LMS sample (8001). The expected upturn as T + 9K is observed. At the lowest temperatures the

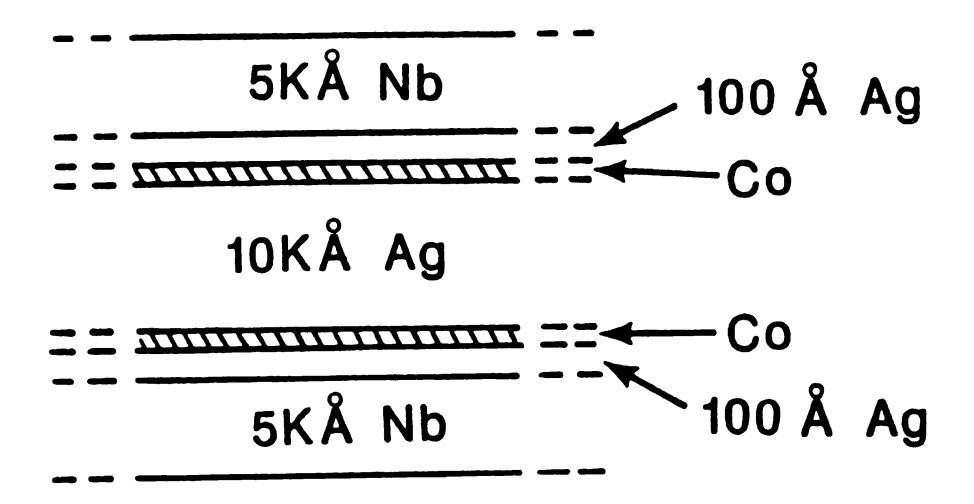


Figure 2.11 Geometry of sandwich samples.

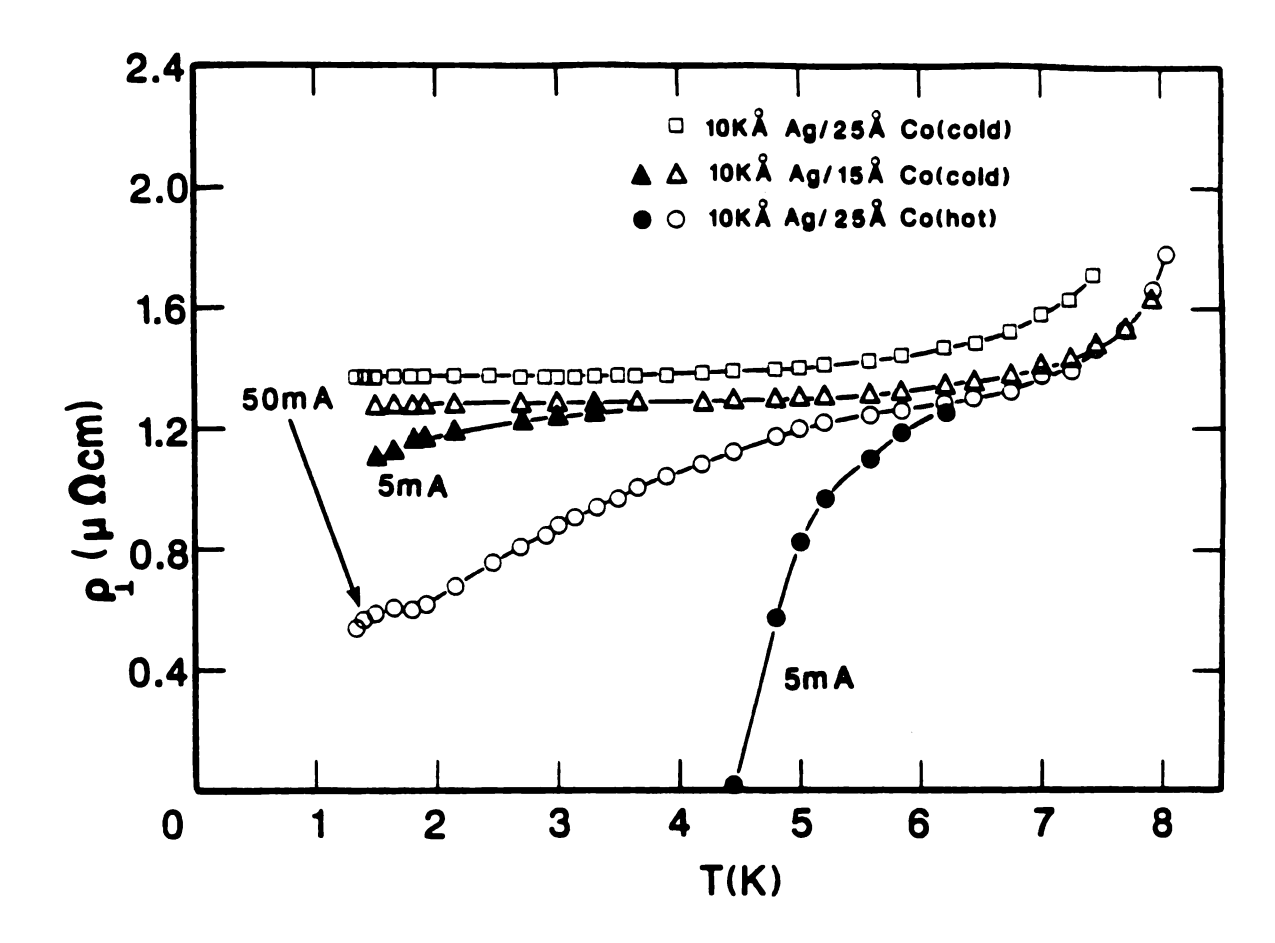


Figure 2.12 Perpendicular resistivity of sandwich samples.

Table 2.5 LMS samples for  $\rho_{\mbox{\footnotesize{perp}}}$  measurements

sample	Λ	t	A/t	ρ٥	ρ(4.2K)
	(Å)	(µm)	(cm)	(μΩcm)	(μΩcm)
5201	85.1	1.068	118	12.30	12.90
5202	57.1	0.716	175	11.72	12.16
5901	81.8	1.026	117	15.08	15.71
5902	23.7	1.186	118	16.7	18.3
5903	39.0	1.086	111	13.49	13.93
<b>7</b> 501	380	0.475	270	9.22	9.44
7502	85.2	0.532	229	16.94	17.37
7503	40.0	0.554	221	13.5	13.6
8001	72.3	0.452	253	13.6	13.8
8002	25.4	0.636	189	16.02	16.38
8003	191	0.487	248	12.72	12.86

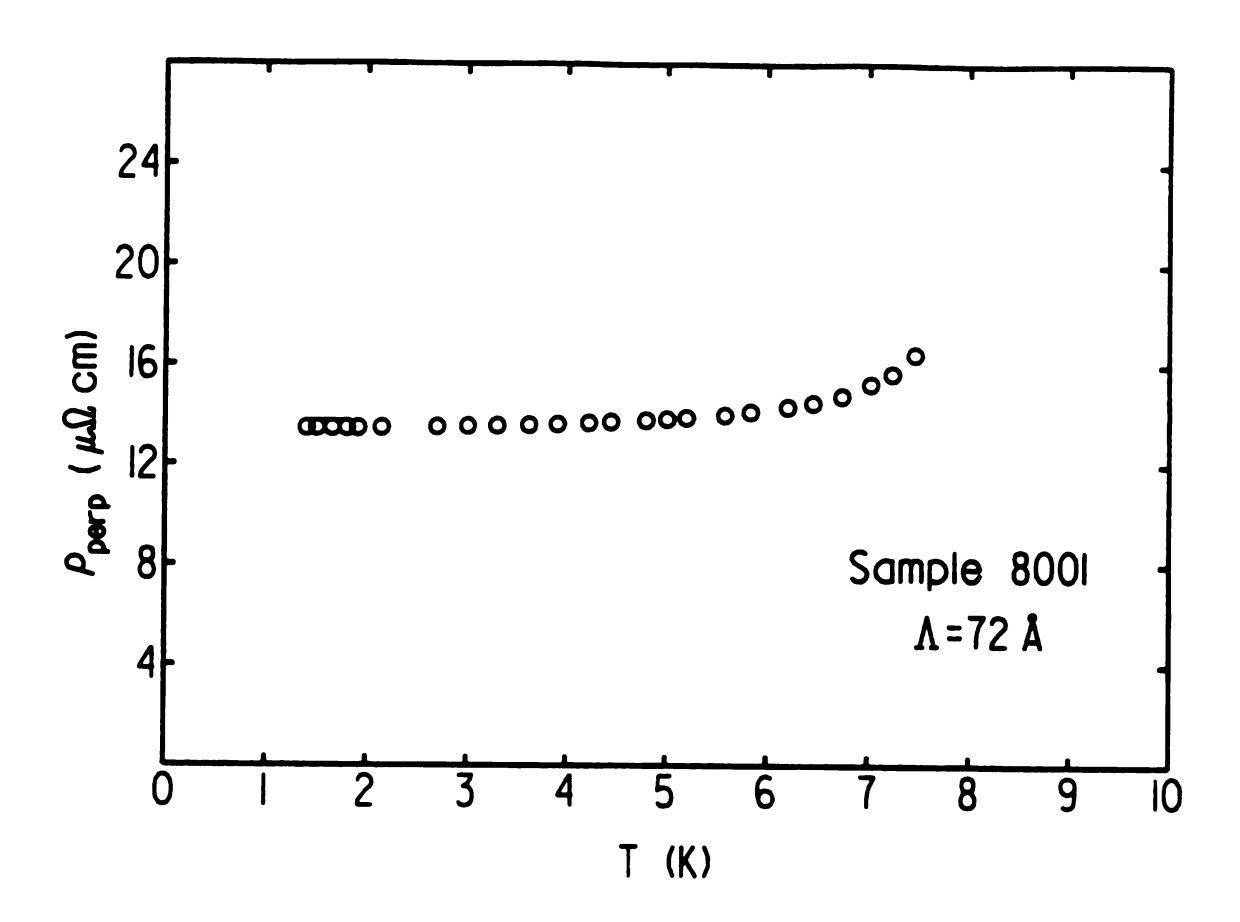


Figure 2.13 Perpendicular resistivity of LMS sample 8001.

resistivity saturates, this value of  $\rho_{\mbox{\footnotesize{perp}}}$  is the measured residual resistivity  $\rho_{\mbox{\footnotesize{o}}}.$ 

Figure 2.14 shows  $\rho_0$  versus  $\Lambda$  for the LMS samples listed in Table 2.5 as well as the  $\rho_{par}$  data for comparison. The scatter in these data is too large to be accounted for by the experimental uncertainty.

The curves shown in the figure were calculated from the modified SS theory. Note that the R=O curve rises far too quickly with 1/ $\Lambda$  to fit the data. If we assume that there is no transmission, t=O, then the R=O curve is the lower limit of  $\rho_{perp}$ . The curves with R<O show the effect of allowing transmission within this model. Even though the model is not valid for t≠O, as explained above, the R<O curves give a qualitative idea of what happens when transmission is allowed. The large  $\Lambda$  limit is the same for any model since in this limit the problem reduces to the bulk film resistances in series. For the parameters used  $\rho_{perp}(\Lambda+\infty)$  = 4.62 $\mu\Omega$ cm. Even if the curvature of the R<O curves is wrong due to the failure of the assumptions of the model, the basic behavior (that they fall below the R=O curve and extrapolate to 4.62 $\mu\Omega$ cm) must be very similar to that which one would find with a model which treats transmission correctly..

The perpendicular measurements make clear that transmission of electrons through the interfaces dominates reflection (since  $R\sim-0.5$ ). This result taken together with the results of the two models of parallel transport indicate that, within a free electron model, the transmission coefficient is  $\sim1/2$ . There may also be some reflection but the reflection coefficient is much smaller than that for transmission.

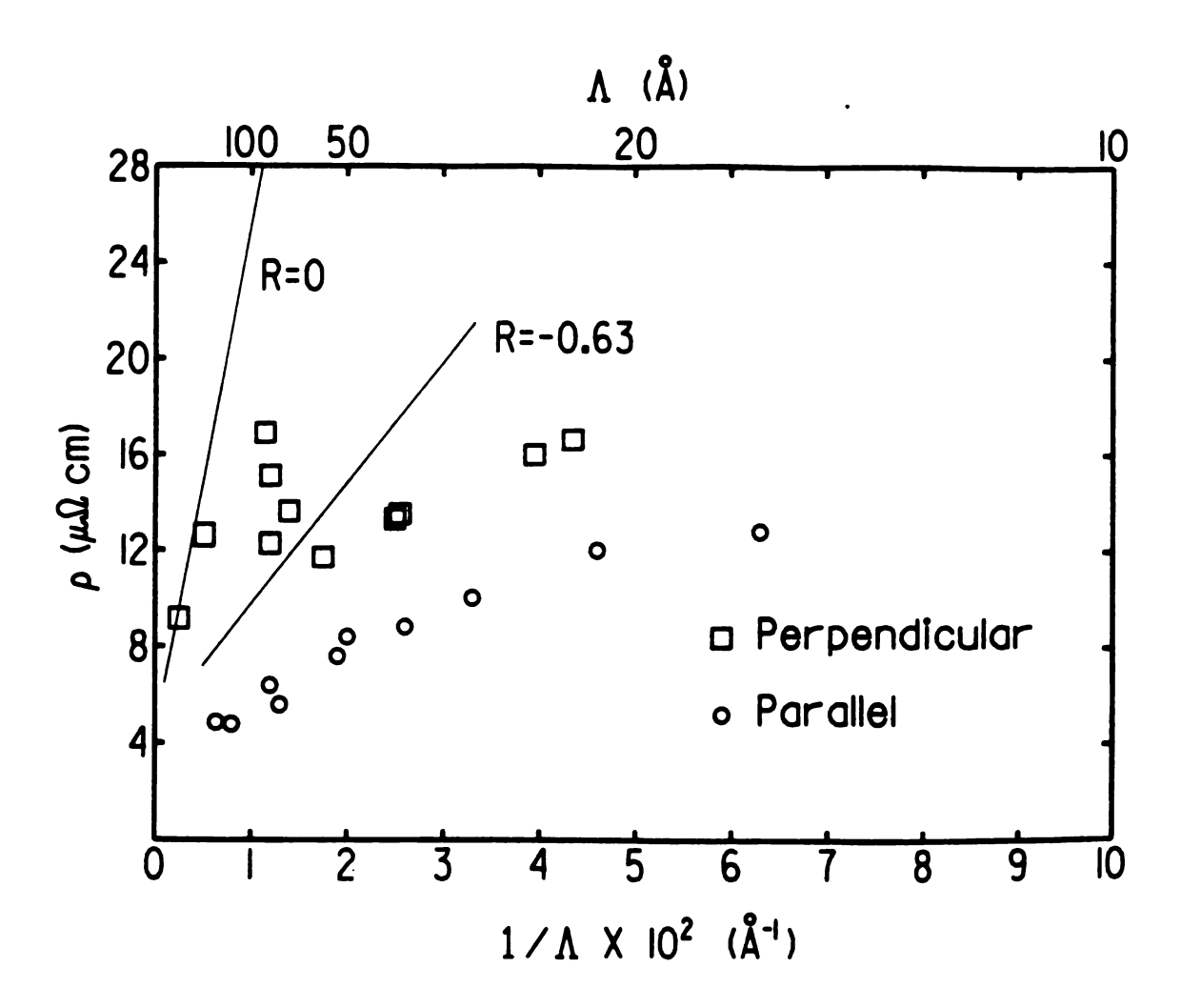


Figure 2.14  $\rho_0$  (perpendicular) versus  $1/\Lambda$ 

The source of the scatter is not clear. The pure film and sandwich measurements imply that the technique works, even though the uncertainty in the absolute resistivity is approximately  $\pm 10\%$ .

One possible source of scatter is differences in the quality of the samples due to variations in the substrate temperature. The perpendicular resistivity is sensitive to the substrate temperature effects. LMS samples made on hot substrates have much lower resistivity than those made on cold substrates. Since the X-ray data for the samples made on hot substrates shows that the layering is very poor, the low resistivity is understandable. As the layering breaks down, the Co layers (having higher resistivity) develop thin spots or gaps and become shorted by the Ag. Once the substrate temperature effect was discovered we were careful to make samples on room temperature substrates and only those samples made on cool substrates are included in the  $\rho_{perp}$  data. The X-ray spectra for the samples made in this way are almost identical. Even though differences in the quality of the layers is expected to effect  $\rho_{perp}$ , given the care taken in making the samples and the X-ray data, the scatter seems too large to be explained by this effect only.

Another possibile source of scatter is band structure effects. Koehler's calculations for Al-Au show that small differences in structure can lead to significant changes in the band structure and thus significant changes in  $\rho_{perp}$ . The values of  $\ell_{eff}$  calculated from the  $\rho_{par}$  data are two or three times the structural period. Perhaps such a mean free path is on the lower limit of that needed to see band gap effects.

#### CHAPTER 3

## MAGNETIZATION, HALL EFFECT AND MAGNETORESISTANCE

#### A. MAGNETIZATION THEORY

Since Co is ferromagnetic in both the hcp and fcc phases, we expect the Co layers to dominate the magnetic properties of the Ag-Co LMS.

# 1. Crystallographic Anisotropy

Before considering the magnetic properties of thin films of Co we will first review the properties of bulk Co. In bulk hcp-Co the hexagonal axis (c-axis) is the direction of easy magnetization and all directions in the basal plane are hard directions [Ki49]. This uniaxial anisotropy is very large compared to anisotropies found in Fe (bcc) or Ni (fcc). Typically one defines the anisotropy energy density  $K_v$  to be the extra work done in magnetizing along the hard axis per unit volume. For the Co basal plane  $K_v$  ( $\approx 5$  X  $10^5$  J/m $^3$ ) is about one order of magnitude larger than for the hard directions of Fe and Ni. Crystals of fcc-Co have been studied at temperatures above  $550^{\circ}$ C by Sucksmith et al. [Su54]. They find that for fcc-Co the easy direction is along the (111) axis and that both the behavior and magnitude of the anisotropy are very similar to Ni (i.e. hcp-Co is far more anisotropic than fcc-Co).

In principle it is very simple to discriminate between fcc and hcp Co from magnetic measurements due to the large uniaxial anisotropy of the hcp-Co. Unfortunately, for the present samples, there are

additional considerations that make the analysis of the magnetic measurements more complicated.

- 1. The Co layers are not single crystal but polycrystalline and textured. The fact that they are textured leaves hope that the anisotropy can be observed even though the layers are polycrystalline.
- 2. The demagnetizing effects associated with the thin film geometry are large and must be taken into account.
- 3. There may be magnetostriction effects since the Co layers are probably strained by their contact with the Ag layers.

### 2. Shape anisotropy

It is useful to think about the problem of thin film magnetism in terms of an internal magnetic field  $\vec{H}_{in}$  which is the sum of two parts; the applied field  $\vec{H}_{a}$  and the demagnetizing field -nM where M is the magnetization and n is the demagnetizing factor (MKS units).

$$\vec{H}_{in} = \vec{H}_{a} - n\vec{M} \tag{3.1}$$

The associated flux density  $\vec{B}_{in}$  is given by

$$\vec{B}_{in} = \vec{B}_{a} + \mu_{o} (\vec{M} - n\vec{M})$$
 (3.2)

where  $\vec{B}_a = \mu_0 H_a$  is the applied flux density and the demagnetizing factor n is determined by the shape of the object in question. Figure 3.1 defines the orientation of the ferromagnetic film. For a thin film with  $\vec{H}_a = H_a \hat{z}$  (normal to the surface) n is unity and for  $\vec{H}_a = H_a \hat{x} + H_a \hat{y}$  (parallel to the surface) it is zero. Since  $\vec{H}_{in}$  is zero in a

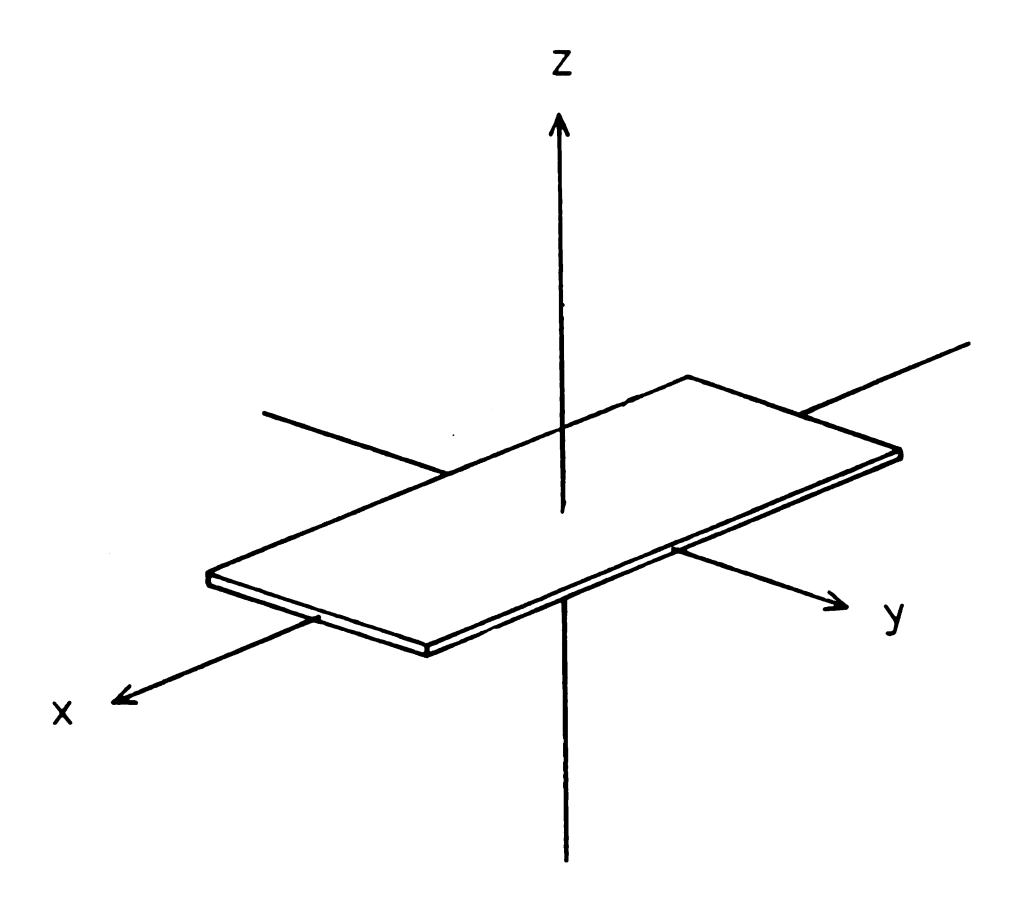


Figure 3.1 Orientation of the thin film.

ferromagnet when the magnetization is not saturated, equation (3.1) implies that  $\vec{H} = \vec{H}_a$  if  $\vec{M}$  is not saturated and  $\vec{H}_a = \vec{H}_a \hat{z}$ . The saturation field  $\vec{H}_s$  (the field required to saturate the magnetization of the sample) is then given by

$$H_s = M_s$$
 (field applied normal to surface) (3.3)

and the associated saturation flux density is  $B_s = \mu_0 M_s$ . If  $\vec{H}_a$  is in the x-y plane then  $\vec{H}_{in} = \vec{H}_a$  and we expect  $\vec{M}$  to saturate quickly as  $H_a$  is increased. In other words, the demagnetization effect causes the easy axis to be in the plane of the film (for a very thin film).

The structure of ferromagnetic domains in single crystal thin films has been theoretically studied by Kittel [Ki46]. He calculated the free energy of a film for three different domain structures as a function of film thickness. The free energy F for a sample of volume V is represented as the sum

$$F = F_{u} + F_{m} + F_{a},$$
 (3.4)

where

 $F_{w}$  = surface energy of the boundary surfaces between domains;

 $F_m$  = magnetic field energy of the configuration;

 $F_a$  = anisotropy energy of spin orientation

 $= K_{v}V.$ 

F is a minimum for a stable configuration. The problem is then to find the minimum F for the three domain configurations under consideration.

His calculations show that, for Co films with thickness less than  $\sim 300 \, \text{Å}$ , domains with  $\vec{\textbf{M}}$  parallel to the film surface have a lower energy than those with  $\vec{\textbf{M}}$  normal to the surface. Assuming that the Ag layers in a Ag/Co LMS are thick enough to decouple the magnetic Co layers, we should expect to find the easy axis parallel to the layers.

# 3. Surface anisotropy

Considering the above discussion we would expect the magnetization to behave as shown in Figure 3.2. But so far we have neglected the fact that, in a thin film, a large fraction of the atoms are at the surfaces where they are exposed to a ferromagnetic environment on only one side and therefore may feel interactions that would cancel in the bulk. Such surface effects lead to a "surface anisotropy" in the magnetic properties of the LMS. We can expect a surface anisotropy to be dependent upon the modulation wavelength  $\Lambda$  since the fraction of atoms at interfaces increases with decreasing  $\Lambda$ . But finding a  $\Lambda$  dependence in magnetic properties is not enough to prove that a surface anisotropy is present since other  $\Lambda$ -dependent effects may be present. For example the saturation magnetization of Ni has been found to decrease with layer thickness in the Ag-Ni LMS [Kr86, Sa87]. In order to separate surface anisotropy from other effects one must have a model which predicts a particular functional dependence on  $\Lambda$ .

Koepke and Bergmann (KB) have shown that, for thin films of Fe evaporated onto non-magnetic metal alloy substrates, the thickness dependence observed in the saturation field can be attributed to a

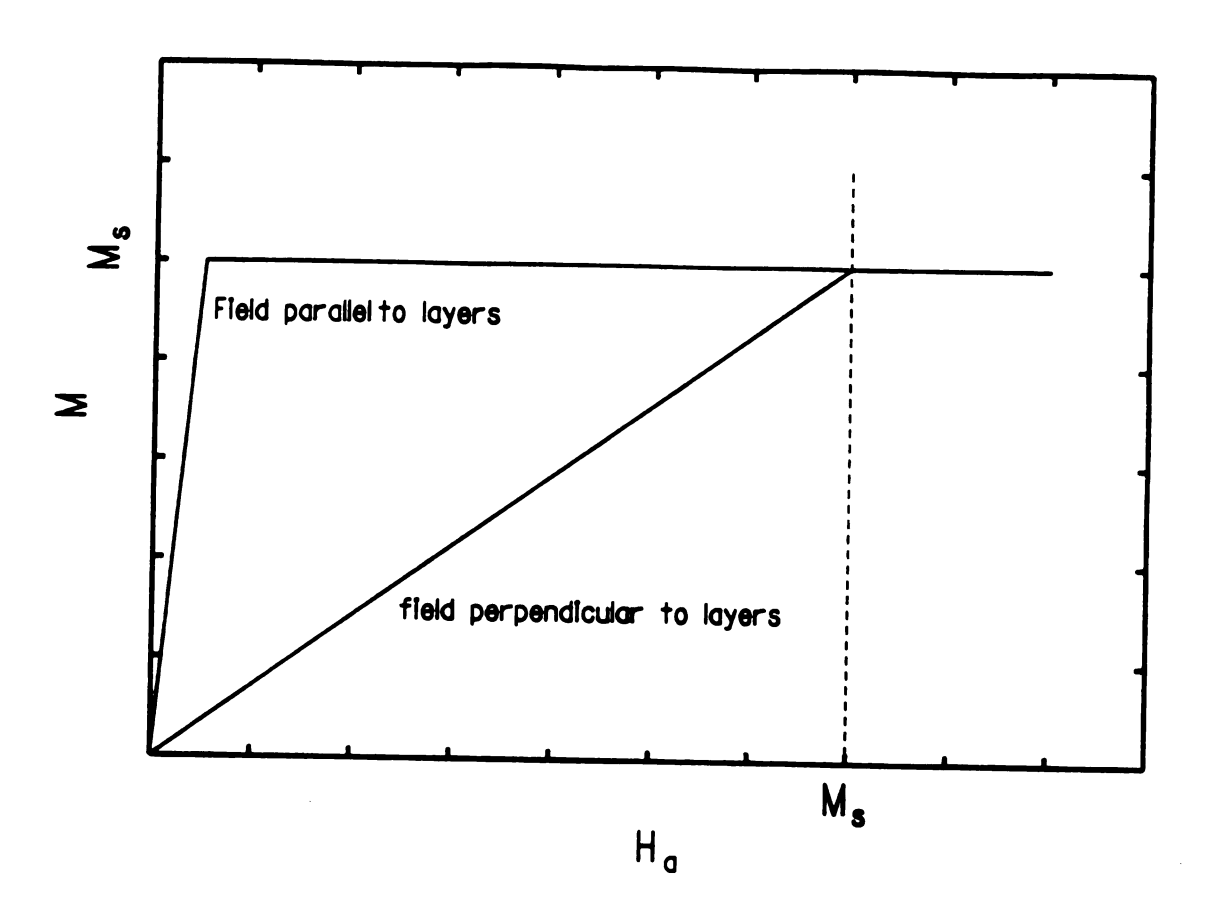


Figure 3.2 M versus  $H_a$  for a thin film with only shape anisotropy.

magnetic interface anisotropy with a surface energy density o of the form [Ko75]

$$\sigma = K_{s} \cos^{2} \Theta = \frac{K}{2\mu_{o}} M_{z}^{2}. \tag{3.5}$$

Equation (3.5) is the form predicted by Neel [Ne54] where  $\theta$  is the angle between the surface normal and  $\vec{M}$ ,  $K_S$  and K are constants. KB consider contributions to the energy of the film from three sources: the magnetization in the external field, the magnetization in the demagnetizing field and the interface anisotropy surface energy. They minimize this energy with respect to  $M_Z$  to find the equilibrium state. The result is that the additional energy, associated with the interfaces, yields a contribution of  $-4K_SM_Z$  /  $\mu_0M_S^2$ d to the internal field and leads to the following relationship between the saturation field  $H_S$  and  $M_S$ :

$$H_s = M_s + \frac{4K_s}{\mu_o M_s} \frac{1}{d}$$
 (field normal to interface) (3.6)

where d is the thickness of the magnetic layer and  $H_{\mathbf{S}}$  is applied normal to the film surface. Since Koepke and Bergmann studied single films of Fe on a substrate, his K contains contributions from the interface with the vacuum and the interface with the substrate. In the case of a LMS, K contains contributions from two identical interfaces.

Including the contribution of the surface-anisotropy field, equation (3.1) becomes

$$\vec{H}_{in} = \vec{H}_{a} - n\vec{M} - \frac{4K_{s}M_{z}}{\mu_{o}M_{s}^{2}} \frac{1}{d}$$
 (field normal to interface). (3.7)

If K>O then the interface anisotropy field is parallel to the demagnetizing field but if K<O they are antiparallel. Note that for K<O the competition between the interface anisotropy field and the demagnetizing field could lead to a change in the easy axis direction for small enough d.

If there is an anisotropy in the bulk material which can be characterized by a volume energy density  $K_{V}$  (such as in single crystal Co), then equation (3.6) would become [Pe87]

$$H_{S} = M_{S} + \frac{2K_{V}}{\mu_{o}M_{S}} + \frac{4K_{S}}{\mu_{o}M_{S}} - \text{ (field normal to interface)}.$$
 (3.8)

The corresponding saturation flux density is given by

$$B_s = \mu_0 M_s + \frac{2K_v}{M_s} + \frac{4K_s}{M_s} \frac{1}{d}$$
 (field normal to interface). (3.9)

## B. HALL EFFECT THEORY

The Hall resistivity  $\boldsymbol{\rho}_{\boldsymbol{H}}$  of a metal is defined as

$$\rho_{\rm H} = \frac{E_{\rm y}}{J} \tag{3.10}$$

where the current density J is in the x-direction, the applied magnetic field is in the z-direction and  $E_y$  is the electric field in the y-direction (see Figure 3.1). The Hall resistivity of ferromagnetic metals can be written as

$$\rho_{H} = R_{o}B_{a} + R_{s}M_{z} \tag{3.11}$$

where R<sub>o</sub> and R<sub>s</sub> are the normal and anomalous Hall coefficients respectively and M<sub>z</sub> is the magnetization perpendicular to the film. The normal term arises from the Lorentz force acting on the conduction electrons. The anomalous term is due to asymmetric scattering of the conduction electrons in a ferromagnetic metal. In a plot of  $\rho_H$  vs. B<sub>a</sub>, the anomalous part dominates at low field giving a curve with positive slope if R<sub>S</sub>>0 or negative slope if R<sub>S</sub><0. If equation (3.7) is valid then the curve should be linear at low field. There is a kink in the curve at the saturation field H<sub>S</sub> (when M<sub>Z</sub>=M<sub>S</sub>). For fields higher than H<sub>S</sub> the curve is given by

$$\rho_{H} = R_{o}B_{a} + R_{s}M_{s}. \tag{3.12}$$

Figure 3.3 illustrates the typical form of the Hall resistivity curve.

The anomalous Hall effect is thought to have two contributions: skew scattering and side-jump scattering [Be70, Hu72]. Skew scattering is classical asymetric scattering caused by a spin-orbit interaction and results in a linear dependence of  $R_{\rm S}$  on the total resistivity  $\rho$ . Side-jump scattering is a nonclassical effect in which a free electron wave packet undergoes a sideways displacement at the scattering centers resulting in a quadratic dependence of  $R_{\rm S}$  on  $\rho$ . There are many theories concerning the microscopic scattering mechanisms in both cases but a discussion of these mechanisms is beyond the scope of this thesis. A review of the subject and many references can be found in reference [Hu72].

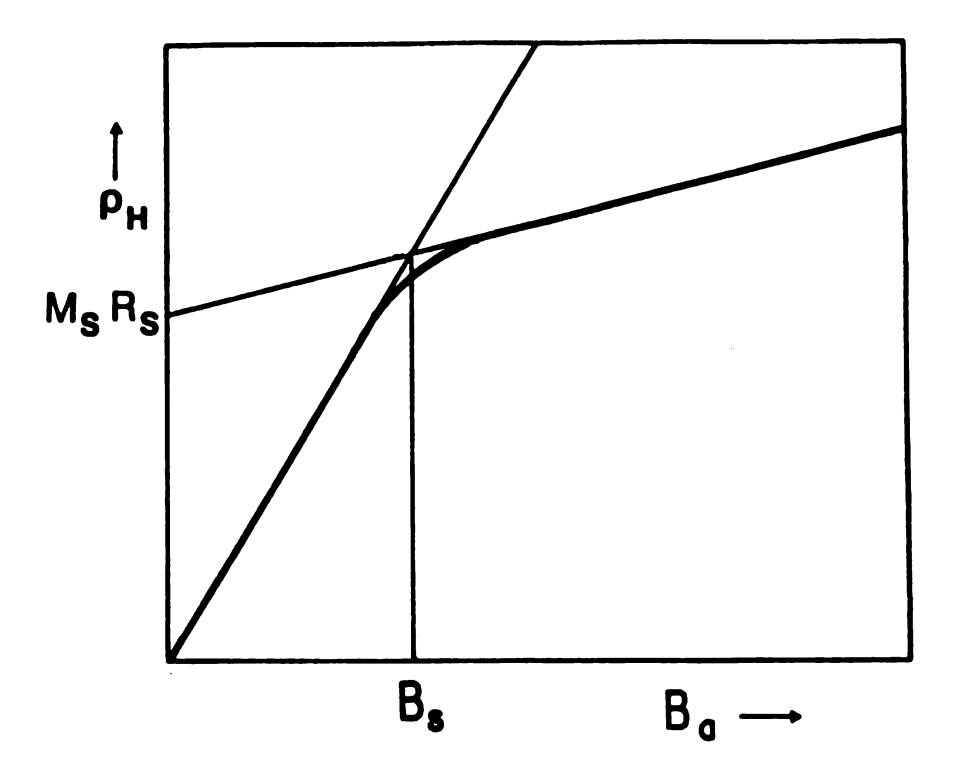


Figure 3.3 Expected form of  $\rho_H$  versus  $B_a$ .

## C. MAGNETIZATION MEASUREMENTS

The magnetization of the samples was measured at 4.2K on a SHE model 905 SQUID magnetometer [SHE] having a maximum field of approximately 1T. For measurements with the field parallel to the layers the samples were sealed in small plastic bags suspended from a string. For the perpendicular field measurements the samples were mounted inside a plastic bucket so that they were held horizontal. Figure 3.4 shows the magnetization versus  $B_a$  for samples with  $\Lambda = 15 \mbox{\normalfont A}$  and  $\Lambda = 151 \mbox{\normalfont A}$ . The figure illustrates the expected shape anisotropy effects: M quickly saturates when  $\mbox{\normalfont B}_a$  is parallel to the layers and increases appoximately linearly when  $\mbox{\normalfont B}_a$  is perpendicular. The maximum field available was not enough to saturate M in the perpendicular case for any of the samples measured. As a result the magnetization measurements gave us  $\mbox{\normalfont M}_a$  but not  $\mbox{\normalfont B}_a$ .

Figure 3.5 shows  $M_s$  versus  $\Lambda$  for Ag-Co LMS.  $M_s$  for a 5000Å pure Co film is shown as an arrow on the right border. We find  $M_s$  to be constant and equal to the thick film value for  $\Lambda \ge 40$ Å with a slight decrease with decreasing  $\Lambda$  for  $\Lambda < 40$ Å.

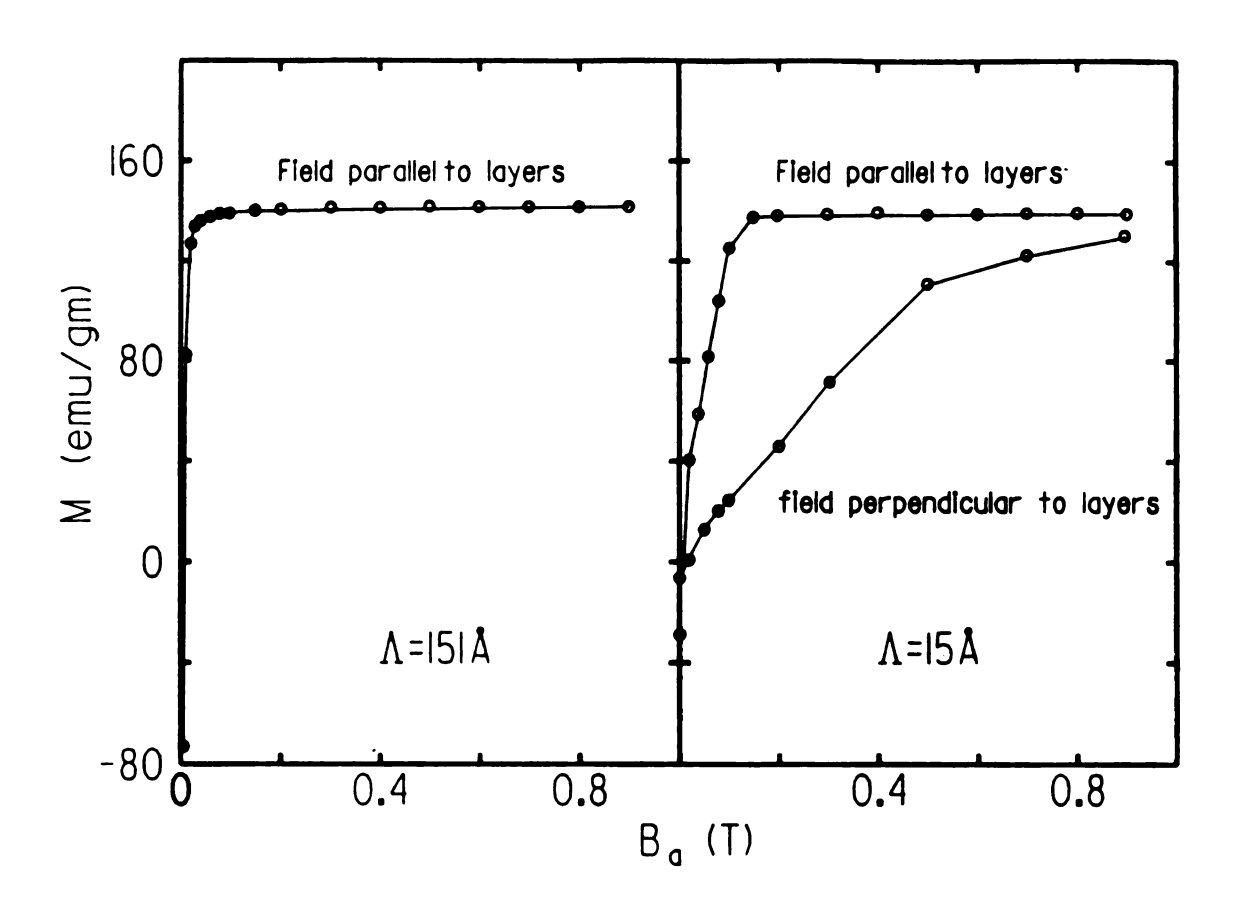


Figure 3.4 M versus  $B_a$  for Ag-Co LMS with  $\Lambda$ =15Å and  $\Lambda$ =151Å.

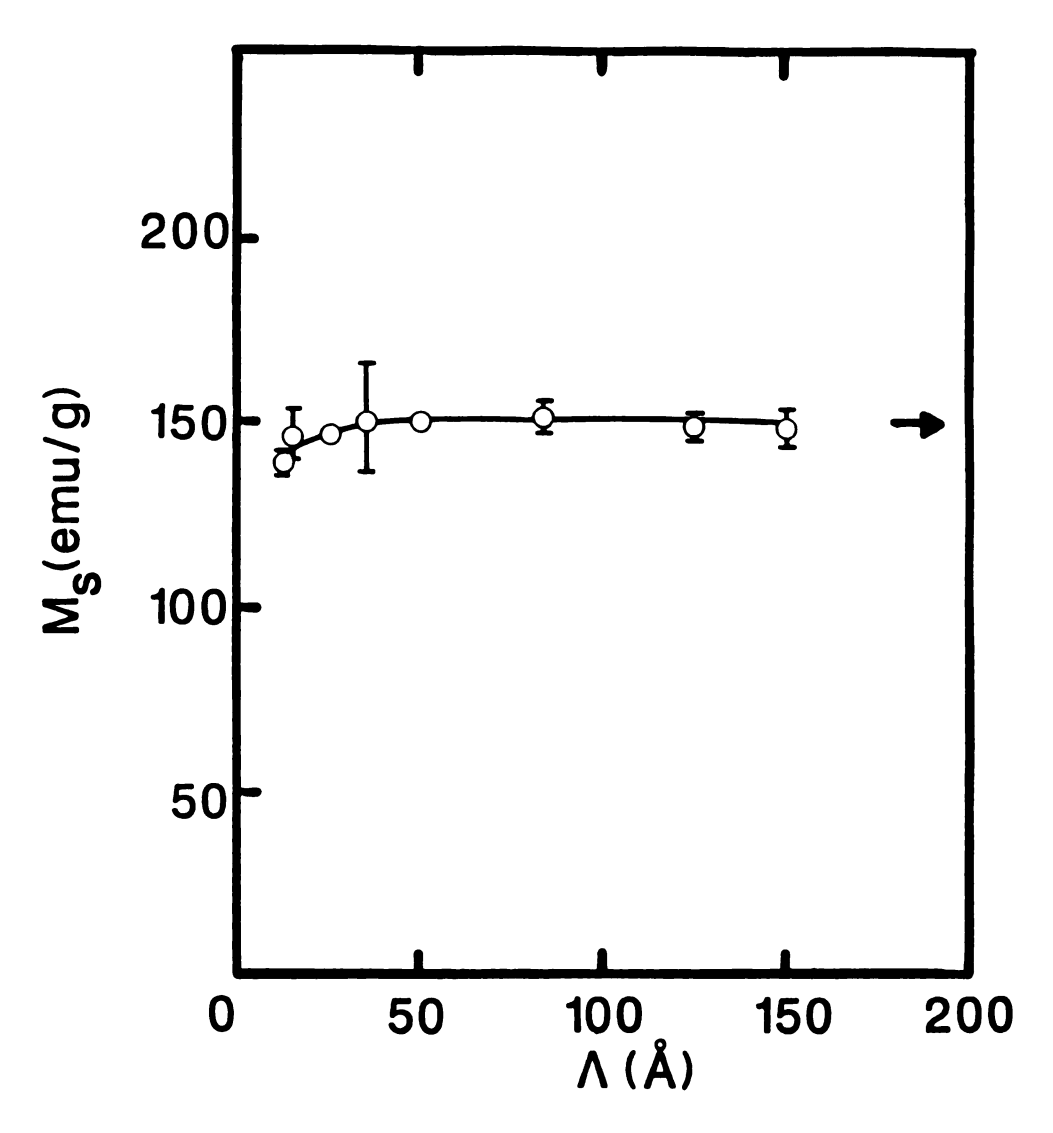


Figure 3.5  $M_s$  versus  $\Lambda$ . Arrow indicates  $M_s$  of a 5000 $\Lambda$  Co film.

## D. HALL EFFECT MEASUREMENTS

Hall effect measurements were made on the same samples used for  $\rho_{par}$  measurements using the same apparatus shown in Figure 2.4. In terms of the measured quantities, the Hall voltage  $V_H$  and the current I, the Hall resistivity, equation (3.10), becomes

$$\rho_{\rm H} = \frac{V_{\rm H}}{I} t \tag{3.13}$$

where t is the thickness of the film. As in the case of the  $\rho_{par}$  measurements, the current is reversed to cancel the effect of thermal emfs. If there is any offset in the positions of the Hall leads then the measured voltage will include an ohmic contribution associated with this offset. The field is reversed to cancel this contribution.

Plots of  $\rho_{\rm H}$  versus  $\rm B_a$  are shown in Figures 3.6 - 3.8. Figures 3.6 and 3.7 show the data for a pure Co film and a 40-40 LMS, respectively, at 4.2, 77 and 295K. Figure 3.8 shows 295K data for samples with  $\Lambda$ =16, 80 and 160Å.  $\rm B_s$  is determined by extrapolating the linear regions on either side of the kink until they intersect. The intersection point is the measured  $\rm B_s$ .  $\rm R_o$  is determined from the slope of the linear region above  $\rm B_s$  and the  $\rm B_a$ =0 intercept of the extrapolation of the same region gives  $\rm R_sM_s$ . Figure 3.9 shows  $\rm B_s$  plotted against  $\Lambda$ . Since the magnetization measurements show that  $\rm M_s$  is nearly independent of  $\Lambda$  for  $\Lambda$ 240Å, we infer that an interface anisotropy contribution is causing  $\rm B_s$  to be  $\Lambda$  dependent. Figure 3.10 shows  $\rm B_s$  versus 1/ $\Lambda$ . The data can be

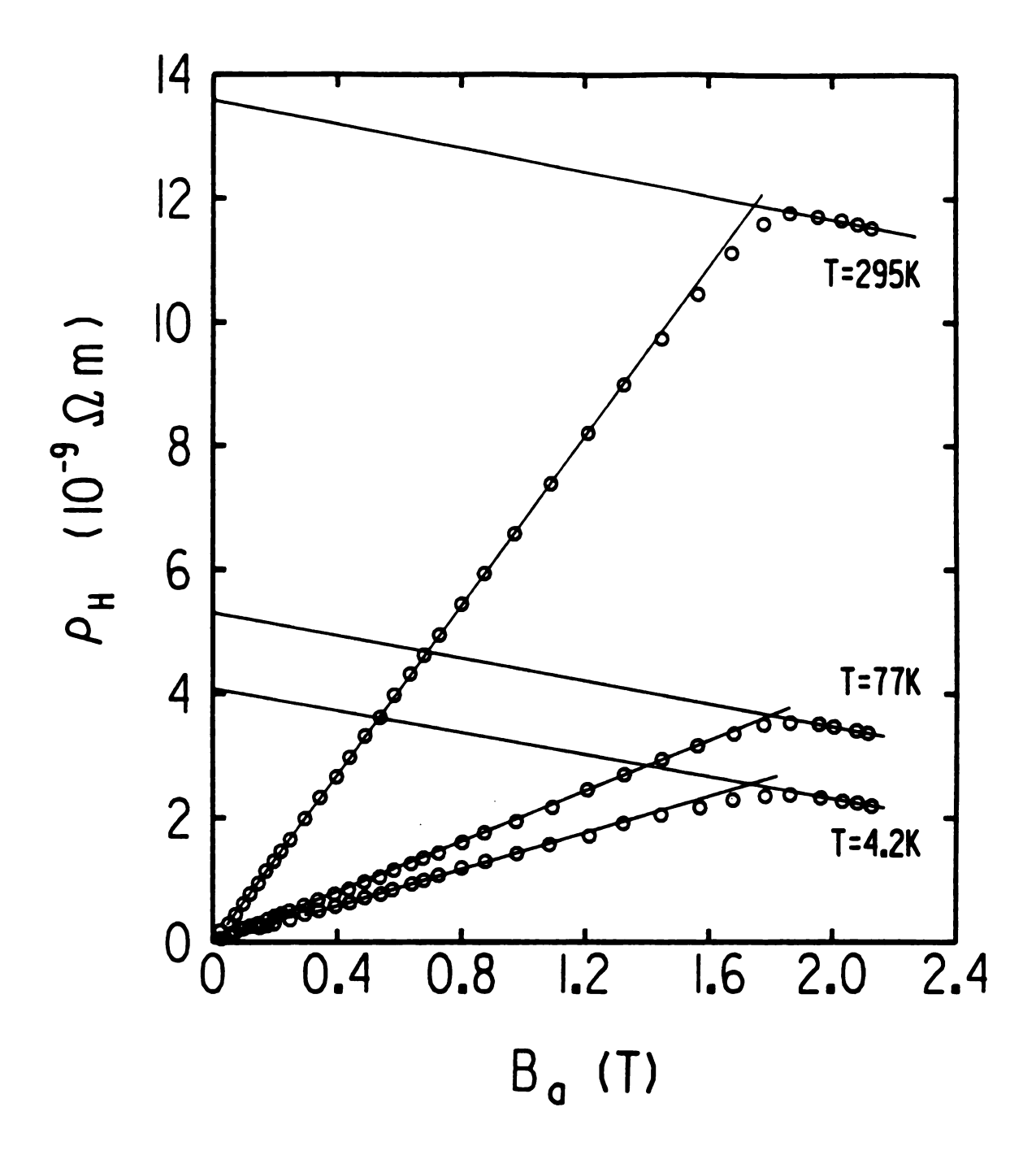


Figure 3.6  $\rho_{H}$  versus  $B_{a}$  for a 5000Å Co film.

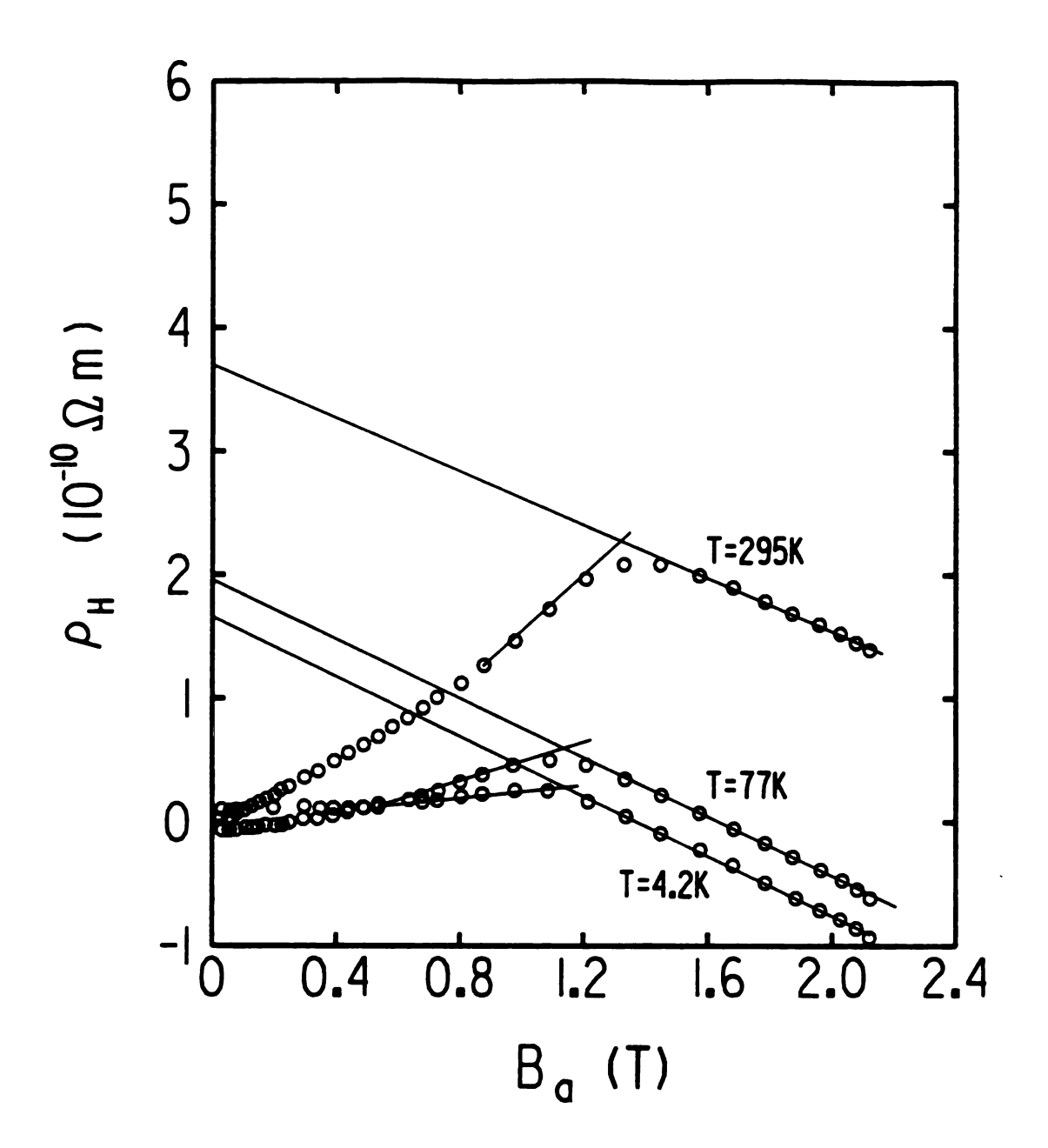


Figure 3.7  $\rho_{H}$  versus B for a  $\Lambda$ =80A Ag-Co LMS.

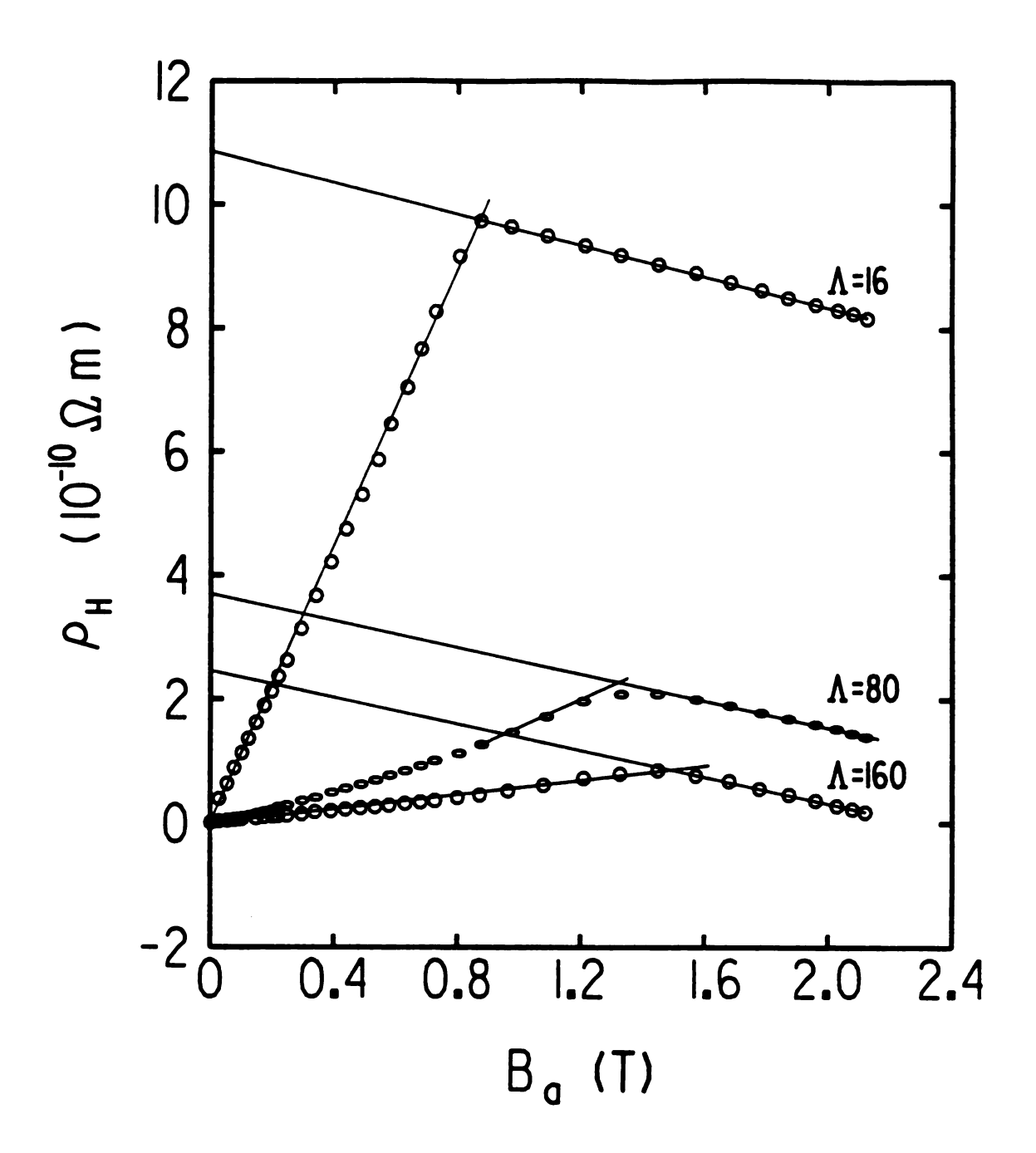


Figure 3.8  $~\rho_{\mbox{\scriptsize H}}$  versus  $\mbox{\scriptsize B}_{\mbox{\scriptsize a}}$  for  $\Lambda = 16,~80,~160\mbox{\scriptsize A}$  Ag-Co LMS at T=295K.

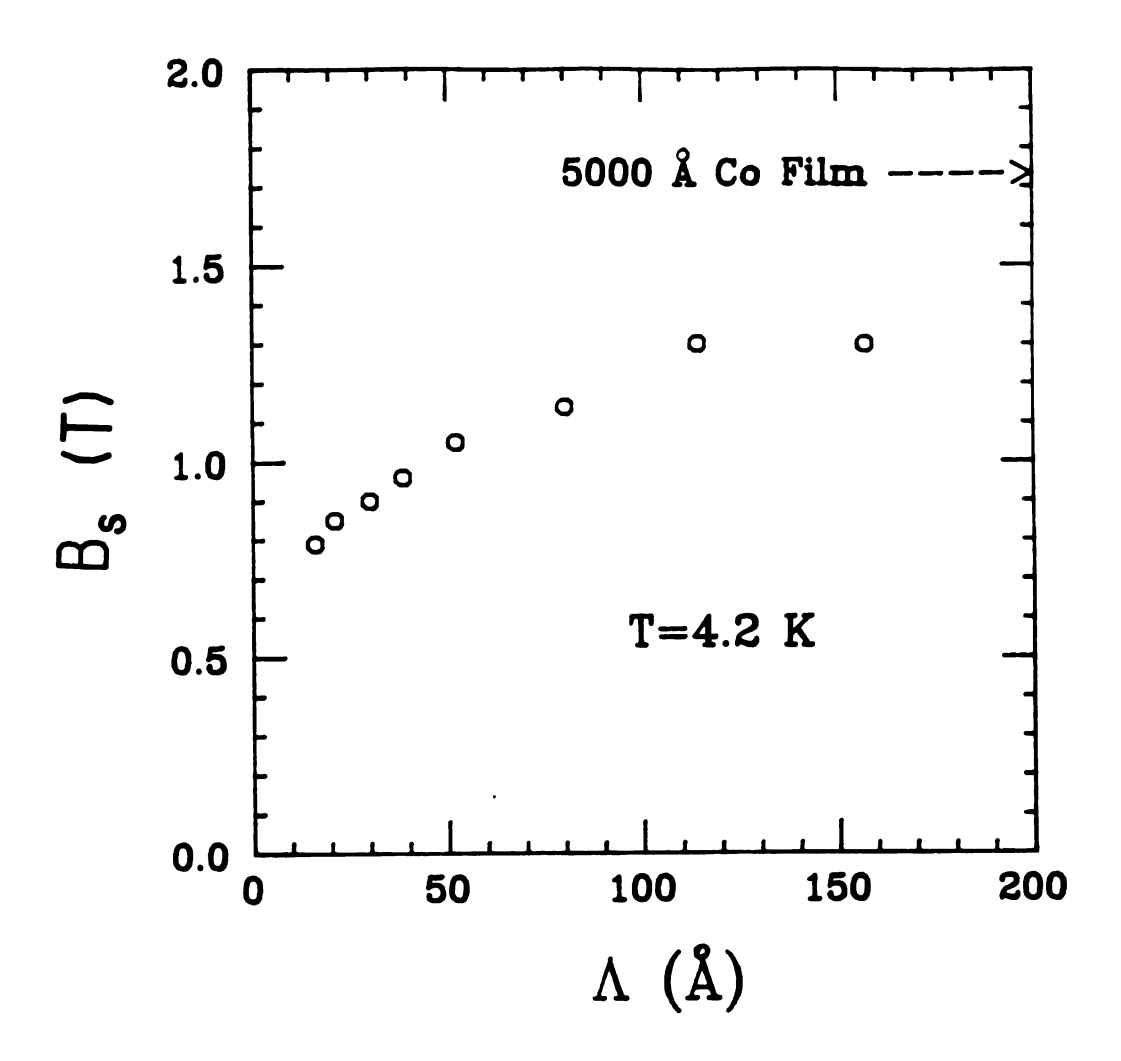


Figure 3.9  $B_s$  versus  $\Lambda$  at 4.2K.

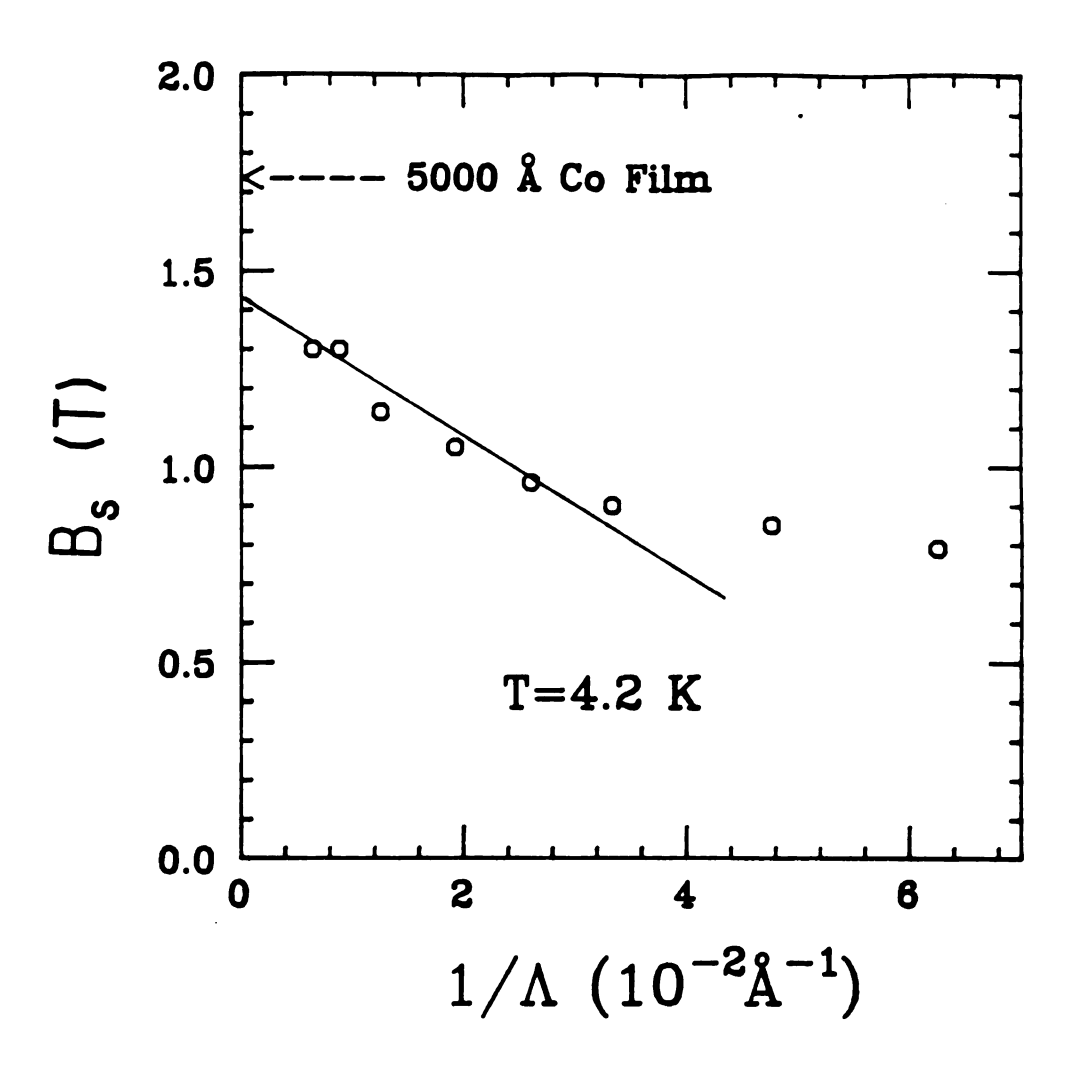


Figure 3.10 B<sub>s</sub> versus  $1/\Lambda$  at 4.2K.

fit to a straight line for A≥30Å yielding a value of approximately  $-2.7x10^{-4}$  J/m<sup>2</sup> for K<sub>s</sub> using equation (3.9). Note that, in the infinite  $\Lambda$  limit, the straight line does not extrapolate to the value of  $\mathbf{M}_{\mathbf{q}}$ determined from the Hall effect curve for a pure Co film indicating that  $K_{\nu}$  in equation (3.9) is not zero. The intercept yields a value of -2.8  $\mathrm{X}10^{5}$  J/m  $^{3}$  for  $\mathrm{K_{v}}$ . This value is a factor of 2 or 3 smaller than reported values of  $K_{ij}$  for Co crystals [Ki49, Su54]. The fact that  $K_{ij}<0$ indicates that the volume contribution to the energy is greater when the magnetization is in the plane. The sign of the anisotropy constants published for Co crystals is positive since for the crystal it is customary to define  $K_{\nu}$  to represent the energy difference between the hard and easy directions while here we have defined it to be the difference between the direction perpendicular to the film and parallel to the film. Even though the magnitude of  $K_{_{\rm tr}}$  is close to the value for single crystal Co and the sign is the same, it is unlikley that the  $K_{_{\mathbf{U}}}$ determined from Figure 3.10 is a manifestation of the same single crystal bulk anisotropy because  $H_{_{\mathbf{S}}}$  for the 5000Å Co film is not depressed. We expect that the Co is strained so it seems most likely that the shift is due to magnetostriction effects.

The flattening of the  $B_s$  versus  $1/\Lambda$  curve at small  $\Lambda$  could be due to structural (i.e. geometrical) effects. We know that the  $\Lambda$ =16Å sample is not made of continuous layers yet the data point for that sample fits smoothly into the curve implying that there may be a gradual deterioration of the layers with decreasing  $\Lambda$ . The magnetoresistance

data, described in the next section, also implies a gradual deterioration of the thin-film geometry of the Co layers.

Figures 3.11 and 3.12 show  $R_sM_s$  (determined from the  $\rho_H$  versus  $H_a$  curves) plotted against  $\rho_{par}^2$ . Since the SQUID magnetometer data show that  $M_s$  is nearly constant as a function of  $\Lambda$ , the nearly linear relationship shown in the figure implies that  $R_s \sim \rho^N$  where  $N \approx 2$ .  $N \approx 2$  implies that the scattering mechanism responsible for the anomalous Hall contribution is side-jump scattering. This result is in contrast to the work of Galepov [Ga73] who found N=1 for a single layer crystalline film of Co.

Takahashi et al. [Ta84] have previously measured  $M_S$  for Ag-Co multilayer films using a vibrating sample magnetometer (VSM) as well as by a ferromagnetic resonance (FMR) technique. Their conclusion was that  $M_S$  decreased continuously with  $d_{Co}$  with a large drop at  $d_{Co} \approx 8 \text{Å}$ . In fact, their values of  $M_S$  determined by FMR are in good agreement with our  $H_S$  values determined by the Hall effect. To determine  $M_S$  from the FMR measurements they used a comparison between measurements taken with the applied field parallel and perpendicular to the layers. Their measured values of  $M_S$  using the VSM with a parallel field are so scattered that they cannot be said to be in disagreement with our SQUID data or their interpretation of their FMR data. As a result we believe that the most reasonable conclusion is that the variation in  $H_S$  with  $\Lambda$  is due to a surface anisotropy rather than a variation of  $M_S$  with  $\Lambda$ .

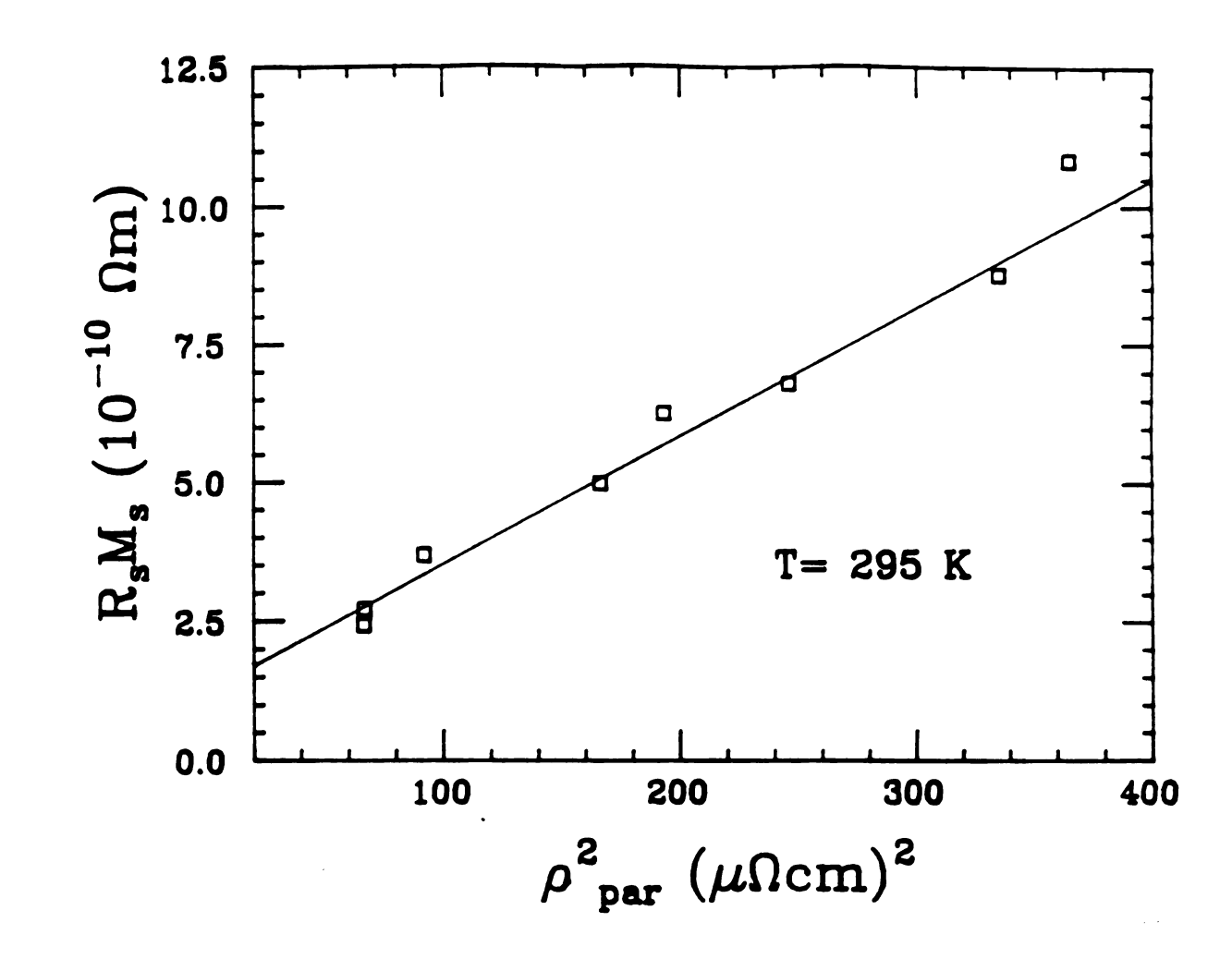


Figure 3.11  $R_s M_s$  versus  $\rho^2$  at T=295K.

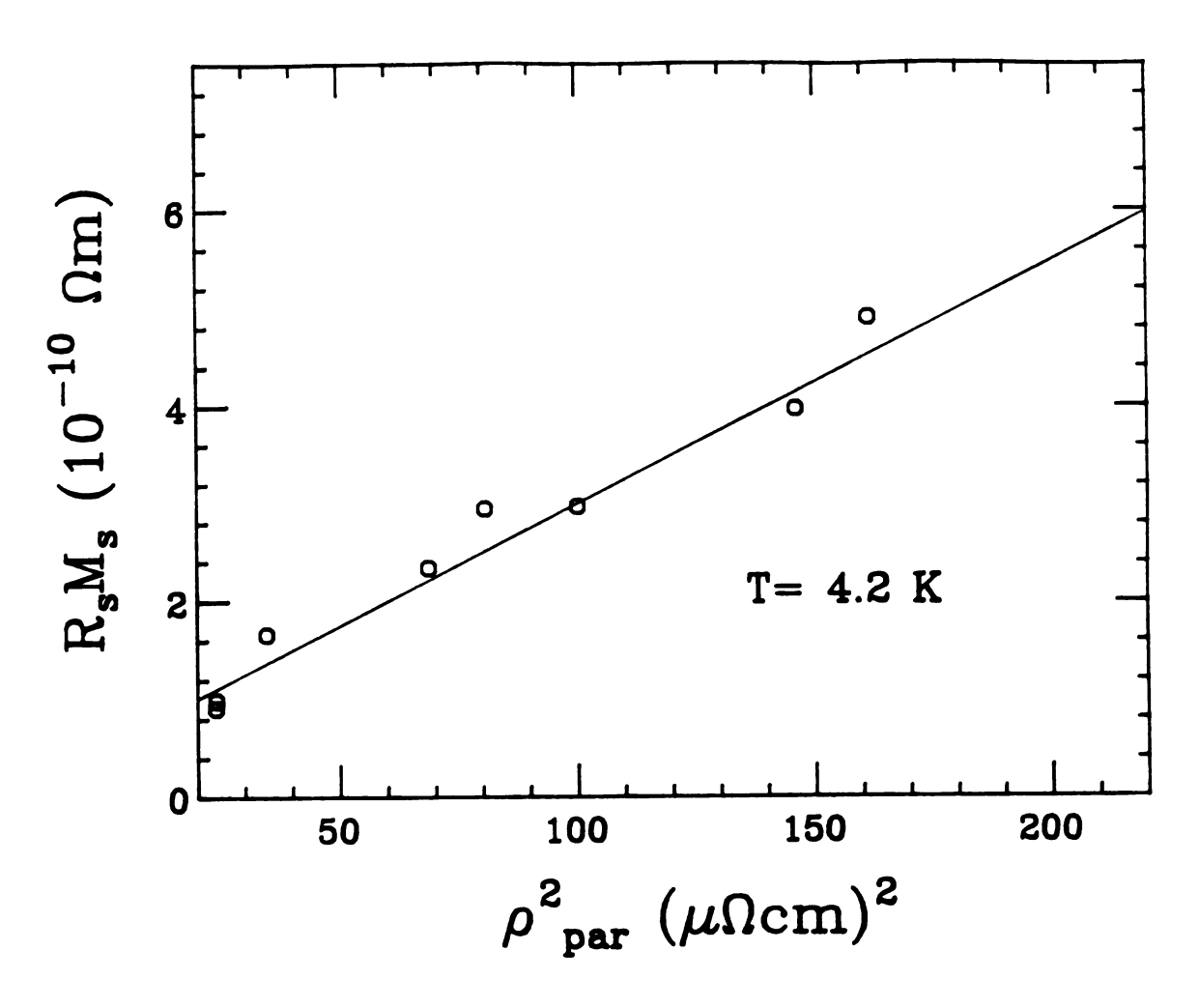


Figure 3.12  $R_{s}M_{s}$  versus  $\rho^{2}$  at T=4.2K.

Chappert et al. [Ch86] made magnetic measurements, using a SQUID magnetometer, of thin layers of Co ( $d_{Co} \le 25\text{Å}$ ) sandwiched between thick layers of Au with a (111) texture. Since Au is chemically and structurally similar to Ag we would expect to see some similarities in the behavior of the Ag-Co and the Au-Co system. They find that the easy axis rotates with increasing  $d_{Co}$  starting perpendicular to the layers and becoming parallel near  $d_{CO} = 18\text{\AA}$ . They interpret the rotation as being a signature of a surface anisotropy dominating other anisotropies in the small  $d_{CO}$  limit. It is interesting to note that if we extrapolate the linear region of Figure 3.10 to smaller A it crosses the  $H_g$ =0 axis at approximately  $\Lambda$ =13Å. The implication is that, if the high-A trend continued, there would be a rotation of the easy axis near  $\Lambda=13\text{\AA}$ . Assuming that the deviation from linearity is due to Co island formation or other structural defects in the Co layers, we would expect Ag-Co samples of the same structural quality as the Au-Co samples to show the rotation.

### E. MAGNETORESISTANCE MEASUREMENTS

Magnetoresistance measurements were made on the same samples used for  $\rho_{par}$  and Hall effect measurements using the same apparatus shown in Figure 2.4. The applied field was varied between zero and 2T and was rotated with respect to the sample through an angle  $\theta$  as defined in Figure 3.13. In this geometry the applied field  $B_a$  is always normal to

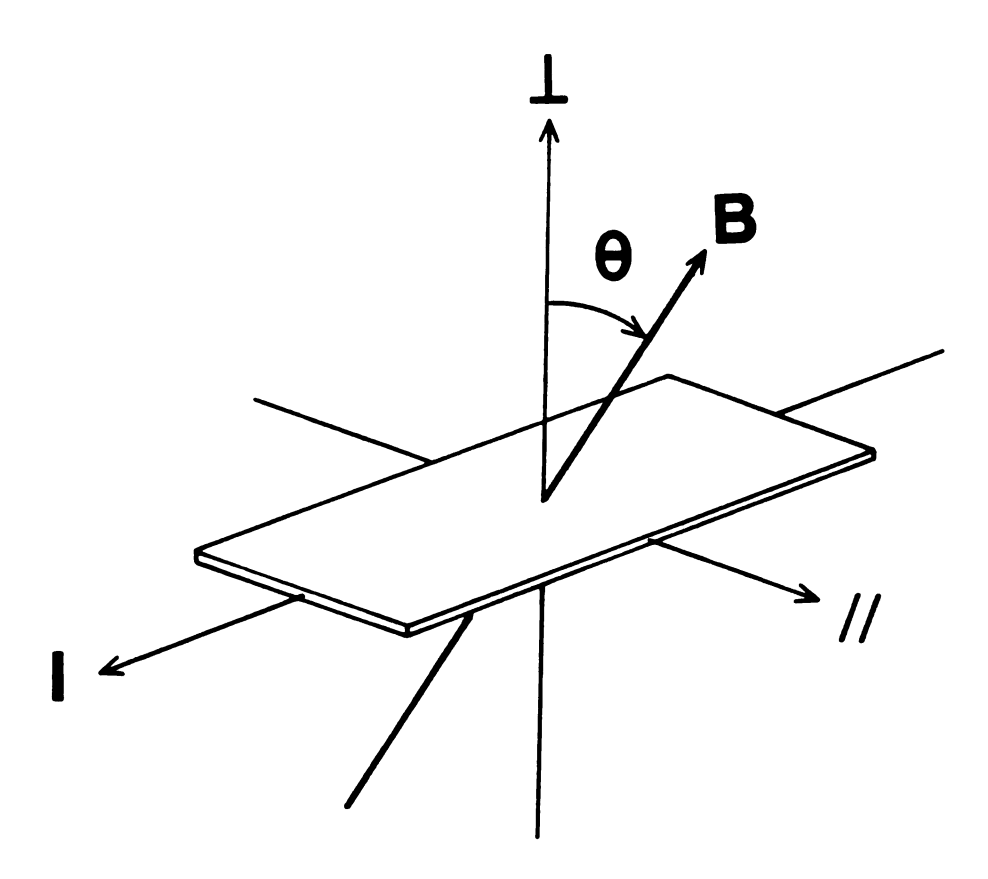


Figure 3.13 Magnetoresistance geometry.

the current but can have components parallel and perpendicular to the layers.

The magnetoresistance  $\rho(B_a)$  of a 5000Å thick pure Co film as a function of  $B_a$  is shown in Figure 3.14. When  $B_a$  is applied parallel to the surface the resistance quickly reaches a minimum and remains near that value as  $B_a$  is increased. In contrast, when  $B_a$  is perpendicular to the surface, the resistance increases and then decreases again at higher fields becoming nearly constant above the saturation field  $H_s$ . The perpendicular magnetoresistance shows some hysteresis for  $H_a < 0.7T$ .

The magnetoresistance of Ag-Co LMS show the same general behavior as the pure Co film. The magnitude of the change in the resistivity produced by the field varies but the features are always the same. The explanation for this behavior lies in the domain structure. Since the easy axis is in the plane of the film, even a small field applied in this direction can align the domains thus decreasing the disorder in the magnetic lattice and decreasing the resistivity. When the field is applied perpendicular to the layers, much greater fields are necessary to saturate the magnetization and align the moments of the domains perpendicular to the layers.

The angle dependence of the magnetoresistance at 0.5T is shown in Figure 3.15 for three LMS samples. A sharp peak is observed as the field is swept through the  $\theta$ =0 direction in all cases. The origin of this peak is again the large anisotropy due to the demagnetizing factor. Except for the exact perpendicular direction, there is a field component parallel to the layers, so that the domains can be easily aligned in

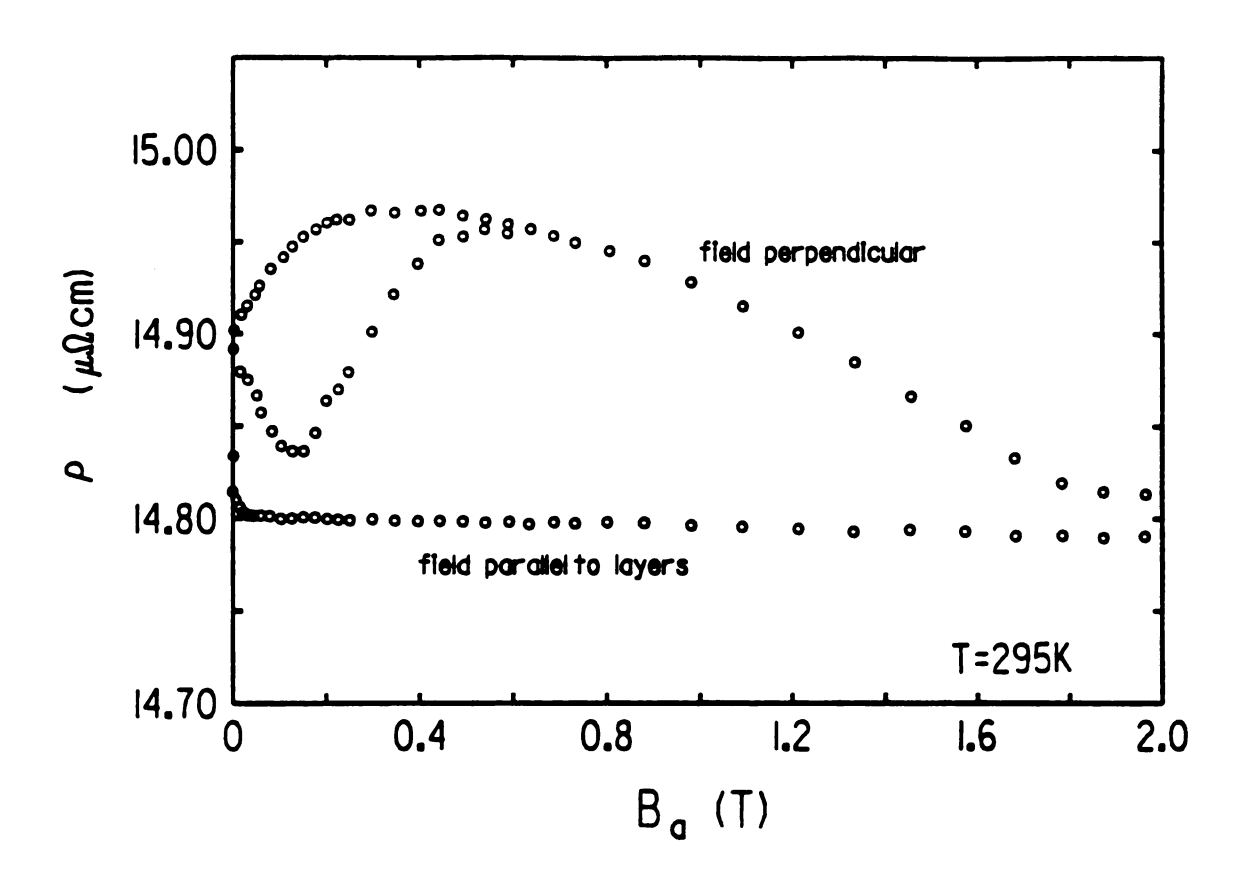


Figure 3.14  $\rho$  versus  $B_a$  for a 5000A Co film.

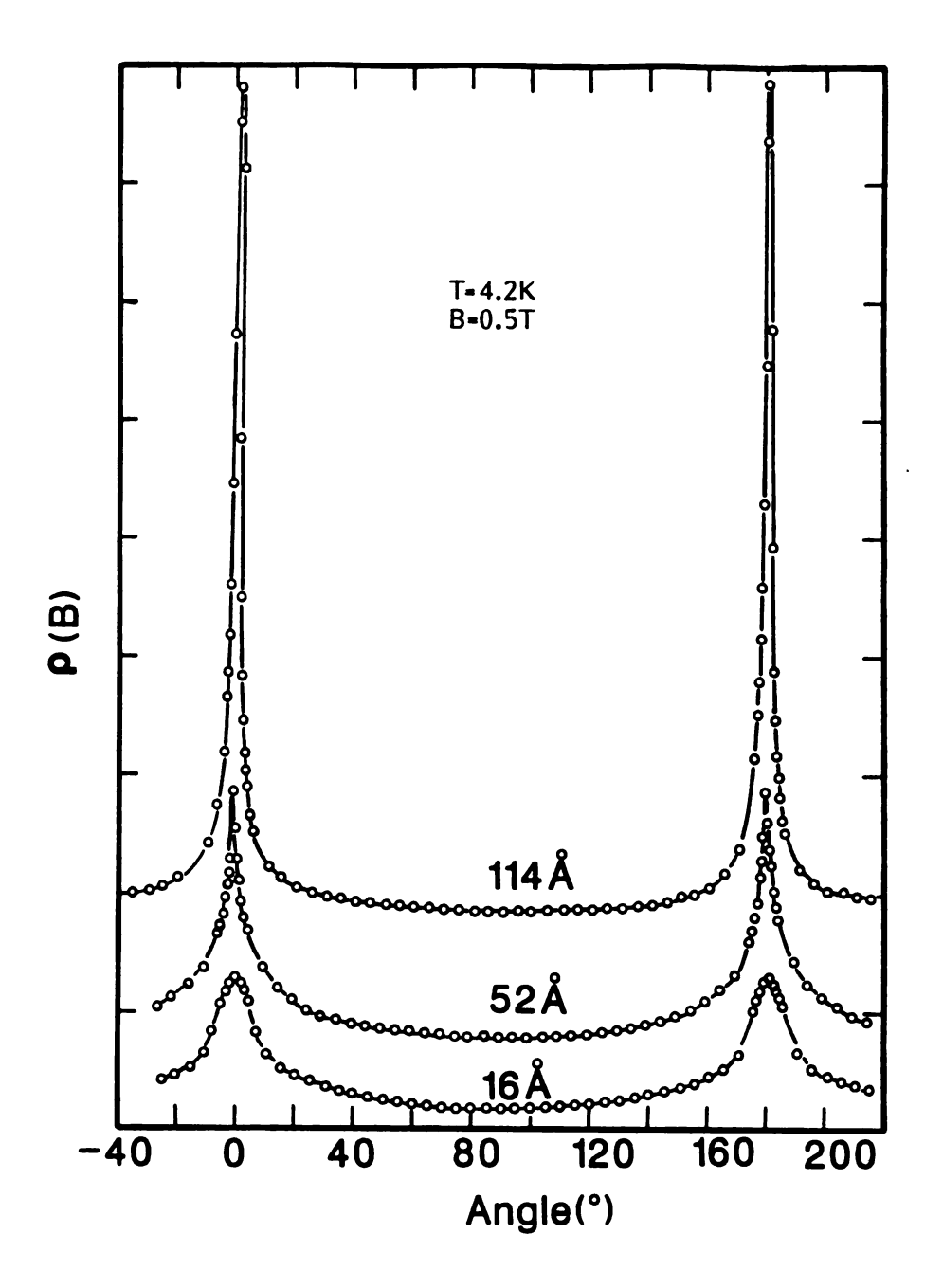


Figure 3.15  $\theta$  dependence of magnetoresistance for three Ag-Co LMS.

that direction. Only very near the  $\theta$ =0 direction is this component too small to align them and the quasi-randomly oriented domains cause the increase in resistance. These peaks have several interesting features.

- 1. The width at 4.2K increases with decreasing  $\Lambda$ . It roughly correlates with the half-width of the X-ray diffraction peaks and therefore with the quality of the multilayers. Since the sharp peaks are the result of the thin-film shape anisotropy, the increasing width may be indicative of a slow degredation of the thin-film geometry of the Co layers with decreasing  $\Lambda$ .
- 2. With increasing  $\Lambda$  (up to 200Å) the rotational hysteresis (the shift of the peak position when the direction of change of  $\theta$  is reversed) increases; e.g. for  $\Lambda=14\text{\AA}$ ,  $\Delta\theta=0.5^{\circ}$  and for  $\Lambda=200\text{\AA}$ ,  $\Delta\theta=8^{\circ}$ .
- 3. The amplitude of the anisotropy defined as  $\Delta \rho = \rho(\theta=0) \rho(\theta=90^{\circ})$  changes smoothly with  $\Lambda$  as indicated in Figure 3.16 with a maximum at  $\Lambda \approx 120 \text{\AA}$ . In the same figure we show that over the same range of  $\Lambda$  the zero field resistivity continuously decreases with increasing  $\Lambda$ . For  $\Lambda < 40 \text{\AA}$ ,  $\Delta \rho$  is very close to that measured for a 5000 \text{Å} thick Co film. In the large  $\Lambda$  limit we can assume that we have a parallel combination of independent resistors. Then we can estimate  $\Delta \rho$  from the measured resistivity and  $\Delta \rho$  of the thick pure metal samples. This estimate is shown as an open square near the right-hand ordinate of the figure. Between these two limits  $\Delta \rho$  shows a temperature dependent maximum which cannot be explained by an independent resistor model since for a pure Co film,  $\Delta \rho$  decreases with decreasing T but near the maximum  $\Delta \rho$  increases with decreasing T.

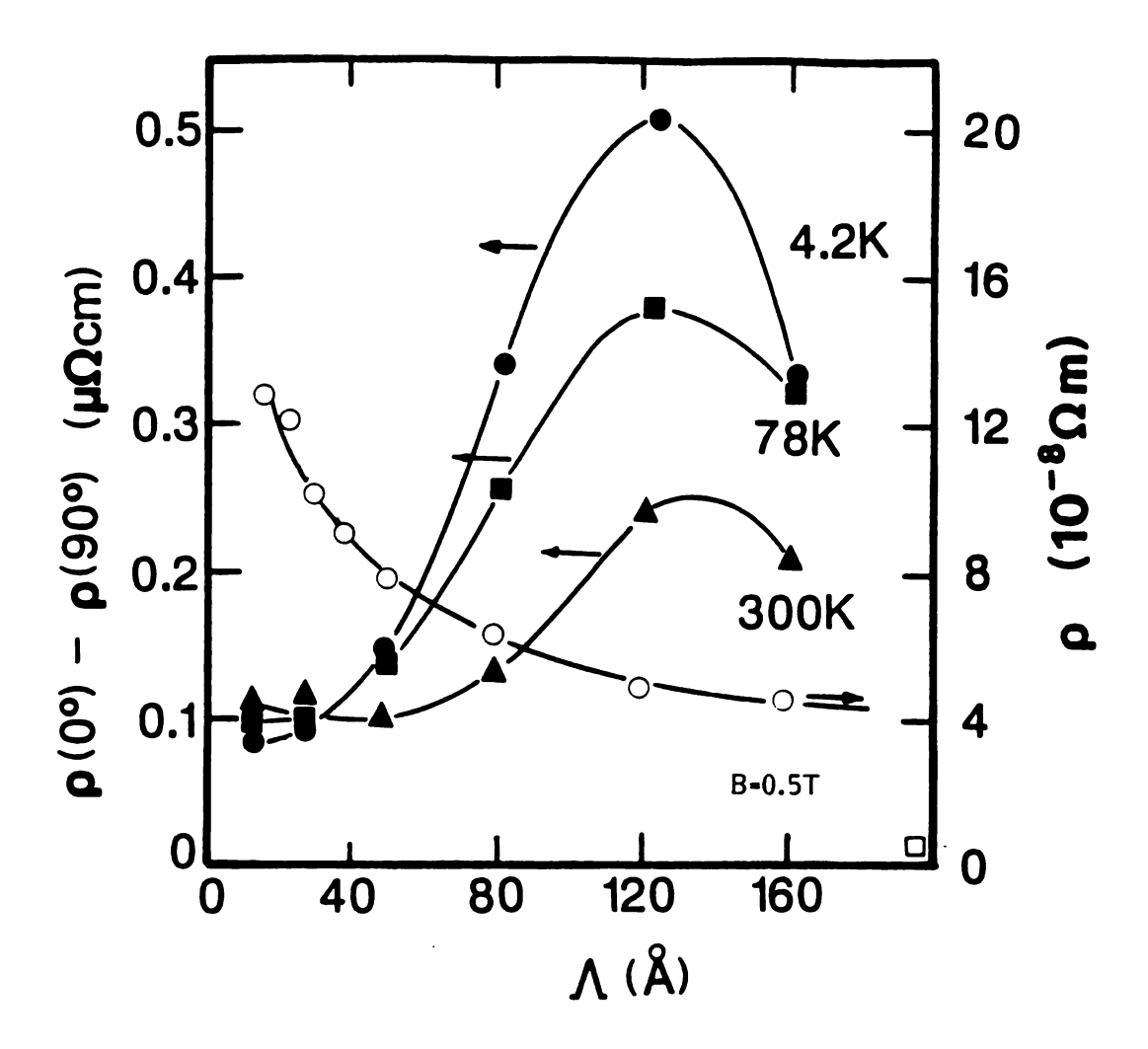


Figure 3.16 Magnetoresistance anisotropy and  $\rho_{\mbox{\scriptsize par}}$  versus  $\Lambda.$ 

### CHAPTER 4

## SUMMARY, CONCLUSIONS AND RECOMMENDATIONS

### A. SUMMARY AND CONCLUSIONS

Ag-Co LMS with  $\Lambda \ge 21 \text{\AA}$  have been produced by sputter deposition on substrates near room temperature. The quality of the layers decreases rapidly with increasing substrate temperature. The coherence length perpendicular to the layers, determined from the widths of the X-ray diffraction peaks, varies from ~100 Å to ~200 Å as  $\Lambda$  varies from 21 Å to 160 Å.

Step-model calculations of  $\theta$ -20 X-ray diffraction spectra reproduce the behavior of the experimental spectra, however, the spectra calculated using hcp-Co layers are so similar to those using fcc-Co that neither structure can be ruled out. The calculations using bcc-Co do not fit the experimental spectra well for  $\Lambda \geq 38.5 \text{\AA}$ .

The resistivity parallel to the layers was measured at 295, 77, and 4.2K and found to be lower than any other LMS studied to date. We estimate that  $\ell_{eff}$ , in Ag-Co LMS, is greater than an individual layer thickness for all of the samples measured (16Å  $\leq \Lambda \leq$  160Å) and is up to 5 layer thicknesses in some samples at 4.2K. The  $\Lambda$  dependence of  $\rho_{par}$  can be fit by a modified Fuchs-Sondheimer model with one free paramter; the probability of specular transmission/reflection t/p. Electrons not specularly transmitted/reflected are diffusely scattered. The best fit to the experimental data is obtained with the transmission model for t=0.55 at T=295K and t=0.63 at T=77 and 4.2K. The best fit obtained

with the reflection model is nearly as good with  $0.45 \le p \le 0.50$  over the same temperature range.

The first measurements of  $\rho_{perp}$  have been made on a LMS. A comparison of the  $\rho_{perp}$  data to a simple free-electron model similar to that used in the parallel case implies that transmission at the interfaces dominates reflection. Thus, considering the results of the fitting to the  $\rho_{par}$  data, we conclude that ~1/2 of the electrons encountering an interface are diffusely scattered and the majority of those not diffusely scattered are transmitted. The scatter in  $\rho_{perp}$  is larger in the LMS data than in the pure film or sandwich data. Structural differences in the samples and/or band structure effects may contribute to this scatter.

The perpendicular measurements made on sandwiches composed of Ag with thin layers of Co near the SN interfaces have shown that a 25Å layer of Co completely inhibits the superconducting proximity effect. A sandwich sample with the same amount of Co, deposited on a hot (~80°C) substrate, becomes superconducting by proximity effect implying that the Co layers in that sample are not continuous.

Magnetization measurements made in a SQUID magnetometer with the field applied parallel to the layers have shown that  $M_S$ , of the Co layers, is nearly independent of  $\Lambda$  and equal to the bulk Co value. There is an indication of a small drop in  $M_S$  for a sample with  $\Lambda \approx 13 \text{\AA}$ .

Hall effect measurements made with the field applied perpendicular to both the current and the layers show that the saturation field decreases with decreasing  $\Lambda$ . Since  $M_S$  is nearly constant with  $\Lambda$ , the

behavior of  $B_S$  indicates the presence of a uniaxial anisotropy, other than the expected shape anisotropy, which depends upon the thickness of the Co layers. The large- $\Lambda$  data were fit to the surface anisotropy theory of Koepke and Bergmann (KB) yielding a surface anisotropy energy density  $K_S = -2.7 \times 10^{-4} \text{ J/m}^2$ . In the KB theory, a plot of  $B_S$  versus  $1/\Lambda$  should be linear (if  $M_S$  is constant) but our data show some curvature. The contribution to the anisotropy which is responsible for the curvature is unknown but structural differences in the samples, including magnetostriction effects due to straining of the Co by the Ag lattice, may be responsible.

The dependence of the spontaneous Hall coefficient on  $\rho_{par}$  is of the usual form,  $R_S^{}\sim \rho^N$ , where N has been found to be ~2 implying that side-jump scattering contributes to the anomalous part of the Hall effect in Ag-Co LMS.

The width of the peaks in the magnetoresistance versus field-direction curves increases continuously with decreasing  $\Lambda$ . Since the sharp magnetoresistance peaks are the result of the thin film shape anisotropy, this result may be indicative of a slow degradation of the thin film geometry of the Co layers with decreasing  $\Lambda$ . The magnetoresistance anisotropy,  $\rho(0^{\circ}) - \rho(90^{\circ})$ , shows a temperature dependent maximum near 120Å which cannot be explained by a simple model of the layers as resistors in parallel.

It is interesting that many of the properties of Ag-Co LMS seem to change their behavior near  $\Lambda=100\,\text{Å}$ . The most noteworthy examples are the following.

- 1. The best fit to the step model of X-ray diffraction changes from hcp to fcc between  $\Lambda=114\mbox{\normalfont\AA}$  and  $\Lambda=80\mbox{\normalfont\AA}$ .
- 2. The  $\rho_{perp}$  data are most scattered near  $\dot{\Lambda}=80\, \mathring{A}$  and the  $\rho_{perp}$  versus 1/A curve (Figure 2.14) seems to have a change of slope near there.
- 3. The curvature in the B<sub>s</sub> versus  $1/\Lambda$  curve (Figure 3.10) could be interpreted as a somewhat gradual change of slope near  $\Lambda=100\text{\AA}$ .
- 4. The magnetoresistance anisotropy goes through a temperature dependent maximum near  $\Lambda=120\mbox{\normalfont\AA}$ .

One possible explanation of these effects is a change in the Co structure as a function of  $\Lambda$ . We suspect that the Co layers are the source since the Co dominates the galvanomagnetic properties of the LMS and, since it has a much higher resistivity that Ag, it plays a more important role in determining  $\rho_{perp}$  than it does for  $\rho_{par}$ .

The X-ray result suggests the following speculation. Suppose the thick layers of Co are mostly hcp with a small fcc component. Further suppose that as the layer thickness decreases the fcc component grows at the expense of the hcp component. It is natural to expect that the exact composition, in the region of  $\Lambda$  where the transition is occurring, would be very sensitive to the conditions during sample preparation so that it would vary from sample to sample. Since hcp-Co has an anisotropic resistivity and the samples are textured, the variations in the composition of the Co layers could contribute to the scatter in  $\rho_{\text{perp}}$ . The mixed phase might also affect the scattering of the electrons in the Co layers and thus affect the galvanomagnetic properties. The galvanomagnetic data vary smoothly with  $\Lambda$  as opposed

to being scattered like the  $\rho_{perp}$  data but this may be due to the fact that the samples used for the galvanomagnetic measurements were produced in the same run under almost identical conditions whereas the  $\rho_{perp}$  samples were produced in many different runs.

There is some evidence against the above speculation. The Ag-Ni LMS has a temperature dependent maximum in  $\Delta\rho$  which is very similar to that in Ag-Co [Sa87]. It is unlikely that this peak is due to a structural phase transition since Ni, like Ag, is fcc. Perhaps the origin of the peak in  $\Delta\rho$ , in both Ag-Co and Ag-Ni, is related to domain structure rather than crystal structure.

### B. RECOMMENDATIONS

In the future, there is much related work which could be done.

- 1. The perpendicular resistivity measurements should be extended to other LMS. Ag-Ni is an interesting system which has many similarities to Ag-Co and some important differences.
  - a. Like Ag and Co, Ag and Ni are mutually insoulble.
  - b. Ag and Ni form a coherent LMS with  $\rho_{par}$  lower than most, although slightly higher than Ag-Co. The coherence length as a function of  $\Lambda$  and the effect of the substrate temperature on the layered structure are very similar to those for Ag-Co.
  - c. The magnetic and transport properties of Ni are more isotropic, due to its fcc structure. In addition, there is no evidence that the Ni in Ag-Ni LMS has any non-fcc component. If the scatter in

the Ag-Co  $\rho_{\mbox{\footnotesize{perp}}}$  data is due to structural changes then the scatter in Ag-Ni should be much less.

- d. Ni is ferromagnetic but may have nonferromagnetic or "dead" layers at surfaces.
- e. Ni has a spin assymetry in its conduction band: the spin-up band has higher conductivity than spin-down. The spin polarization of the electrons coming from Ni into Ag may result in an effective interface resistance at each Ni-Ag interface [va87].

Preliminary  $\rho_{\mbox{\scriptsize perp}}$  measurements on Ni-Ag are presently underway.

- 2. Ultra-low temperature (0.010K  $\leq$  T  $\leq$  4K) measurements in the perpendicular geometry should be made with the same SQUID circuit (shown in Figure 2.9) and one of the dilution refrigerators available in this department. The temperature dependence can be measured with a precision of 1 part in  $10^7$  using this system. Preliminary measurements indicate that there may be a significant contribution to the temperature dependence from the SN interfaces which depends upon whether there is Co in direct contact with the Nb or Ag. The effect of the SN interface must be studied further to determine the viability of the perpendicular technique for studying temperature dependences.
- 3. More sophisticated characterization of the samples is needed for a more detailed analysis of the Ag-Co data. Electron diffraction and cross-sectional TEM experiments in the department's Analytical Electron Microscope Laboratory may shed some light on the Co structure and better characterize the geometry of the layers.
- 4. The size effect in Co films should be studied to determine the correct value of  $\rho_u \hat{\iota}$ . Our ability and experience in making high quality

Co films for resistivity measurements puts us in the best position for filling this gap in the literature.

5. There are some theoretical problems which deserve consideration. A theory for  $\rho_{perp}$  which treats transmission correctly would be useful. Band structure calculations for Ag-Co and Ag-Ni might also help in understanding the perpendicular resistivity measurements.

## APPENDIX A

#### READING POWER SUPPLY PARAMETERS

The L.M. Simard TS/2 target power supplies are capable of supplying target voltages  $V_T$  up to (-)1000V at currents up to 2A. The TS/2 is a constant voltage supply. The target current  $I_T$  is adjusted by increasing or decreasing the plasma density above the supttering target. In practice the plasma density (and therefore  $I_T$ ) is determined by the plasma current  $I_P$  supplied by the PD/20 OR PD/200 plasma power supply. Increasing  $I_P$  will increase  $I_T$ .

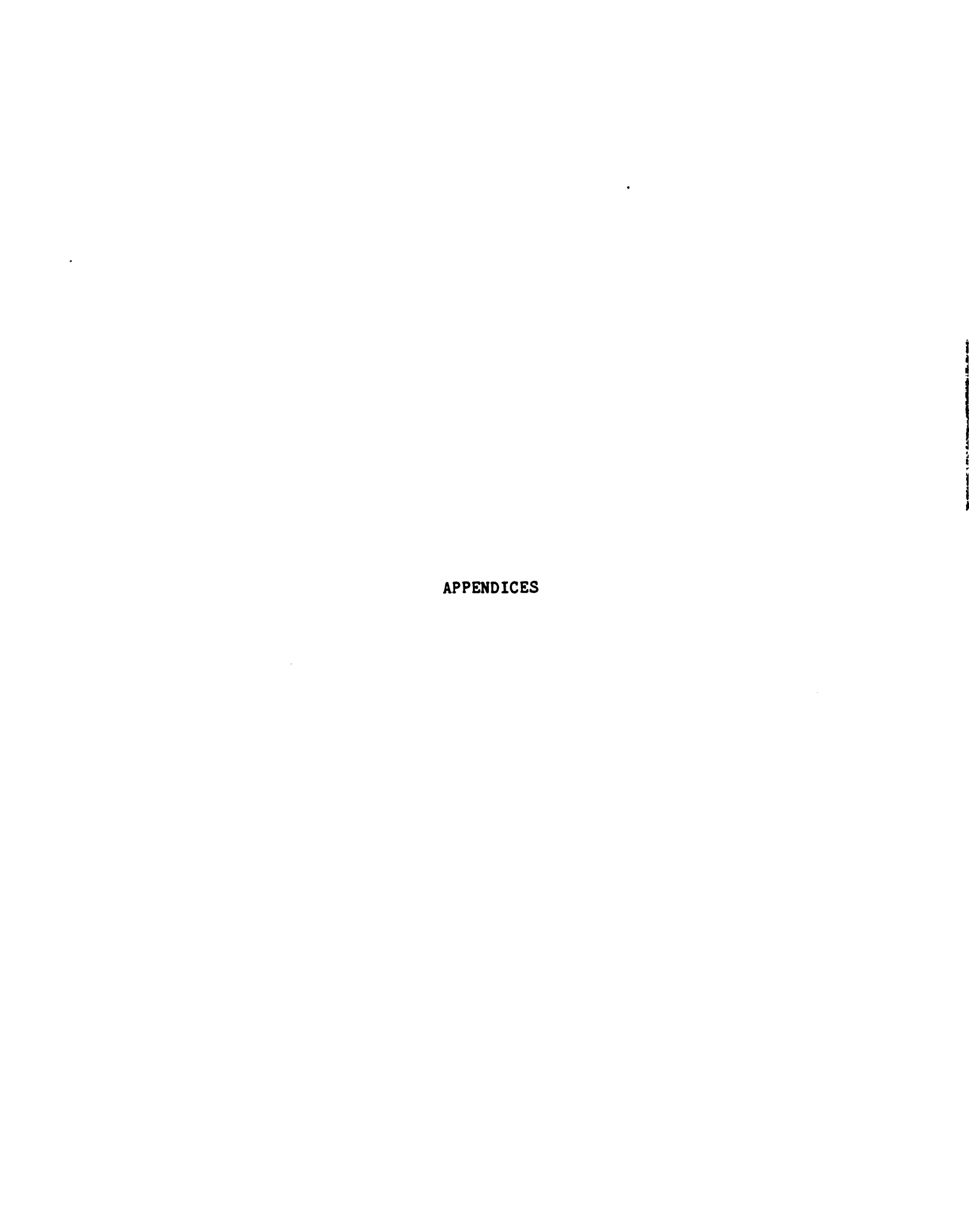
In order to hold the sputtering rate constant, the target supply parameters must be held constant. The first step toward this goal is to monitor  $I_T$  and  $V_T$ . The second step is to have the computer feed back to the plasma supply to control  $I_p$  and therefore also control  $I_T$ .

The TS/2s have low voltage outputs,  $v_t$  and  $i_t$ , which are proportional to  $V_T$  and  $I_T$  respectively. The relationships between the low voltage outputs and the actual power supply parameters are

$$v_{t}[V] = 0.01 V_{T}[V]$$
 (I.1)

$$i_{t}[V] = 5 I_{T}[A].$$
 (I.2)

The computer reads  $v_t$  and  $i_t$  using an analog-to-digital converter (ADC) and uses them to calculate  $V_T$  and  $I_T$ .



The Data Translation DT2801 ADC/DAC board is described in Chapter 1. A subroutine package by Data Translation (PCLAB) is used to communicate with the board via CALLable subroutines which are contained in a library and linked with the compiled programs. The ADC returns a number called the analog data value (ADV) which is in the range  $0 \ge \text{ADV} \ge 4095$ . The input range of the ADCs is set at -10V to +10V to accommodate  $\mathbf{v}_{\mathbf{t}}$  and  $\mathbf{i}_{\mathbf{t}}$ . Thus, the relationship between the input voltage to ADC channel i,  $\mathbf{v}_{\mathbf{i}}$ , and its corresponding ADV, ADV(i), is

$$v_i [V] = 20(ADV(i) / 4096) - 10.$$
 (I.3)

Using equations (I.1) - (I.3), a computer program can calculate  $V_T$  and  $I_T$  from the ADVs. The only complication is that there is a large 120Hz ripple superimposed on  $V_T$  and  $I_T$  so that a single reading would have a large uncertainty. An average of 500 readings taken over a period of 0.333s reduces the uncertainty to ~0.3%.

Below is a listing of the source code for the subroutine TARADC (see Chapter 1, page 16). TARADC, like all of the control software, is written for the Microsoft [MIC] QuickBASIC compiler. The subroutines SETUP.ADC, BEGIN.ADC.DMA, WAIT.ADC.DMA and SET.CLOCK.DIVIDER are part of the PCLAB library. The ADC channel assignments are defined in Figure 1.6. The ADVs are read into the computer memory through a direct memory access (DMA) channel, meaning that the program continues to run while the ADVs are read directly into memory.

SUB TARADC ( GUN%, V.AVE, I.AVE ) STATIC

<sup>&#</sup>x27; reads target supply parameters

<sup>&#</sup>x27; J Slaughter 6-4-86 10-7-86 4-7-87

<sup>&#</sup>x27; clock is set w/ SET.CLOCK.DIVIDER(TICKS%) by main program

<sup>&#</sup>x27; ticks = 133 => 500 X 2 points in 1/3 s

```
' samples are taken alternately from V.CHAN% & I.CHAN%
' GUN$ = 0 => gunA : chan 0 & 1
         1 => gunB : .... 2 . 3
        2 => gunC : .... 4 . 5
         3 => gunD : chan 6 & 7
' V.CHAN' = channel number to read target voltage from
' I.CHAN% = . . . . . . . . . . . current .
' V.AVE = calculated target voltage
' I.AVE = calculated target current
' SUMO = sum of V.CHAN% ADVs
' SUM1 = sum of I.CHAN% ADVs
' nper = number of points to read from each channel - for average
' ADV%(i) = array to conatin ADVs read from both channels
DIM ADV%(1000)
nper = 500
N.WAIT%=50
            ' see below
V.CHAN% = GUN% * 2
I.CHAN\% = V.CHAN\% + 1
TIME.SOURCE%=0 ' see below
GAINS=1
               ' see below
                       ' see below
NO. VALUES = nper # 2
CALL SETUP.ADC(TIME.SOURCE%, V.CHAN%, I.CHAN%, GAIN%)
   this subroutine sets up ADC to read sequentially from channel
   V.CHAN% to I.CHAN%.
   TIME.SOURCE = 0 => use internal DT2801 clock to set frequency
   of sampling. Clock previously set up by SET.CLOCK.DIVIDER.
   GAIN% = 1 => use input voltage range as set by hardware '
switches. i.e. ±10V.
SUMO=0
SUM1=0
CALL BEGIN.ADC.DMA(NO.VALUES, ADV, (0))
   This subroutine begins the reading of the ADVs directly into
   memory as specified by SETUP.ADC.
    Puts numbers into the array ADV$() starting with ADV$(0).
   NO. VALUES; is the number of samples (ADVs) taken.
CALL WAIT.ADC.DMA(ADV%(N.WAIT%))
   This subroutine stops execution of the program until the first
   N.WAIT% values are read. Insures that program does not try to
   calculate averages using elements of ADV%() which have not been
   defined yet.
' calculate averages and convert adv's to actual values
FOR I%=0 TO (NO.VALUES%-2) STEP 2
   SUMO=SUMO + ADV%(I%)
   SUM1=SUM1 + ADV%(I%+1)
NEXT IS
V.AVE = (SUMO / (NPER * 4096)) * 2000 - 1000
I.AVE = (SUM1 / (NPER * 4096)) * 4 - 2
```

#### END SUB

At present, the values returned by TARADC are displayed on the screen during sample production along with the values read when the deposition rates were measured (as a reference). The operator must occasionally adjust the power supplies to keep the production parameters equal to the reference values.

There are two practical problems one must keep in mind when using TARADC.

- 1. As the SPAMA disk moves there are often fluctuations in the target parameters. These fluctuations occur when the open holes in the disk (for the FTMs) pass over a sputtering source. The presence of a hole briefly changes the local pressure over the source and thus the plasma density. If the target supply parameters are being read when such a fluctuation occurs, the reading will not reflect the true value of the parameters when the substrate is over the gun. To avoid this problem, the control programs, FILM and CMS, only call TARADC to monitor a source when the substrate is stopped over that source. This procedure eliminates the problem of reading spurious parameters but it makes the second problem more serious.
- 2. It takes ~1.1s for the computer to calculate  $V_T$  and  $I_T$  since there are 1000 numbers to be averaged. If a sample is being made which requires a time delay over a source to be <1.1s (i.e. a sample with thin layers or high deposition rates), the parameters cannot be monitored for every layer. The easiest solution to this problem is probably a software solution: make the software read the supplies only every second or third cycle if necessary. The only difficulty lies in the

fact that the PC21 indexer is programmed to send carriage return characters to signal the beginning of a new layer. If the signal is missed because the computer is busy calculating averages then the control program and the indexer/motor will be out of synchronization. The motor will finish the last sequence it was programed for but the computer will be stuck in an endless loop waiting for more carriage returns. This signalling problem can be avoided by checking for the signal in the loop that calculates the sums in TARADC but this will, of course, increase the amount of time needed by TARADC. Although such a change is not difficult, it has not been made to date.

In the future the two digital-to-analog converter (DAC) channels could be used to control the plasma current  $I_P$  to hold the rate constant. The PD/20 power supplies would need extensive modifications to accomplish this but the PD/200s require only minor modifications. Since  $V_T$  doesn't drift very much, it would be sufficient to hold the product  $V_TI_T$  constant (i.e. constant sputtering power). In this way one need only feed back to  $I_P$ , rather than both  $I_P$  and  $V_T$ . DAC channels 0 and 1 are reserved for feedback to PD/200 #1 and PD/200 #2 respectively.

### APPENDIX B

## SPUTTERING SYSTEM INSTRUCTIONS

## A. PREPARING FOR A SPUTTERING RUN

J.M. Slaughter

2/87, 8/87, 11/87

Before opening vacuum chamber the following clean parts should be ready for installation:

top confinement covers

bottom confinement covers

magnetic covers

target inserts

orifice plates

chimneys and covers - one open and one closed for each gun

SPAMA plates

substrates

The parts should be cleaned mechanically to remove old metal. In addition, Aluminum gun parts may be cleaned with the following solutions:

- B. 1:1:1 NH<sub>4</sub>OH : H<sub>2</sub>O<sub>2</sub> : H<sub>2</sub>O Ag

(This solution will leave a black residue on the parts.

Solution C may be used, briefly, to remove this residue.)

C. 9:1:3  $HNO_3$ : HF:  $H_2O$  Si, many others

(Use caution with this soln. it will attack the Al parts. May be in contact with the parts for only a few min.)

SPAMA plates, substrate holders, etc. must not be cleaned with acids since they are made of a variety of metals. Solutions A and B above attack Al very slowly but will attack most other metals.

### CHECKLIST:

(Instructions follow checklist)

- 1. Install clean parts and targets in guns do electrical check of the guns.
- 2. Install proper shutter setup and label handle positions. There must not be any flaking metal on chimneys or shutter arms.
- 3. Clean glass viewport shield reinstall.
- 4. Remove any flaking metal from mask plate or install a clean one.
- 5. Set up the SPAMA set height of substrates write down the setup in the lab book.
- 6. Install correct FTM xtals and check for proper FTM operation. Write down the setup in the lab book.
- 7. Install clean substrates in substrate holders. Write down the substrate setup in the lab book.
- 8. Make sure the SPAMA is in the neutral position.
- 9. Check that the hook on the wobble stick is in the desired position and that it is fully retracted.
- 10. Inspect the o-ring before closing vacuum chamber to pump down.
- 11. After closing chamber remove the nuts from the hoist screws.
- 12. Reconnect the FTM electrical connections.
- 13. Make sure that all of the guns are connected to their supplies.
- 14. The FTM's must be programed with the proper parameters.
- 15. Check water filters.

- 16. Test the sputtering guns. The test may be performed anytime as long as the base pressure is below 5E-6 torr. The sooner the test is performed, the less time is lost if something is wrong.
- 17. If you will be reading sample parameters from disk during the run, the sample parameter files must be created.
- 18. If an unusual setup is to be used, a new setup file may be needed (see "Making a Sputtering Run" for the names of the standard files).

## INSTRUCTIONS:

1. Gun parts must be free of all flaking metal. Inspect the area around the filament for flaking metal. If necessary the filament assembly may be removed and cleaned without removing the gun from the chamber. Replace the filament if it shows significant thinning.

## Electrical Check:

Make sure that the circuit breakers are off. Disconnect target and plasma cables from power supplies and turn on water. Check the following resistances at the feedthroughs outside the vacuum chamber:

Ground to target	>200 KOhm
to anode	infinite
to filament	infinite
to housing	>200 KOhm
Housing to filament	infinite
to anode	infinite
to target	>200 KOhm
Target to anode	infinite
to filament	infinite
Filament to anode	infinite
Across filament connectors	<0.5 Ohm

Note that this check is slightly different than the one in the Simard manual.

- 2. Shutter setup: Each gun needs an open chimney and a closed one. Whenever possible the shutter should be arranged so that only the guns operating at any given time have open chimneys. Remember that even the open chimneys need to have covers (with the proper size openings).
- 3. Clean glass window cover: Use acid followed by alcohol. Don't use solution C it attacks glass.
- 4. SPAMA Plates: It is very important that these plates remain flat so handle them with care. Be careful to avoid putting force on the pins, they are easily loostened. Sandpaper, not acid, may be used if necessary to remove metal stuck to the underside. Clean with alcohol before returning it to the vacuum chamber.
- 5. SPAMA setup: When attaching the disk to the shaft you must wiggle the plate while tightening the set screw to make sure that the screw goes into a dimple. If the screw is not in the dimple it may come loose during the run disaster. The SPAMA should be tested to make sure that the plates will mate properly. The substrate height can be determined by measuring the distance from the top of the Meissner trap to the substrate and subtracting that distance from 12".
- 6. FTM crystals: Test the FTM's by reconnecting them and turning on the electronics briefly. Hit the 'stop' button to clear the P-FAIL message. After the P-FAIL message is cleared there should be no further error messages unless something is wrong. Use the test button to determine the \$1 life of the xtal. Remember that for most elements the crystals fail long before 0%, often near 50%.

- 7. Clean substrates: The procedure is to use the ultra-sonic cleaner with alconox solution then distilled water then ethyl alcohol. Put each substrate in a separate test tube containing the solution and put them all inside a beaker of water.
- 8. SPAMA: The neutral position is when all plates are in their up position (with the substrate plate rotated 90° with respect to the FTM plate) and the motor is at the zero position.
- 9. Wobble stick: Make sure the end is correct and that it is fully retracted so that it will not be in the way when the top is lowered.
- 10. O-ring: It should be free of foreign particles and not twisted.
- 12. FTM cooling lines. It may be necessary to wrap the tubes with a kimwipe near the feedthrough to keep condensed water from running down the tubes and shorting the oscillator wires.
- 13. Make sure that all of the guns are connected to their supplies. Be especially careful when the RF supply will be used or was used last.
- 14. The FTM's must be programed with the proper parameters. See table 4.1 in the FTM-3000 manual.
- 15. The filters for the cooling water get dirty in just a few runs. New filters can be purchased in the physics store. You should not need any tools to remove the old filters or put on the new ones tightening by hand is sufficient.
- 16. Put the guns through their paces. Run them for at least 10 minutes each and at voltages and currents higher than you expect to use during the run.
- 17. Sample parameter files are simply ASCII files containing the parameters which specify a sample. They can be created with the

COPY command or with any editor that will save a file in ASCII format. The items in a file can be separated by carriage returns or commas. The format of a parameter file for CMS is different from that for FILM. The formats are the following.

# parameter file for CMS:

```
remarks
            (any discriptive material you like)
                     (a number)
substrate holder
letter of 1st gun
                      (a, b, c or d)
letter of 2nd gun
                      (a, b, c or d)
               (number of angstroms in layer for 1st gun)
thickness 1
                (number of angstroms in layer for 2nd gun)
thickness 2
number of cycles
                     (integer - number of periods in CMS)
               (a, b, c or d to make last layer with)
finish gun
record supply parameters
                             (v or n)
mask number
                (integer number if using masks else nothing)
```

## parameter file for FILM:

```
remarks (any discriptive material you like)
substrate holder (a number)
number of layers (from 1 to 10 inclusive)
letter of 1st gun (a, b, c or d)
thickness 1 (number of angstroms in layer for 1st gun)
letter of 2nd gun (a, b, c or d)
thickness 2 (number of angstroms in layer for 2nd gun)
...
mask number (integer number if using masks else nothing)
```

Example: The following file specifies a CMS sample with material 1 from gun B and material 2 from gun A. It has 62 periods with each period consisting of 40Å of each material. The first and last layers are from gun B, the substrate is #1 and the mask is #5 The target supply parameters will not be saved on disk.

```
file s.2 - params Ag /Co samp on subst 1 1 b,a 40,40
```

62 b

n

5

18. Setup files contain the parameters which define the current SPAMA setup as well as the positions of objects in the chamber. The setup file of your choice is read from disk when the control program is executed. Like a sample parameter file, a setup file is an ASCII file containing items separated by commas or carriage returns. Positions are specified with the positive direction being CCW viewed from above, gun A as zero and the SPAMA in its neutral position. The format is the following.

```
remarks
            (any discriptive material you like)
                    (number of masks being used, 0 through 16)
number of masks
position of mask 1
                       (in degrees)
position of mask 2
                       (in degrees)
position of last mask (in degrees)
number of substrate holders
                             (number of holders, 1 through 16)
position of substrate 1
                            (in degrees)
position of substrate 2
                            (in degrees)
position of last substrate (in degrees)
position of FTM 1
                      (degrees)
position of FTM 2
                      (degrees)
acceleration for sample making
                                 (rev/s - 10 absolute max)
minimum allowed time delay over gun
                                        (seconds)
time to allow for in and out of beam (seconds - depends upon
                                      size of beam and maximum
                                      acceleration)
position of wobble stick
                             (degrees)
position of viewport
                         (degrees)
using separate substrate plate
                                   (y or n)
```

Example: The following setup file is used for the production of perpendicular transport samples. There are 16 mask positions (not all used) and 4 substrates. The other items are typical.

```
setup for separate substrate and mask plate - 4 substrates 16
40.5, 49.5, 63, 72, 108, 117, 130.5, 139.5, 220.5, 229.5
243, 252, 288, 297, 310.5, 319.5
4
85.5, 94.5, 265.5, 274.5
0,180
5
.3
.2
45,135
```

## B. MAKING A SPUTTERING RUN

J.M. Slaughter

2/87, 11/87

### Notes:

- 1. Before the run begins, each of the guns should be run for approximately 10 min. to insure that they are working.
- 2. The programs that will be used during the run should be checked by doing a dry run with the guns off.
- 3. The dead volume pressure is kept between 1 atm. and 15 psig. To keep within this range it must be refilled every:

2 1/2 hr for 1 gun

1 1/4 hr for 2 guns

1 hr for 3 guns

3/4 hr for 4 guns

More often if using flow rates > 35 sccm, use

4. If the cold-trap Ar purifier was used for the last run, pump out and flush the cold trap and dead volume several times. Then the dead volume can be filled by opening the valve on the regulator.

## CHECKLIST

- 1. Stepping motor is turned on (aux 2).
- 2. FTM parameters have been programed.
- 3. Main valve on UHP Ar tank is open, the regulator is set to 15 psig, and the cold trap and dead volume have been flushed if necessary. Be sure to refill the dead volume according to the schedule above.

- 4. The cold-trap Ar purifier has been filled with LN<sub>2</sub> and turned on. See pp. 18-19 of sputtering system log book #4 for detailed instructions.
- 5. The valve between the cold trap and the Hydrox purifier is open.
- 6. The Hydrox purifier has been plugged in for >30 min. with Ar flowing through it.
- 7. GFC has been on for at least 10 min to warm up.
- 8. Cables to gun power supplies are reconnected.
- 9. Circuit breakers for power supplies to be used are on.
- 10. VPC: IG2 and CG2 are set for Ar
- 11. Meissner trap has been filled.
- 12. Water is turned on to all guns and the FTM's

When the checklist is complete you may procede with starting the guns.

## STARTING THE GUNS

# A. Setting the Ar pressure

- 1. Make sure that the gate valve is open all the way.
- Manually turn on the gas for the first gun that you wish to ignite.
   Adjust to desired flow rate (typically ≥ 30 sccm).
- 3. Adjust gate valve until IG2 reads about 3E-3 torr.
- 4. Switch off gas flow. Pressure should drop rapidly. Return the auto/manual switch to auto if you wish to use auto plasma ignition. If you are using a PD/20 then make sure that its gas switch is in the corresponding position.

## B. Igniting the plasma

- 1. Make sure that the gun's chimney is closed.
- 2. Set the plasma current knob at approximately 35%.
- 3. Turn off IG2 if igniting a PD/20.
- 4. a. For PD/200 plasma supplies used in the auto emission mode, the emitter current knob should be set at approximately 82%. This value will limit the maximum emitter current to < 40A. LET THE PD/200 WARM UP FOR A MINUTE OR MORE by turning on the front panel circuit breaker but leaving the yellow power switch off. To start the plasma just press the power switch and the gas switch. If the corresponding GFC channel is on auto then the gas flow will start automatically.
- b. The PD/20 supply's emitter current knob sets the actual emitter current since it does not have the auto emission circuit. Begin with it set at 70%. If the gas switch is on AUTO just turn on the supply and after approx. 20s the gas should switch on and the plasma ignite. If you are controlling the gas manually then turn on the gas when the emitter current is at  $\sim$ 28A. In either case, if the plasma does not light (i.e. if the plasma current is zero) then turn off the supply, wait about 30s and try again. Once the plasma has been ignited the emitter current should be adjusted, so that the plasma voltage is  $\epsilon$  (50, 60V). 30A is a typical value.
- 5. If more than one gun will be used then lower the pressure to about 3E-3 on IG2 and ignite the next gun. Repeat ...
- 6. When all the desired guns have been ignited lower the pressure and restart IG2 if necessary. Use the gate valve to set the desired Ar pressure.

## C. Sputtering

- 1. Turn on the target supply and raise the voltage slowly to a value greater than the desired target voltage. Sputter into the closed chimney at this elevated voltage for a few minutes then reduce the target voltage to the desired value.
- 2. Procede to set the deposition rate using the appropriate computer program.

## MAKING SAMPLES USING THE COMPUTER PROGRAMS

To start the computer put a disk labeled "SPUTTER runtime" in drive A and and a "RUN DATA" disk into drive B. Push the master power switch. Once in DOS enter "MENU" and the menu program will start. Now is a good time to turn on the stepping motor (AUX 2).

When the program prompts for the setup file enter the name of the setup file that describes the setup for the run.

- 4.set => 4 sample setup with changeable masks
- 8.set => 8 pairs of samples using wobble stick
- 16.set => 16 independent samples using wobble stick
- clay.set => setup for clay wheel
- In all cases the motor must be set to the zero position using the 'position' routine before any other moves are made.
- Do not open/close shutters or raise/lower plates unless promptedby the program.
- 3. When raising or lowering plates one should check the plate's progress at intermediate steps and when it is in the final position. Starting the motor while plates are not mated correctly

would most likely result in damage to the SPAMA and possibly severe damage to the Temescal rotary feedthrough.

There are 14 turns from the full up position to the substrate plate down position. Turn about 9 turns and check that the plate is mating with the pins of the disk then do the additional 5 turns. Now check that the arms of the substrate plate are free of the arms of the FTM plate. Do not continue unless they are free! There are 26 additional turns to put the FTM plate down. Do about 21 of them and check that it is mating with the pins of the mask plate then do the additional 5 turns. Now check that the pins in the lift have pulled out of the block that supports the FTM plate. IF THE PINS ARE NOT OUT WHEN THE MOTOR TRIES TO MOVE THE FTM PLATE BAD THINGS WILL HAPPEN!

4. The run description that you enter should include everything needed to identify the samples later. e.g. type of substrates and their positions, target material for each gun, and a description of each mask

#### ENDING A SPUTTERING RUN

- 1. Follow any instructions that the program may give for completing the run.
- 2. Reduce the target voltages to zero and turn off the target supplies.
- Reduce the plasma currents to approximately 5A or less and turn off the plasma supplies.
- 4. Turn off the stepping motor (aux 2)

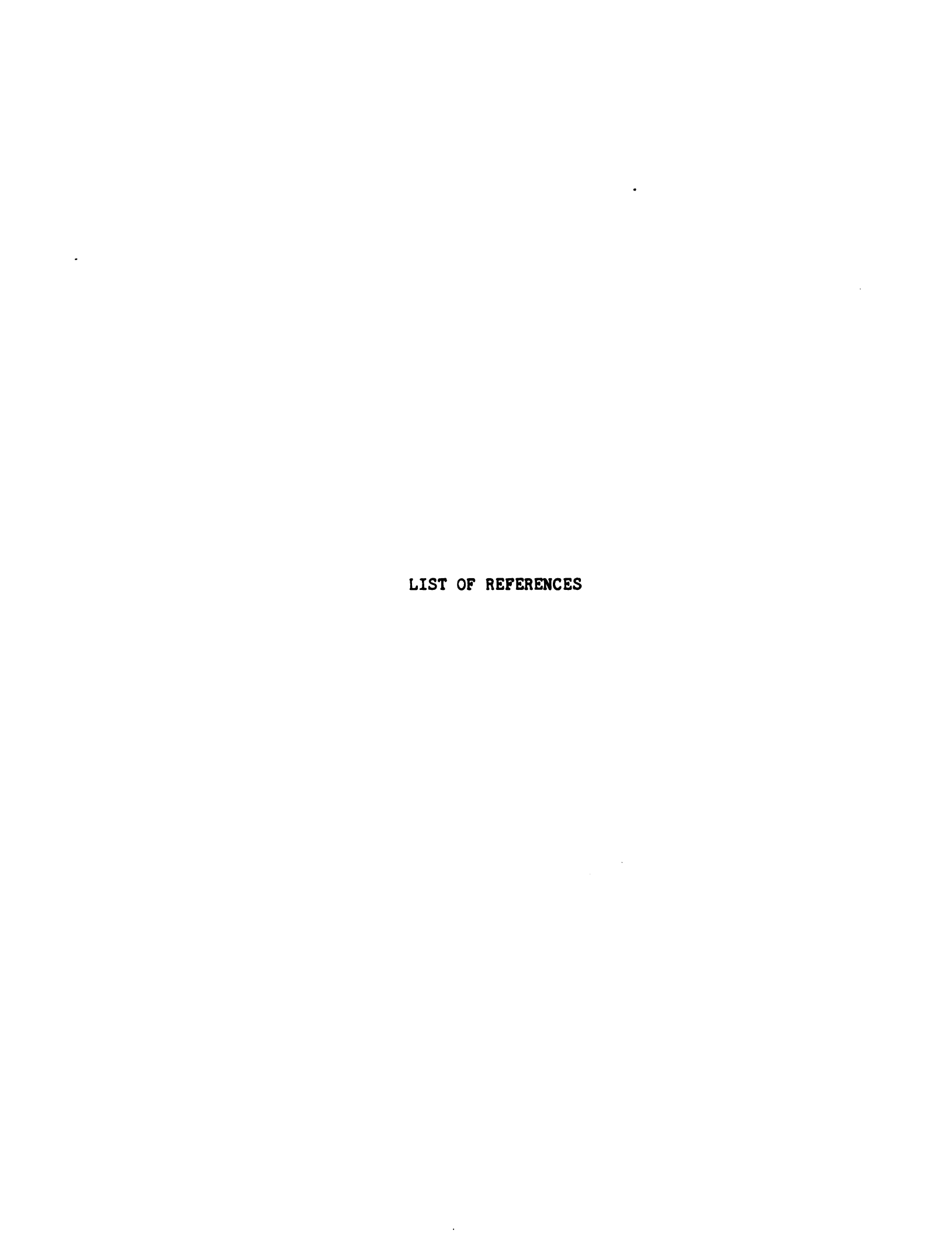
- 5. Turn off the circuit breakers for the supplies.
- 6. Turn off the cooling water.
- 7. Unplug the Hydrox purifier and close the valve between the coldtrap purifier and the Hydrox.
- 8. Refill the dead volume and close the valve on the Ar cylinder.
- 9. Open the gate valve all the way.
- 10. It's a good idea to print run output now. After returning to DOS type COPY B:RUNnnn.\* PRN: where nnn is your run number.
- 11. Remember to fill out the gun log book.

## REMOVING SAMPLES FROM THE VACUUM CHAMBER

Notes: It is best to wait for the liquid nitrogen trap to warm before opening the vac. chamber. If the samples are not needed immediately it is best to wait until gun parts etc. are ready for the next run before opening, this minimizes the amount of time that the vac. chamber is open.

- 1. Make sure the stepping motor is off.
- 2. Disconnect the FTM electrical connections.
- 3. Close the gate valve all the way.
- 4. Turn off IG2. Make sure CG2 is set for Ar.
- 5. Vent the chamber with Ar.
- 6. Make sure that the wobble stick is fully retracted and locked in place.
- 7. Put the nuts back on the hoist screws and turn them with a wrench until the main flange has opened about 1/2".

- 8. Now the hoist may be used to lift the chamber top.
- 9. Immediately put the nylon protective rings on the main flange halves.
- 10. The samples may now be removed from the sample holders.



## LIST OF REFERENCES

- [AP] Apiezon Products Limited, London S.E.1, ENGLAND
- [As76] Neil W. Ashcroft and N. David Mermin, "Solid State Physics," Saunders College, Philadelphia, PA (Holt, Rinehart and Winston; 1976)
- [Ba82] J. Bass in Landolt-Bornstein Group III Vol. 15a, Springer-Verlag, NY (1982) p. 140
- [Be70] L. Berger, Physical Review B 2, 4559 (1970)
- [Ca83] P. F. Carcia and A. Suna, Journal of Applied Physics 54, 2000 (1983)
- [Ca85] P. F. Carcia, A. Suna, D. G. Onn and R. van Antwerp, Superlattices and Microstructures 1, 101 (1985)
- [Ch86] C. Chappert, D. Renard, P. Beauvillian, J. P. Renard and J. Seiden, Journal of Magnetism and Magnetic Materials <u>54-57</u>, 795 (1986)
- [COM] Compumotor Corporation, Petaluma, CA
- [CTI] CTI-Cryogenics, Kelvin Park, Waltham, MA
- [DT] Data Translation, Inc., Marlboro, MA
- [DYC] Amtek-Dycor, 150 Freeport Rd., Pittsburgh, PA
- [Ed80] D. Edmunds, W.P. Pratt, Jr. and J.A. Rowlands, Review of Scientific Instruments 51, 1516 (1980)
- [Fa84] Charles M. Falco, Journal of Applied Physics <u>56</u>, 1218 (1984)
- [Fu38] K. Fuchs, Proceedings of the Cambridge Philosophical Society 34, 100 (1938)
- [Ga73] P.S. Galepov, Physics of Metals and Metallography 34, 134 (1973)
- [GP] Granville-Phillips Co., 5675 East Arapahoe Ave., Boulder, CO
- [Gu86] M. Gurvitch, Physical Review B <u>34</u>,540 (1986)
- [Ha74] G.L. Harding, A.B. Pippard and J.R. Tomlinson, Royal Society of London Proceedings A 340, 1 (1974)

- [Hs80] Thomas Y. Hsiang and John Clarke, Physical Review B 21, 945 (1980)
- [HUB] Huber, Rimsting, Germany
- [Hu72] Colin M. Hurd, "The Hall Effect in Metals and Alloys," Plenum Press, New York (1972)
- [IMI] Imperial Metal Industries, Witton, Birmingham, England
- [Kh83] M. R. Khan, C. S. L. Chun, G. P. Felcher, M. Grimsditch, A. Kueny, C. M. Falco and I. K. Schuller, Physical Review B 27, 7186 (1983)
- [Ki46] Charles Kittel, Physical Review 70, 965 (1946)
- [Ki49] Charles Kittel, Reviews of Modern Physics 21, 541 (1949)
- [Ko75] R. Koepke and G. Bergmann, Zeitschrift für Physik <u>B21</u>, 185 (1975)
- [Ko81] J. Koehler, Physical Review B 23, 1753 (1981)
- [Kr86] R. Krishnan and M. Tessier, Physica Status Solidi (a)97, K39 (1986)
- [Le86] K. Le Dang, P. Veillet, C. Chappert, P. Beauvillian and D. Renard, Journal of Physics F: Metals Physics, 16, L109 (1986)
- [MAT] Matheson Gas Products, P.O. Box 96, Joliet, IL
- [Ma70] A.F. Mayadas and M. Shatzkes, Physical Review B 1, 1382 (1970)
- [Mc85] D. B. McWhan in "Synthetic Modulated Structures," edited by Leroy L. Chung and B. C. Giessen, Academic Press, Inc. (1985)
- [Me80] R. Meservey, P.M. Tedrow and V.R. Kalvey, Solid State Communications 36, 969 (1980)
- [MIC] Microsoft Corporation, Bellevue, WA
- [Mo58] N. F. Mott and H. Jones, "The Theory of the Properties of Metals and Alloys," Dover Publications, Inc., New York, NY (1958)
- [Ne54] L. Neel, Journal of Physics Radium 15, 225 (1954)
- [Pa76] Arun K. Pal, S. Chaudhuri and A.K. Barua, Journal of Physics D: Applied Physics, 9, 2261 (1976)
- [Pi71] A.B. Pippard, F.R.S., J.G. Shepherd and D.A. Tindall, Royal Society of London Proceedings A 324, 17 (1971)

- [Pr85] G.A. Prinz, Physical Review Letters 54, 1051 (1985)
- [RIG] Rigaku Corp., Kandasurugadai, Tokyo, JAPAN
- [Sa87] H. Sato, P.A. Schroeder, J. Slaughter, W.P. Pratt, Jr., and W. Abdul-Razzaq, submitted to Superlattices and Microstructures (1987)
- [Se73] Armin Segmuller and A. E. Blakeslee, Journal of Applied Crystallography 6, 19 (1973)
- [SHE] SHE Corporation, San Diego, CA
- [SIM] L. M. Simard, Inc., 759B Ward Drive, Santa Barbara, CA
- [SLN] Sloan Technology Corp., Santa Barbara, CA
- [So52] E. H. Sondheimer, Advances in Physics 1, 1 (1952)
- [St80] Steven Dale Steenwyk, Ph.D. Thesis, Michigan State University (1980)
- [Su54] W. Sucksmith, F.R.S. and J. E. Thompson, Royal Society of London Proceedings <u>A225</u>, 362 (1954)
- [Sz86] J. Szczyrbowski and K. Schmalzbauer, Journal of Phsics F: Metals Physics 16, 2079 (1986)
- [Ta84] M. Takahashi, S. Ishio and Y. Notohara, Conference on the Physics of Magnetic Materials, Jadwisin Poland (1984), p. 13.
- [TEM] Airco Temescal, Berkeley, CA
- [Tr87] Nandini Trivedi and N. W. Ashcroft, Physical Review B 35, 6084 (1987)
- [UC] Union Carbide, Linde Division, Danbury, CT
- [va87] P.C. van Son, H. van Kempen and P. Wyder, Physical Review Letters 58, 2271 (1987)
- [VG] Vacuum Generators Ltd., Hastings, England
- [Vi83] R.H. Victoria and L.M. Falicov, Physical Review B 28, 5232 (1983)
- [Wa69] B. E. Warren, "X-ray Diffraction," Addison-Wesley Publishing Co., Reading, MA (1969)
- [Wa75] J.R. Waldram, Royal Society of London Proceedings A 345, 231 (1975)

[We82] T. R. Werner, I. Banerjee, Q. S. Yang, C. M. Falco and I. K. Schuller, Physical Review B <u>26</u>, 2224 (1982)